



# **REU PROGRAM IN INTERDISCIPLINARY MATERIALS RESEARCH**

Research Reports by Students Supported by  
the REU Site: Interdisciplinary Materials  
Research for Undergraduates  
(NSF REU Site Program, DMR-1757420)

This REU Program for Interdisciplinary Materials Research is co-organized and co-supported by the REU Site for Interdisciplinary Materials Science (NSF REU Site Program, DMR-1757420) and the Cornell Center for Materials Research (NSF MRSEC program, DMR-1719875). This document contains the reports by all students that were funded by the REU Site. The photo shows the cohort of the whole REU program.



# TABLE OF CONTENTS

## Student

- 02 David Chapparo
- 07 Ashley Del Valle Morales
- 12 Kaylee Dunnigan
- 19 Kayleigh Jones
- 23 Rachel Lawless
- 33 Myung Joo Lee
- 37 Gabriel Martinez-Zayas
- 42 Maya Martinez
- 48 Jessica Rappaport
- 56 Maximilian Rozenblum

## Faculty Advisor

- Prof. Jeffrey Moses
- Prof. Andrej Singer
- Prof. Tobias Hanrath
- Prof. Itai Cohen
- Prof. Héctor Abruña
- Prof. Richard Robinson
- Prof. Julie Goddard
- Prof. Katja Nowack
- Prof. Matthew Reid
- Prof. Jonathan Butcher

# Automatic Delay Stage for Optical Parametric Amplification

David Chaparro

Department of Applied Physics, Cornell University, Ithaca, New York 14853, USA

## ABSTRACT

Optical parametric amplification is a non-linear process that enables the use of multiple wavelengths at high power without the need of an additional laser source. It is critical for the completion of various experiments such as four wave mixing, multi-photon microscopy, and high powered laser amplification. Additionally, it is useful in studying light matter interactions by creating far infrared pulses that can change the crystal structure of a material. In optical parametric amplification, a high intensity pump beam amplifies a signal beam within a birefringent material with a gain of approximately 10dB-60dB. While this optical setup is useful, numerous conditions must be met in order to achieve optimal gain. For a pulsed laser system, both the signal and the pump beam must be optimally overlapped and synchronized in time. Previously, a manual delay stage was assembled to adjust the path length and time when the pump pulse reaches the non-linear crystal. While useful, the path length of the pump beam changes due to thermal fluctuations. To account for this, I implemented an automated delay stage that precisely maintains a desired amplified signal spectrum by adjusting the path length. This was completed using an Arduino and a Proportional-Integral-Differential feedback loop with a linear photodiode array and stepper motor. The end product has a  $1.25\text{--}\mu\text{m}$  resolution in path length control and can correct for signal disruptions in less than 10 seconds.

## 1 Introduction

### Non-Linear Optical Parametric Amplification

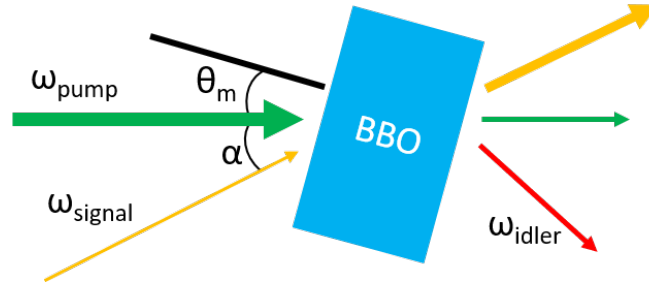


**Figure 1.** This diagram depicts the physical process behind non-collinear optical parametric amplification. A high intensity pump beam encounters a birefringent crystal (Beta Barium Borate) at an angle  $\theta_m$ . Typical angles for  $\theta_m$  range from  $20^\circ$  to  $30^\circ$ . The signal beam encounters the same birefringent material at angle  $\alpha$  relative to the pump beam.

Optical parametric amplification (OPA) is a nonlinear process whereby three waves interact in a birefringent material; a high intensity pump pulse amplifies a low intensity signal pulse, thereby generating a low intensity signal pulse. This nonlinear optical effect is useful in a variety of experiments because amplifies and generates coherent light at wavelengths that most sources can not achieve. This makes it an excellent optical source applications requiring broad bandwidths and short pulse durations.<sup>1</sup> The OPA can amplify signals in the far infrared range and can be used to study optical effects in crystals. By exciting a crystal using far infrared light, it is possible to excite the crystal and transform its crystalline structure. This would change its optical properties and could be determined by changes in its polarization susceptibilities. In the process, an additional idler wave is created due to the conservation of energy. In order to efficiently achieve this effect, energy and momentum must be conserved.

$$\vec{k}_p = \vec{k}_s + \vec{k}_i + \vec{\Delta k}$$



$$\hbar\omega_p = \hbar\omega_s + \hbar\omega_i \quad (2)$$

where  $\omega_p$ ,  $\omega_s$ ,  $\omega_i$  represent the frequencies of the pump, signal, and idler beam, and  $\vec{k}_p$ ,  $\vec{k}_s$ , and  $\vec{k}_i$  represent the wave vectors of the pump, signal, and idler beam respectively and  $\Delta k$  represents the phase mismatch of the wave vectors. In a normal crystal with an isotropic index of refraction, these conditions cannot be met due to the fact that the index of refraction varies in a material as a function of wavelength.<sup>2</sup> To overcome this obstacle, a technique called Non-collinear Optical Parametric Amplification (NOPA) is employed. (Figure 1).

To satisfy the conservation of momentum a birefringent crystal is used. Typically Beta Barium Borate would be rotated slightly such that the phase matching angle  $\theta_m$  of the pump beam is no longer parallel to the crystallographic axis, and the signal beam encounters the pump beam at an angle  $\alpha$  (Figure 3).<sup>3</sup> An additional constraint is added due to the fact that  $\Delta k = 0$  for amplification to occur and for conservation of momentum to be upheld (Figure 2). This condition is called the phase-matching condition, and depends on the incident angle of the signal beam relative to the pump beam.

If all phase matching conditions are met, then the end result is an energy spectrum that amplifies light at the 600nm regime. However one final condition is required in order to achieve optimal gain. Due to the fact that our laser source is pulsed, in order for amplification to occur, the two light pulses must coincide with each other in the BBO crystal both in space and in time. For a constant source laser, the time domain is not an issue, but for our pulsed laser source, the two pulses must sync in time to provide optimal amplification. In order to adjust when light pulses strike the BBO crystal, we installed a delay stage that can change the path length of the pump beam to match that of the signal beam. For my project, I was responsible for automating this delay stage, to ensure that the pump and signal pulses encountered the BBO crystal at the same time. This would be done utilizing feedback loops and sensor arrays, and also lead to the precise management of the NOPA spectrum.

## Conservation of Momentum

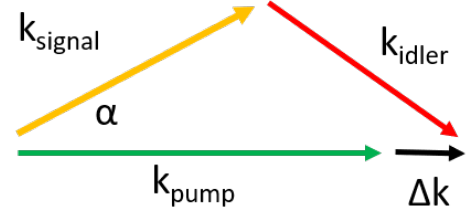


**Figure 2.** This diagram depicts the phase matching condition for non-collinear optical parametric amplification. The magnitude of  $\Delta k$  can be controlled as a function of the signal, pump, and idler wavelength, incident angle  $\theta_m$ , and signal angle  $\alpha$ . Optimal phase matching occurs when  $\Delta k = 0$ .

## 2 Design and Construction

The automated delay stage, was implemented using a linear photodiode array, Arduino, and stepper motor. The sensor was constructed of 3 linear photo-diode arrays, resulting in a sensor with 384 elements for the spectrum. This gives plenty of resolution and allows us to characterize the noise with great accuracy. A back reflection from the OPA amplified signal is sent to the optical setup for analysis. The optical setup consists of a periscope, mirror and diffraction grating (Figure 6). The Thor labs GR13-0609 Diffraction grating with 600g/mm spectrally disperses the beam onto the photo-diode array. Then, the TSL1401CL linear photo-diode array (LPDA) were arranged to capture the full spectrum with enough detail to resolve characteristic spectral features. An Arduino interfaces with the LPDA, captures the spectrum and processes it within the feedback loop. In order to adjust the delay of the signal beam, a stepper motor attached to a micrometer is used due to its low cost and high resolution. The Stepper Motor rotates at 400 steps/rev. When it is attached to our micrometer which has 500 $\mu$ m/rev, our system has a 1.25 $\mu$ m precision. Due to our chosen stepper motor controller, the precision can theoretically achieve

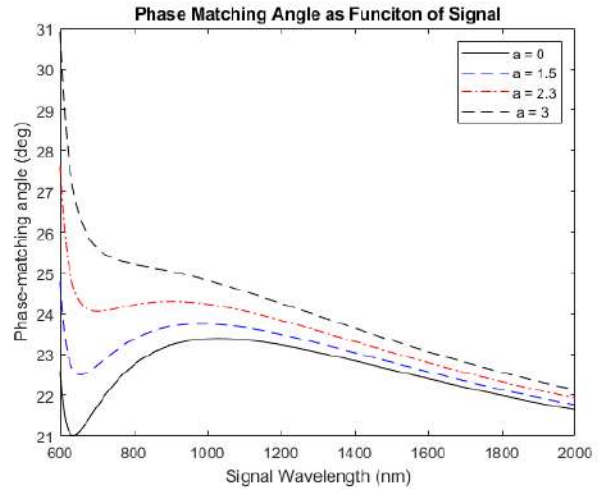


**Figure 3.** This graph shows the optimal angle  $\theta_m$  for various values of  $\alpha$ . Each plot represents the fulfillment of the phase matching condition. The plot varies as a function of signal wavelength and resides around 24°

78nm. Since the speed of light is approximately  $3mm/ps$ , in order to achieve high precision in our corrections, we require  $\mu m$  accuracy.

The sensor was constructed of 3 linear photo-diode arrays, resulting in a sensor with 384 elements for the spectrum. This gives plenty of resolution and allows us to characterize the noise in great accuracy. The optical setup consisted of a periscope, mirror and diffraction grating (Figure 6).

Additionally, in order to maintain the desired spectrum, we must pick a parameter of calculated from the input spectrum that best characterizes the spectrum and can act as an error function for the feedback loop. Two methods were tested during the development of the feedback loop: integral and center of intensity. The integral method takes the integral of the spectrum as a function of diode position and returns the total intensity under the spectrum. However, this indicator is not monotonic as a function of delay position, as the integral follows a Gaussian behavior (Figure 4). While it is possible to use this as the tracking function, it is less precise and requires more complexity due to its non-monotonic nature. Meanwhile, the center of intensity indicator is nearly monotonic as a function of delay position (Figure 5). Because of this, we can achieve a high precision in returning to the set point, and can use a simpler correction algorithm which introduces less noise into the system. Using a Proportional-Integral-Differential feedback loop, we can calculate the deviation from the set point spectrum and correct to return to the original spectrum.

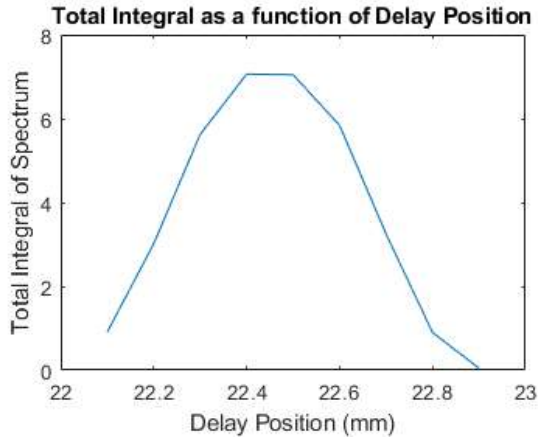


**Figure 4.** This is a graph of the total integral of the spectrum as a function of delay position. It resembles a non-monotonic Gaussian curve. Since this is the area of where the spectrum remains non-zero, the average center delay positions we are working with, this is not the ideal metric to characterize the spectrum. Primarily this is due to the added complexity of corrections algorithm that would make it unfeasible.

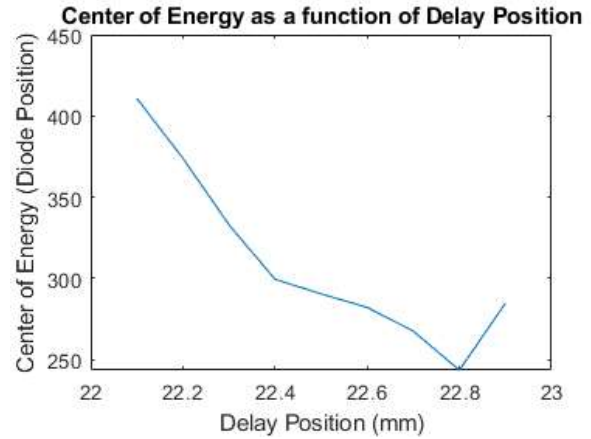


**Figure 5.** This figure depicts the measured center of intensity as a function of delay position. In the region of intensity varies nearly as a monotonic function. This is especially useful because the monotonic function gives us additional information about our position and allows us to create a quicker correction function.

Additional software feedback mechanisms were set in place to suppress noise in the system. A function that calculates the total integral of the spectrum is used to detect if light is shining on the photo-diode array. If no light is shining onto the sensor, no feedback is produced, preventing the spectrum from moving outside the monotonic correction area. An additional noise reduction method was implemented to reduce the mechanical noise of the motor by limiting when the motor can apply corrections. If the feedback for the system stays below the accuracy threshold for more than 30 seconds, the feedback loop is disabled so noise cannot trigger the motor to move unnecessarily. After 30 seconds, the feedback loop is enabled and applies any corrections to the spectrum.

### 3 System Characterization

When the NOPA was created, the first characterization was that of the superfluorescence. Superfluorescence occurs when there is no signal beam to induce amplification and quantum noise gets amplified and produces a gain profile. This gain profile represents the amplification as a function of signal frequency and can be observed on a spectrometer. Once the signal beam is applied to

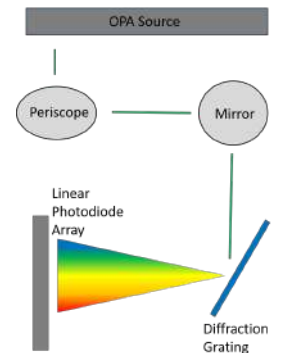


**Figure 6.** This is a block diagram of the optical components needed to track the signal spectrum. It consists of a periscope to change the polarization of light, and

the BBO crystal, the optimal delay spectrum is found by varying the delay position. The optimal gain spectrum is shown below.

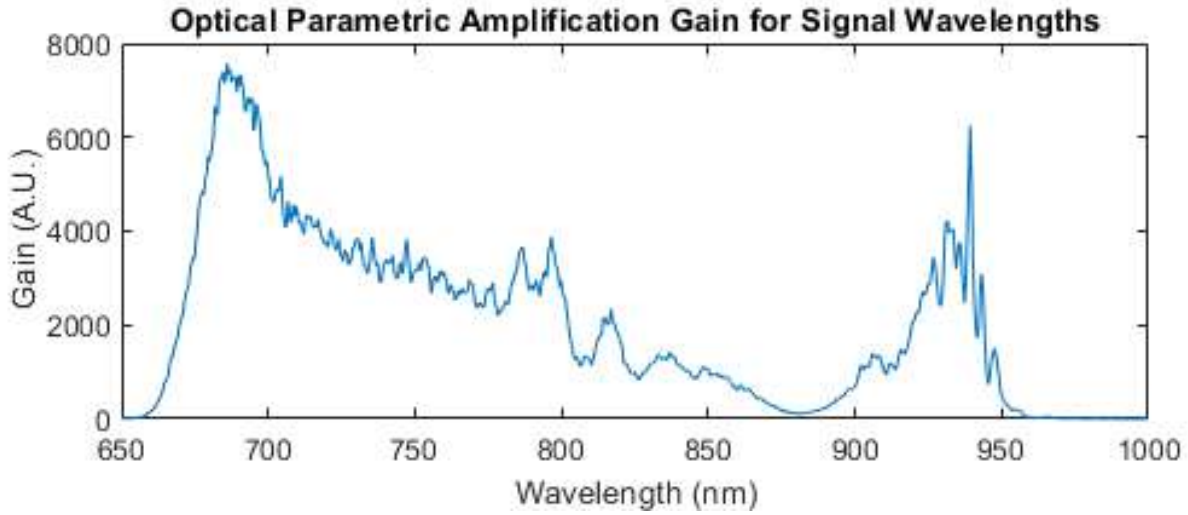


**Figure 7.** This figure shows the spectrum of the amplified signal beam. This is the desired spectrum for the amplifier and is the set point for our feedback system.

After the dark noise was characterized, a test began to characterize the drift of the OPA spectrum as a function of time. In this test, the motor was not turned on, and the delay stage was held static in its position.

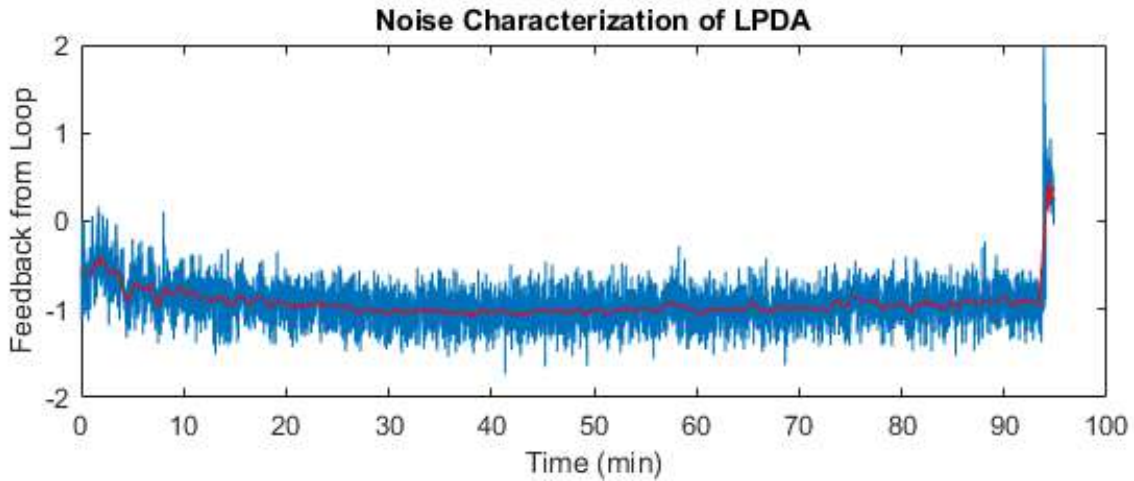


**Figure 8.** This graph as a function of time characterizes deviation from set point position. The data was taken with a static delay position until the end of the data set where the delay position was returned to its set point by hand. The blue data is the actual measurement, while the red line is a moving average of the data. It is possible to determine that the spectrum of the OPA did drift away from its set point before settling at a value around -1.1. At the end of the time series, the OPA signal was corrected, and as predicted, the feedback returned to a value close to zero, meaning that the Average Position Indicator was in fact a reliable characterization method. The Standard deviation of the noise from the average was .2038

These measurements show that the average position of spectrum indeed is a good indicator of the set point of our system. Additionally, excess noise created by the automated feedback loop can be minimized using a software limit to prevent the motor from correcting too frequently. Additionally, at the end of the recording, the spectrum was set back to its original position. The moving average, depicted by the red line in Figure 8, shows the center of intensity was close to its original set point. Additionally, we were able to reach the set point with a precision of  $1.25 \mu\text{m}$ .

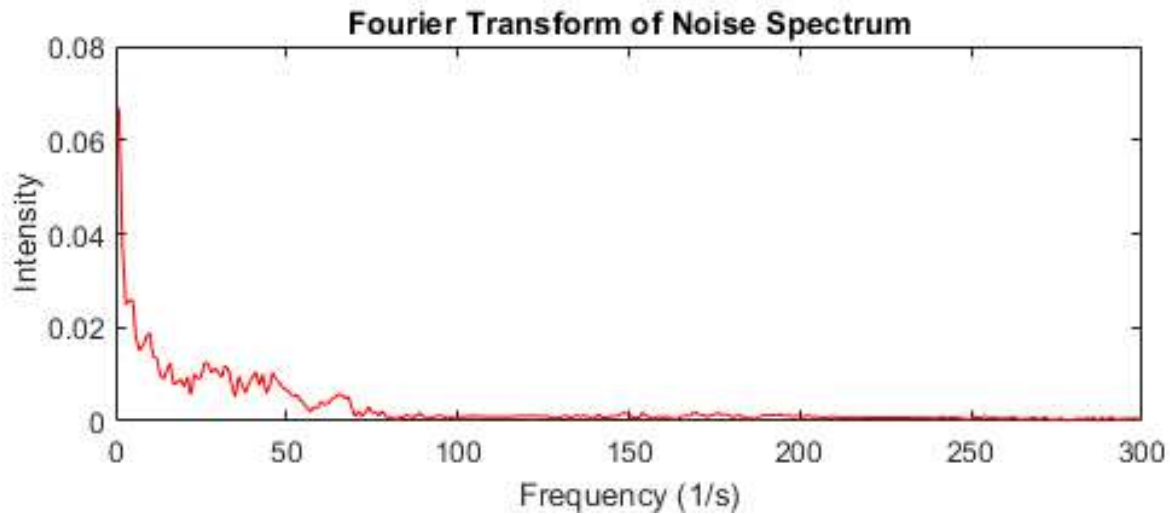


**Figure 9.** This figure is a Fourier transform from the Noise Characterization of LPDA. It shows that a large amount of the noise is in the low frequency domain. Most of the noise stays below 100hz. Most of the higher frequency noise can be attributed to changes in voltage measurements coming from the LPDA while the lower frequency noise stems from the spectrum drift over time.

Further characterization was completed during the troubleshooting and tuning process, however, no complete data set was taken to depict overall system performance. Unfortunately, before a time series could be acquired, the laser source suffered a critical error that disabled it for the remaining weeks. However, during an earlier test of the system, the automated delay stage successfully recovered the center of intensity after perturbations were applied to it. The feedback system corrected large deviations from the set-point within 15 iterations of the code, and corrected within 30s of a perturbation.

## 4 Conclusions

Optical Parametric amplification is a non-linear process that can generate light at wavelengths distinct from the source. This device enables experiments with more than one source to be completed without the purchase of another source. Through the use of the automated delay stage, it is possible to maintain optimal amplification with minimal intervention by the user. This allows for more sensitive measurements and more accurate experiments. With the use of the automated delay stage, it is possible to create a more robust optical parametric amplifier that is resistant to changes in beam pointing and thermal noise. This allows for the ideal amplification to occur in the device and enables us to perform more precise measurements and with greater ease. This allows experiments to be completed at a greater rate and allows us to reach for more interesting science as a result.

## References

1. Heberle, Dylan A., Flemens, Noah R., Ding, Xiaoyue, Chang, Wei-Zung & Moses, Jeffrey. Towards a 10-fs hyperspectral spectroscopy source with arbitrary pulse shaping based on adiabatic frequency conversion. *EPJ Web Conf.* **205**, 01027 (2019). URL <https://doi.org/10.1051/epjconf/201920501027>. DOI 10.1051/epjconf/201920501027.
2. Manzoni, C. & Cerullo, G. Design criteria for ultrafast optical parametric amplifiers. *J. Opt.* **18**, 103501 (2016). URL <https://doi.org/10.1088/2040-8978/18/10/103501>. DOI 10.1088/2040-8978/18/10/103501.
3. Cerullo, G. & De Silvestri, S. Ultrafast optical parametric amplifiers. *Rev. Sci. Instruments* **74**, 1–18 (2003). URL <https://doi.org/10.1063/1.1523642>. DOI 10.1063/1.1523642. <https://doi.org/10.1063/1.1523642>.

# Structure dynamics in sodium-ion batteries during charging

Ashley A. Del Valle, Oleg Gorobtsov, Andrej Singer  
Cornell Center for Materials Research

**Abstract:** Large-scale energy storage is crucial for the development of renewable energy systems. Lithium-ion batteries are very well-known due to their efficiency and low cost. Nevertheless, when considered on a large-scale, they are not feasible. Sodium-ion batteries are gaining more attention every day. This element is more abundant than Lithium. Nonetheless, it also has a lower ionization potential than Lithium, leading to lower operating voltages and thus lower energy densities. Additionally, structural degradation is much more severe in sodium ion batteries. This research focuses on understanding the intrinsic behavior of Sodium-ion batteries to better understand what is happening on a particle level using operando X-ray imaging. Particularly, we focus on bragg coherent diffraction imaging and tested the reliability of the phase retrieval algorithm in use by comparing different scans taken from the same particle. The algorithm showed positive results when reconstructing the shape of the particle, nonetheless, there are still inconsistencies when analyzing the dislocation density and formation.

## Introduction

Rechargeable lithium ion batteries, (LIBs), have become successful and sophisticated energy storage devices [1]. LIBs were originally developed as a high-energy power source for portable electronic devices. Currently, LIBs are taking the lead in plug-in electric vehicles and renewable energy, producing batteries that can store up to megawatt-hour (MWh) viewed as large-scale energy storage.

Although LIBs potential has been demonstrated over the years, scientists are questioning the feasibility of lithium, which is certainly the inherent element in LIBs. Lithium is widely distributed in the Earth's crust but is not regarded as an abundant element [1]. In contrast to lithium, sodium resources are unlimited everywhere, been one of the most abundant elements in the Earth's crust and the ocean, see **figure 1**.

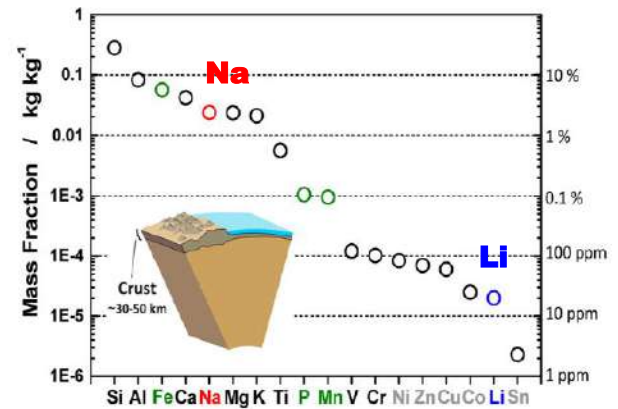


Figure 1 Elemental abundance in the Earth's crust [1].

Sodium-ion batteries are a promising alternative, they typically have poor electrochemical activity when compared to LIBs, see **figure 2**. This is due to two intrinsic shortcomings associated with Na. First, it has a lower ionization potential than Li, leading to lower operating voltages and thus lower energy densities in comparison to LIBs. Second,  $\text{Na}^+$  ions are heavier and larger than  $\text{Li}^+$  ions, leading to slow diffusion within a solid electrode during cycling of SIBs and offer larger volume expansion of the electrode when compared with LIBs [2].



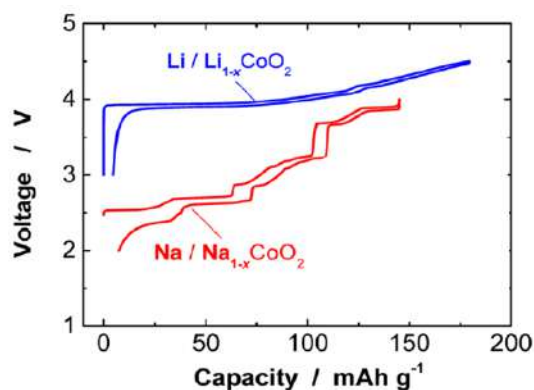


Figure 2 Comparison of charge/discharge curves of Li/LiCoO<sub>2</sub> and Na/NaCoO<sub>2</sub> cells [1].

Sodium Batteries, called Na-ion batteries (NIBs), consist of sodium insertion materials with aprotic solvent as electrolyte, positive and negative electrodes, which are electronically separated by electrolyte [1]. In general, electrolyte salts dissolved in aprotic polar solvents as a pure ionic conductor. Essentially, the structures, components, systems, and charge storage mechanisms of NIBs are the same of LIBs, except that lithium ions are replaced with sodium ions, see **figure 3**.

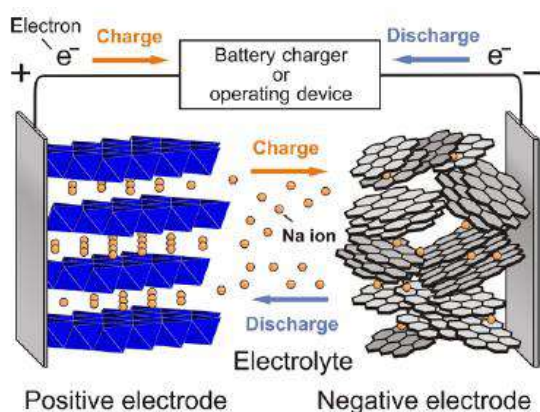


Figure 4 Schematic illustration of Na-ion batteries [1].

This research project focused on understanding the intrinsic behavior of Sodium-ion cathodes to

better understand what is happening on a particle level using operando X-ray imaging. Particularly, on testing the reliability of the algorithm in use by comparing different scans taken from the same particle. The algorithm showed positive results when reconstructing the shape of the particle, nonetheless, there are still inconsistencies when analyzing the dislocation density and formation.

## Procedures

### Operando 3D imaging of the dislocation

Coherent x-ray diffractive imaging is a novel imaging technique that utilizes phase retrieval and nonlinear optimization methods to image matter at nanometer scales [3]. By using the in-situ Bragg coherent diffractive imaging (BCDI) technique, we map the 3D displacement field inside of a cathode nanoparticle during sodium extraction (battery charge) [4]. For this experiment an operando x-ray imaging was used, diffracted x-rays created the diffraction pattern of the

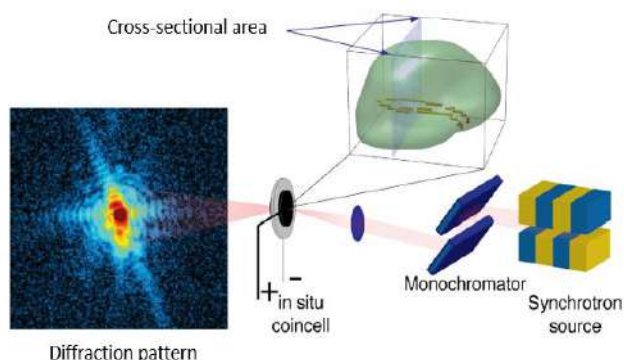


Figure 3 Schematic of experimental arrangement [4].

Na-ion particle, making it possible to study, see **figure 4**. This approach has already proven to be successful when studying LIBs in [4], is expected that it also works for NIBs. Yet, the diffraction patterned obtain from the

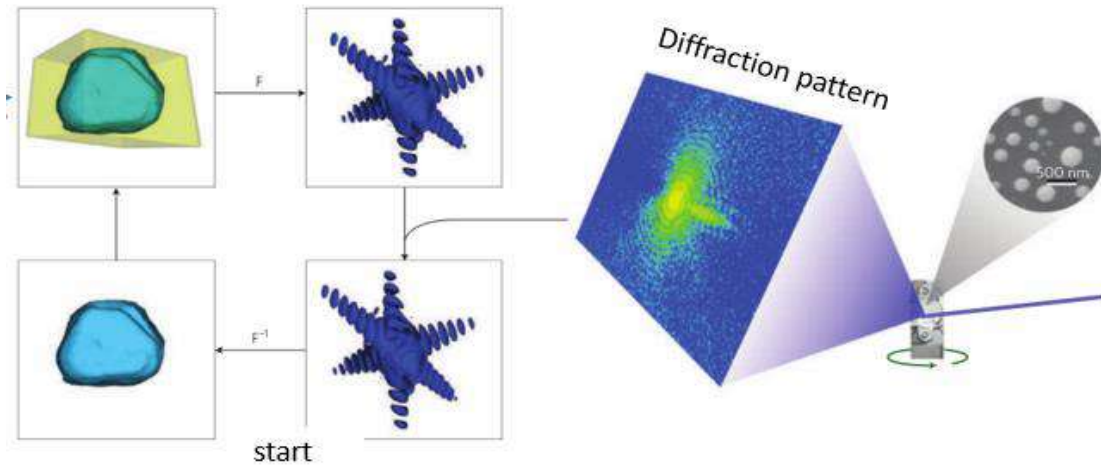


Figure 5 Reconstruction process using Fourier transform iterations [5].

NIBs are not comparable in quality with the patterns obtained from LIBs. Making the data harder to analyze.

After obtaining the diffraction patterns, various reconstruction procedures were tested, including combinations of error-reduction (ER) alternating with hybrid input-output (HIO) [8][9]. The goal is to compare the three scans and determine if they appear to be similar, then the algorithm is reliable and is reconstructing correctly.

To obtain a good reconstruction, it is crucial to have the amplitude and the phase of the diffraction patterns. However, the optical phase cannot be measured by the detector. A conventional phase retrieval iterative algorithm that uses Fourier transforms iterations was used to approximate the phase; since the diffraction intensity is proportional to the squared magnitude of the Fourier transform of the image. It is important to highlight the significance of knowing the Fourier phase. It is well known that knowledge of the Fourier phase is crucial in recovering an object from its Fourier transform [6]. Many times, the Fourier phase contains more information than the Fourier magnitude, as can be seen in the synthetic.

## Results and Conclusion

Three random scans were selected to apply the reconstruction, eight were done in total, see **figure 5**. For each reconstruction a parameter was changed, waiting to see how each parameter affected the data: smoothing and threshold. The algorithm produced the best reconstructions having a higher threshold, a mathematical approach that sets all equations outside the boundary to zero. This was noticeable when analyzing the amplitude of the scans, see **Figure 6**. Using the amplitudes given by the detector, and the phases given by the algorithm, a 3D image was reconstructed showing the estimated shape, dislocation density and formation of the particle, see **Figure 6**. The particle is approximately 200 x 200 x 100 nm. When comparing the three random scan's 3D images, we noticed a similarity in the overall shape of the particle, the shape stays constant also during the analysis of the last scans. Having this similarity in shapes along the scans suggest that the algorithm is indeed reconstructing correctly the size of the

particles. Nonetheless, the dislocation density and formation did not present enough persistence along all the scans to achieve a preliminary conclusion of the reliability of the program. Furthermore, we can conclude that the algorithm can identify the formation of dislocation, this can be viewed when observing the first and last scan. The first scan possesses only a few dislocations, while the last scan (after the battery has been charged) possesses many more dislocations.

To be able to conclude the algorithm is reliable and accurate the team will compare a bigger number of scans, changing more parameters that affect the reconstruction process.

### Acknowledgements

I would like to thank Professor Andrej Singer for offering me the opportunity to work in his lab and Oleg Gorobtsov for his guidance through this project. The data used for algorithm refinement was collected in the collaboration with the group of Shirley Meng at UCSD. Furthermore, my sincere gratitude to the CCMR REU program for making this experience possible.

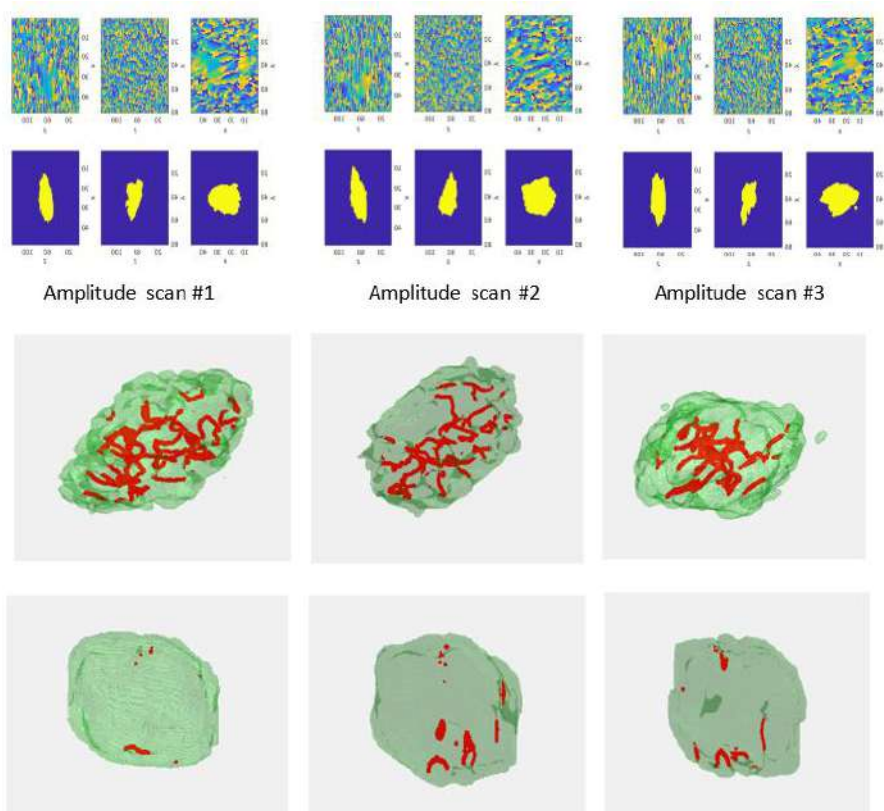


Figure 6 Amplitude and 3D image of best reconstruction achieved with using high-threshold and no smoothing.

### References

- [1] Yabuuchi, N., Kubota, K., Dahbi, M., & Komaba, S. (2014). Research Development on Sodium-Ion Batteries. *Chemical Reviews*, 114(23), 11636–11682. doi: 10.1021/cr500192f
- [2] Sawicki, M., & Shaw, L. L. (2015). Advances and challenges of sodium ion batteries as post lithium ion batteries. *RSC Advances*, 5(65), 53129–53154. doi: 10.1039/c5ra08321d
- [3] Tripathi, Ashish, Leyffer, Sven, Munson, Todd, & M., S. (2015, June 1). Visualizing and improving the robustness of phase retrieval algorithms. Retrieved from <https://www.osti.gov/biblio/1221604>
- [4] Singer, A., Zhang, M., Hy, S., Cela, D., Fang, C., Wynn, T. A., ... Shpyrko, O. G. (2018). Nucleation of dislocations and their dynamics in layered oxide cathode materials during battery charging. *Nature Energy*, 3(8), 641–647. doi: 10.1038/s41560-018-0184-2

- [5] Robinson, I., & Harder, R. (2009, April 1). Coherent X-ray diffraction imaging of strain at the nanoscale. Retrieved from <https://www.nature.com/articles/nmat2400>
- [6] Shechtman, Y. (2014). Phase Retrieval with Application to Optical Imaging. Retrieved from <https://arxiv.org/pdf/1402.7350.pdf>
- [7] McNulty, I. (2014, June 18). PPTX.
- [8] Elser, V. Phase retrieval by iterated projections. *J. Opt. Soc. Am. A* 20, 40–55 (2003).
- [9] Luke, D. R. Relaxed averaged alternating reflections for diffraction imaging. *Inverse Probl.* 21, 37–50 (2005).



# Exploring Single Crystal Quantum Dot Solids Though Dip Pen Lithography Printing Techniques

Kaylee A. Dunnigan<sup>1,2</sup>, Daniel M. Balazs<sup>2,3</sup>, Tobias Hanrath<sup>2,3</sup>

<sup>1</sup>*Department of Chemical and Biomolecular Engineering, New York University Tandon School of Engineering, Brooklyn, NY 11205*

<sup>2</sup>*Cornell Center for Materials Research, Cornell University, Ithaca, NY 14853*

<sup>3</sup>*Cornell University, Robert Fredrick Smith School of Chemical & Biomolecular Engineering, Ithaca, NY 14853*

---

## Abstract

In this study the use of Dip Pen Lithography (DPL) is being explored for the printing applications of quantum dot solids (QDS). The goal of using DPL is to have better control of the crystallization and resulting polymorphs of the QDS nucleation. DPL offers precise control over the location of QDS ink placement with nanosized volumes. This study illustrates initial characterization of DPL in terms of solvents used in inks, size characterization for the ink and liquid surface, as well as other parameters such as ink drying dynamics.

---

## Introduction

Significant advancements have been made in the field of Quantum Dot Solids (QDS) with more control over synthesis, size, structure, and properties over the past decade. Their unique and novel properties have shown potential in the miniaturization of electronics, as superconductors, and interesting optoelectronic properties. There are potential applications in solar cells [1-3], transistors [4,5], and electronics [6,7]. Some properties of QDS will only appear in well ordered arrangements with there are layers of large nucleation crystals in the same direction.

How the arrangements are ordered are impacted by their self assembly. Self assembly is when the QDS organize themselves into more ordered patterns and structures. These arrangements are highly impacted by how the films are developed, so having control over the development of the films, and not just the synthesis of the QDS is important to their final properties. Dip Pen Lithography (DPL) is one method that allows for controlled nanosized placement of QDS inks.

Previous efforts have been made to use ink jet printing with some difficulties in reproducibility and in working with the

equipment. Dip pen nanolithography is when a sharp tip is used to create micro sized patterns directly onto a surface or substrate [6]. For QDS this entails transferring a droplet of ink onto a surface of ethylene glycol, so that the particles can self-orient on a high boiling point and high surface tension solvent. DPL has been seen using novel designed and machined ink tips that have a range of designs and methods of holding and transferring ink [7-9]. Some methods also use an array of pens or needles in order to complete an array of transfers at once [m]. Pen designs range from a sharp tip or needle, to a quill design, to designs that hold excess ink so that the pen does not need to re-ink itself during the process [6-11].

DPL has also been shown as a direct write method where patterns can be drawn onto a surface. QDS inks may be more suited to DPL than inkjet printing or microcontact printing for the reasons of scale and controlled placement [12,13]. For other non QDS inks ink jet printing or microcontact printing has been shown to be a better method due to the faster speed at which these methods work. DPL patterning speed can be considered slow in comparison. DPL is a low cost way to print on the micro and nanoscale. After proof of concept has been shown DPL can be scaled up using a variety of tools. An

inexpensive and reasonable form of DPL is using sewing needles and a z-stage to test ink transfer.

Atomic Force Microscopy (AFM) and a Nano eNabler™ Molecular Printing (NEMP) System are two potential tools that can be used for DPL scale up. AFM has been shown success in using DPL, those many of these studies are transferring ink onto a solid surface and not a liquid surface. Also many of these studies are using polymer based inks as opposed to the organic solvent based inks in this study, this could lead to potential difficulties using the QDS ink with this system. The NEMP shows equal potential in use for scale up, it has been used in other printing studies.

In this study developing QDS inks for DPL and characterizing DPL are focused on. This study will advance process knowledge of making controlled QDS with exact placement of QDS with an order of magnitude smaller volume transfers than done previously. This should aid in the advancement of developing complex layered superlattices and multilayered QDS assemblies.

#### Experimental

#### General Synthesis Pathway for QDS

Synthesis was done following a modified recipe for PbSe quantum dots [14]. PbSe QDS were synthesized in a Nitrogen filled inert environment. PbO (4.00 mmol), oleic acid (10.00 mmol), and 1-octadecene (48.64 mmol) were mixed and heated until 160 °C and the heated for 20 °C more. A selenium-trioctylphosphine solution (8.00 mmol of selenium) injected, then the solution was cooled for about 30°C. Then the solution was cooled quickly in order to stop the continuous nucleation of the PbSe nanocrystals. The size of these crystals were then measured using UV-vis [15].

#### b. Ink Formulation

QDS were dried out of solution and resolved in high boiling point nonaqueous solvents to form the desired inks. Three main solvents were used decane, dodecane, and tetradecane. All inks were formulated in an inert environment.

#### c. Preparing Silicone Surface

The wetting contrast on Si wafers used to hold ethylene glycol in this study were prepared using a previously studied method [16].

## Results and Discussion

### Capillary Forces

The dip pen lithography assembly is performed by covering the tip of the needle in ink and then dipping it into the liquid surface, in this case ethylene glycol, in order to transfer a small volume of the aqueous colloidal suspension. Once the ink is transferred the needle is removed and the ink is left to dry.

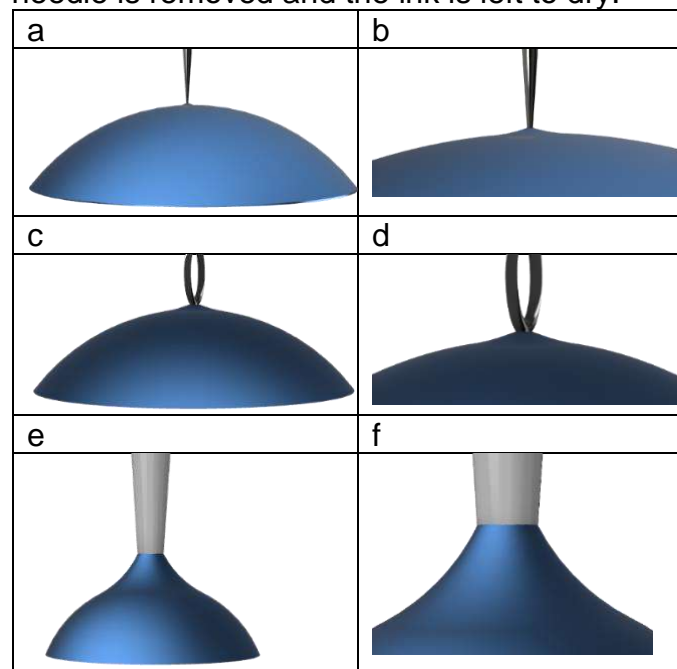


Figure 1 CAD models illustrating the capillary forces caused on the liquid surface as a result of contact with the needle during ink transfer. Figure 1a-1c show the full diagrams and d-f show a closer view of the capillary forces. From left to right the figures illustrate needle in contact with a large liquid surface, the eye of a needle, a needle tip coming in contact with a much smaller surface.

The movement of the needle into and out of the ethylene glycol contributes to the movement of the ink outward on the liquid surface. As the needle moves out of the EG a meniscus is formed around the needle, the liquid surface forms this meniscus and eventually falls back onto the droplet. The assembly of an ordered quantum dot solid film

layer occurs by the ink first spreading across the entire area of the ethylene glycol drop and then drying from the outside of the drop inwards towards the center. Though the force caused by the meniscus does not affect drying shape or consistency since the drying time is significantly longer than the time of ink deposition. The formation of the meniscus increases the time that the needle is in contact with the liquid surface. The smaller the liquid surface is the larger the impact the capillary forces have, at a surface around 1mm<sup>2</sup> the entire droplet forms a meniscus with the needle, so the entire surface of the liquid interface is impacted by the ink transfer. The mechanism of needle transfer of particles is not yet fully understood but will be discussed further later in this paper.

### Transfer Volume in DPL

#### Determining Volume Transferred in Dip Pen Lithography

In order to optimize the use of the DPL printing technique various parameters were analyzed. The volume of QDS ink transferred by a small sharp tip was first determined in a series of experiments. By determining the amount of volume transferred by a needle the concentrations of the ink synthesized and expected layer thickness made by the ink can be more precisely controlled.

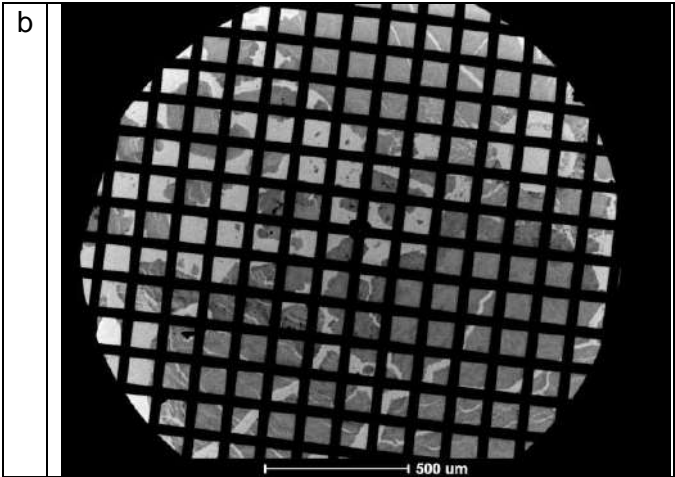
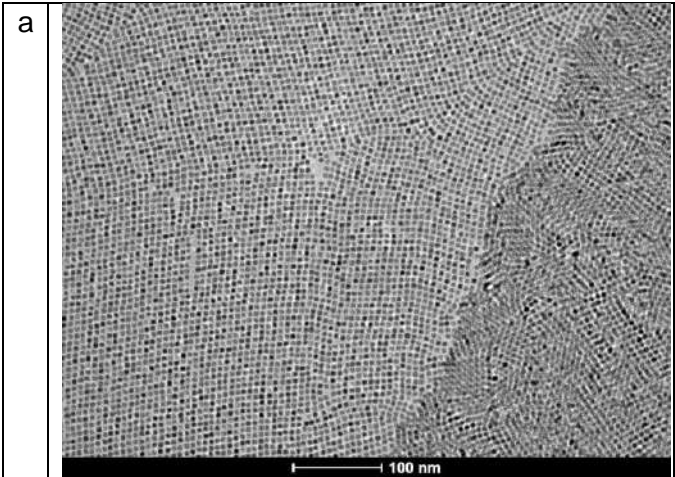


Figure 9 TEM show images for mono and bilayer QDS film from a low concentration, 0.034 mM, ink. Image 9a shows a small area and 9b shows the full TEM film. These TEMs were used to help estimate the volume of ink transferred.

QDS inks were developed with varying concentrations and deposited on ethylene glycol to then be analyzed with TEM images. At the lowest concentration, shown in figure 9, ink the layers were observed to be on average 1.5 layers thick relatively consistently across the film. Using this layer thickness estimate the volume transferred was back calculated to be around 45 uL per droplet.

Concentration (mM)	Particles/L	Layers	Particles/nm	Volume (nL)
3.43E-02	2.07E+19	1.5	0.0175	39.91
5.15E-02	3.10E+19	2.25		
8.58E-02	5.17E+19	3.75		

Figure 10 shows the calculations to determine the volume being transferred by the needle in DPL.

The 45 uL volume estimate was used to determine what layer thickness higher concentrated inks would result in. These calculations were shown to be within an order of magnitude of what the respective TEMs had shown, which supported the initial volume estimate.

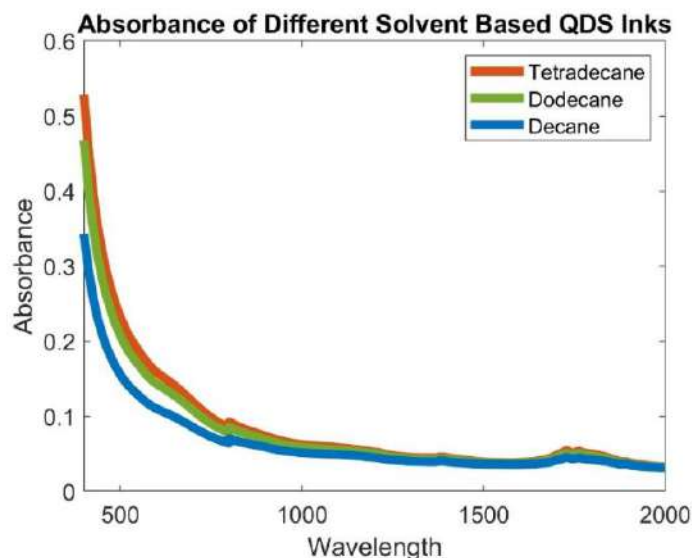


Figure 11 is a UV-VIS absorbance spectrum with three ink samples at the same concentration that underwent 20 DPL ink transfers. This graph illustrates that more ink is transferred with DDE and TDE than DE. So viscosity does impact the amount of ink transferred.

Solvent	Volume Transferred (nL)
Decane	29.22
Dodecane	39.91
Tetradecane	45.1

Figure 12 using the data from figure 10 and 11 the volume of ink transferred in DPL based on solvent type was calculated.

Next a series of samples were taken with the same concentration but varying the solvent used in the ink: DE, DDE, and TDE were used. The DPL technique was completed for twenty ink transfers to be analyzed using UV vis. The UV vis data varied between these inks, but all these inks have the same chemical properties from the decane based structure with the only difference being the viscosity. Figure 12 shows respectively how much the volume transfer varies between solvent types. This demonstrated that viscosity of the solvents used in DPL will have an impact on the amount of ink transferred, with a higher viscosity transferring more ink.

### Comparing Solvents for QDS Inks

How the inks dry effect the final film in terms of consistency in layer thickness, amount of cracks, and overall film morphology. Three different decane solvents were used in this study: decane (DE), dodecane (DDE), and tetradecane (TDE).

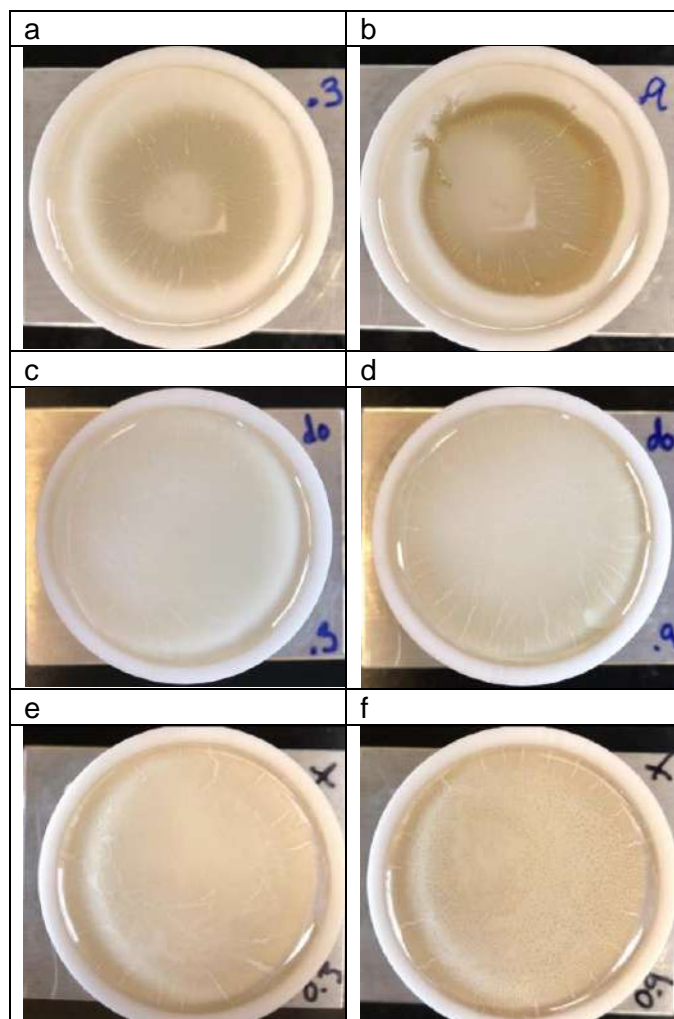


Figure 7 illustrates each final drying pattern for DE (a-b), DDE (c-d), and TDE(g-h) solvent-based inks. The left column is at 0.3uL volume and the right column is at 0.9 uL volume transferred. These transfers were completed using a micropipette.

While DE dries uniformly from the outer edges inward, with a few small cracks forming in the film after drying is complete. Both DDE and TDE show small circular droplets forming uniformly across the surface after wetting is complete but before drying begins. At high concentrations these droplets are visible in the film after drying. But these films have less breaking than the DE films do, this could be in part due to the drying time being and order of



magnitude larger for DDE and two orders of magnitude larger for TDE, with a significantly longer drying time allowing for a less cracked film. Drying dynamics will be discussed further later in the paper.

### Layer Consistency and Reproducibility

Experiments were completed to reproduce the QDS transfer at different concentrations in order to analyze the consistency of ink transfer from the needle to the liquid layer. Pictures were taken after the inks completed drying and then were analyzed using an image analysis software to get grey scale color data.

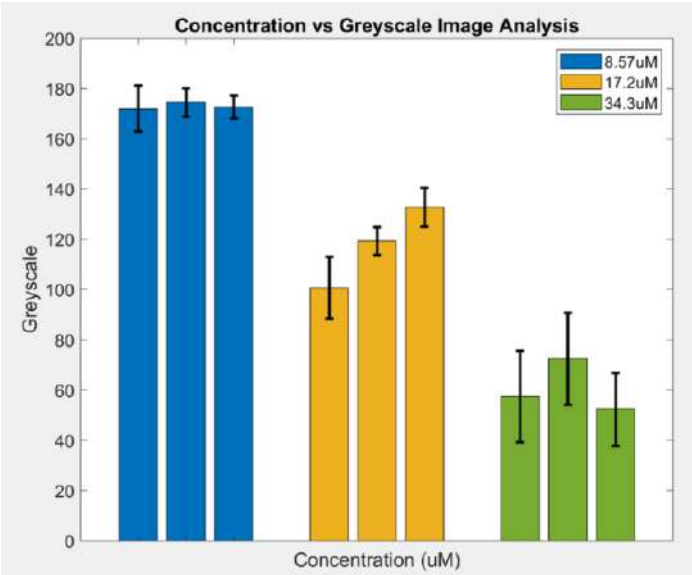


Figure 11 shows the ink concentration deposited with DPL versus the grey scale image analysis completed on the image. With the increasing concentration the images become darker. Each point represents the average greyscale point from three images.

With increasing concentration, the images get increasingly darker on average. Using this data ink concentration could be estimated based on the greyscale of the film under similar lighting conditions. This data shows some regularity and consistency in the amount of ink transferred in DPL.

### Drying Dynamics

The drying dynamics of the QDS inks vary depending on the solvent base for the ink used.

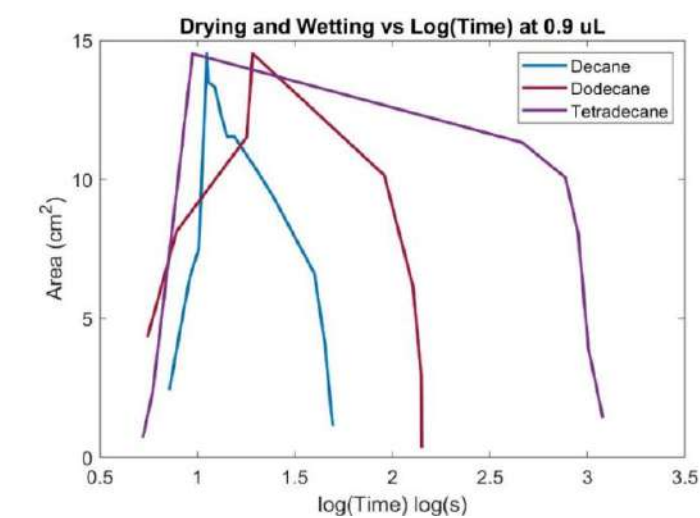


Figure 8 graphs showing the wetting and drying time by the area of the circular ethylene glycol filled through covered, time is graphed on a log plot.

While wetting the droplet expands out covering the entire area and then dries from the outside of the circular through inward. Image analysis was completed on videos of the wetting and drying process of low volumes (0.1 uL to 0.9 uL range) of QDS ink with DE, DDE, and TDE as the solvents used. Similarities existed in the way the ink would spread out in a regular fashion to the outer edges of the circular trough. A micropipette was used in these studies instead of a needle as the videos were completed on a much larger volume scale than the needles are able to transfer. DE drying time is about 1.5 min, DDE is around 2.5 min, and TDE is around 30 min. The longer drying time may allow for easier transfer of QDS ink from the needle to the liquid surface, as such a small volume is being transferred part of the ink could dry before transfer occurs.

### General Morphology

a	b
---	---

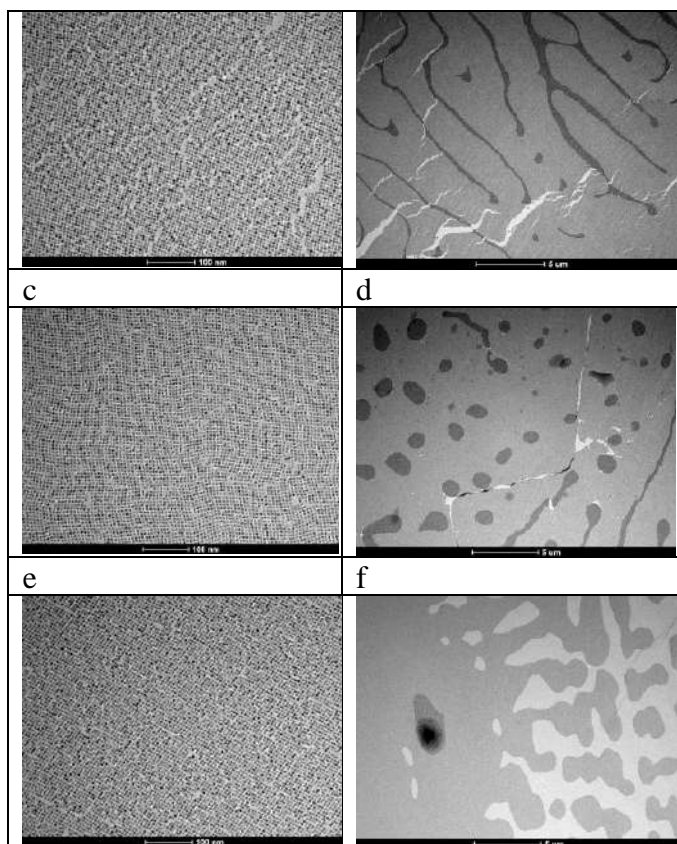


Figure 8 (a-f) shows TEM images of 1-2 multilayer films made from DE, DDE, and TDE respectively from top to bottom. The left images show the films in the 100nm size range and the right images show films in the 5 μm size range.

The films all show smooth mono to bilayered QDS films. This shows that the final morphology and film type is not significantly different between DE, DDE, and TDE in terms of the film in the 100nm range. Though with increasing chain length (from DE, DDE, and TDE) and increasing drying time there are fewer cracks and thus increasingly smoother more consistent films. There is also an increasing area of the bilayer film and less monolayer film with the increasing chain length which is caused by the increased volume transfer due to the viscosity as discussed previously.

## Conclusion

The study illustrates how dip pen lithography can be used on liquid surfaces in order to make uniform quantum dot solid films on the micro and nano scale. The control of experimental parameters such as placement, concentration, solvent, and volume provide more control of the process in order to

determine film thickness and size as small as an area covering  $1\text{mm}^2$ . The ability to deposit small controlled volumes of QDS ink can allow for novel applications. The size scale aids the development of functional complexity for applications in the miniaturization of electronics.

With instruments like a z-stage, Atomic Force Microscopy (AFM), and Nano eNabler Molecular Printing (NEMP) System the deposition speed of the ink transfer is able to be fully controlled. In future experiments AFM and NEMP will be tested more extensively with the QDS ink in order to determine ability of scale up. The small scale that is being used allows to move between different types of assemblies with potential future application in developing arrays or microfabricating unique quills and moving away from traditional needles.

## References

- [16] Minemawari, Hiromi, et al. *Nature*, vol. 475, ser. 364, 13 July 2011. 364, doi:<https://doi.org/10.1038/nature10313>.
- [14] *hem. Mater.*200416173318-3322, Publication Date: July 17, 2004, <https://doi.org/10.1021/cm049476y>
- [1] S. D. Stranks, H. J. Snaith, *Nature Nanotechnology* 10 (2015) 391.
- [2] W. R. Mateker, M. D. McGehee, *Advanced Materials* 29 (2017).
- [3] J. Correa-Baena, A. Abate, M. Saliba, W. Tress, T. J. Jacobsson, M. Gratzel, A. Hagfeldt, *Energy & Environmental Science* 10 (2017) 710.
- [6] Yan, H. *et al.* A high-mobility electron-transporting polymer for printed transistors. *Nature* **457**, 679–686 (2009)
- [7] Rivnay, J. *et al.* Large modulation of carrier transport by grain-boundary molecular packing and microstructure in organic thin films. *Nature Mater.* **8**, 952–958 (2009)
- [4] *ACS Appl. Mater. Interfaces*20181043739-3749, Publication Date: January 11, 2018, <https://doi.org/10.1021/acsami.7b13997>
- [5] *ACS Appl Mater Interfaces*. 2018 Feb 14; 10(6): 5626–5632. Published online 2018 Jan 25. doi: [10.1021/acsami.7b16882](https://doi.org/10.1021/acsami.7b16882)

- [7] Genome Res. 2003 Oct; 13(10): 2348–2352.  
doi: [10.1101/gr.623903](https://doi.org/10.1101/gr.623903)
- [8] Kim, K. , Moldovan, N. and Espinosa, H. (2005),  
A Nanofountain Probe with Sub-100 nm  
Molecular Writing Resolution. *Small*, 1: 632-  
635. doi:[10.1002/sml.200500027](https://doi.org/10.1002/sml.200500027)
- [9] Appl. Phys. Lett. 93, 143105 (2008);  
<https://doi.org/10.1063/1.2995859>  
Submitted: 29 August 2008 . Accepted: 09  
September 2008 . Published Online: 07  
October 2008
- [10] Salaita, K. , Wang, Y. , Fragala, J. , Vega, R.  
A., Liu, C. and Mirkin, C. A. (2006),  
Massively Parallel Dip–Pen  
Nanolithography with 55 000-Pen Two-  
Dimensional Arrays. *Angewandte Chemie  
International Edition*, 45: 7220-7223.  
doi:[10.1002/anie.200603142](https://doi.org/10.1002/anie.200603142)
- [11] Hynes, W., Gracias, A., Fahrenkopf, N., Raof,  
N., Raja, W., Lee, K., . . . Cady, N. (2009).  
Direct Cell Printing With Microfabricated  
Quill-Pen Cantilevers. *MRS  
Proceedings*, 1235, 1235-RR06-02.  
doi:10.1557/PROC-1235-RR06-02
- [6] BY RICHARD D. PINER, JIN ZHU, FENG  
XU, SEUNGHUN HONG, CHAD A.  
MIRKIN, *SCIENCE* 29 JAN 1999 : 661-663
- [12] Rizzo, A. , Mazzeo, M. , Palumbo, M. ,  
Lerario, G. , D'Amone, S. , Cingolani, R.  
and Gigli, G. (2008), Hybrid Light-Emitting  
Diodes from Microcontact-Printing Double-  
Transfer of Colloidal Semiconductor  
CdSe/ZnS Quantum Dots onto Organic  
Layers. *Adv. Mater.*, 20: 1886-1891.  
doi:[10.1002/adma.200701480](https://doi.org/10.1002/adma.200701480)
- [13] *Nano Lett.* 2004 4:141-44, Publication  
Date: December 3, 2003  
<https://doi.org/10.1021/nl034851r>
- [15] *Chem. Mater.* 2007 19:2561-6106  
Publication Date: November 15, 2007  
<https://doi.org/10.1021/cm071410q>

# The Assembly of Magnetic Panels: Learning from Molecules

Kayleigh Jones,<sup>1,2,\*</sup> Ran Niu,<sup>2,3</sup> Yunus Kinkhabwala,<sup>2,3</sup> Samuel Whitehead,<sup>2,3</sup> and Itai Cohen<sup>2,3</sup>

<sup>1</sup>*Department of Physics, The University of Texas at Austin, Austin, TX 78712*

<sup>2</sup>*Cornell Center for Materials Research, Cornell University, Ithaca, NY 14850*

<sup>3</sup>*Laboratory of Atomic and Solid State Physics, Cornell University, Ithaca, NY 14850*

(Dated: August 7, 2019)

Micro-scale technology has become increasingly desirable because of the potential to store more data, process information more efficiently, and perform functions that were previously impossible. The objective of this project is to study the mechanical properties of macro-scale, magnetic, polymer analogues with the intent to fabricate them at the colloidal-scale. These magnetic panels consist of programmable dipole patterns and, with varying design, they have the potential to become self-assembling strands. This paper focuses on the persistence length of a panel strand and how to potentially tune the persistence length using different panel designs.

## I. INTRODUCTION

For billions of years, molecular biology has had time to evolve and correct itself. DNA was created to store genetic information, and RNA was created for protein synthesis, just to name a few of nature’s inventions. Both molecules were built to complete a detailed and purposeful function. However, humans today have evolved and thus must address more urgent questions. What if petabytes of data could be stored the same way billions of DNA base pairs are stored? What if information were processed similar to how RNA processes genetic code? By taking inspiration from years of evolution, we can more effectively approach problems that biology has already solved.

Suppose we could draw inspiration from the physical properties and functionality of a polymer such as DNA/RNA and make it our own. In doing so, we create magnetic panels - magnetic, colloidal-scale panels, with dipole patterns analogous to Watson-Crick base pairs (Fig. 1A). Though inspired by molecules, they differ from any biological polymer in that their binding energies and magnetic interactions are programmable. Thus, we could change the physical properties of these magnetic panels to fit a specific need. Manufacturing such a device would open new possibilities for information storage and smart, micro-scale, functional structures.

Such an ambitious project requires collaboration involving nano-manufacturing, simulations, and macro-scale testing. The last of the three is where this paper will focus.

## II. MATERIALS AND EXPERIMENTAL SETUP

### A. Why use magnets?

Current experimentation with micro-scale, 3D assemblies often takes days to complete. Waiting for complex

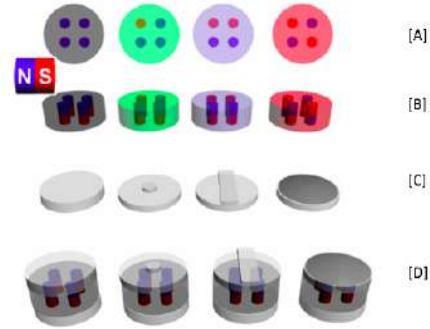


FIG. 1. Panel design and assembly. [A] shows the four dipole patterns, [B] shows the main panel body, [C] shows the different kinds of panel spacers, and [D] shows the assembled magnetic panel.

polymer systems to assemble often requires time because polymers, like DNA, rely on electrostatic interactions to form. The polymer is screened in solution, meaning its short-range, electrostatic forces are often interrupted by a charge in the solution. In contrast, magnetic interactions are not screened in solution. Magnetic panels rely on dipole and multipole interactions to form, and thus have a much more direct assembly. The panels’ magnetic interactions will also aid in a faster assembly on account of the system’s free energy. The free energy of the magnetic panels is dominated by entropy (rather than enthalpy) and thus allows the assembly to quickly reach a stable state.

Furthermore, magnetic interactions are scalable. If the ratio between two magnetic energies is taken at the macro-scale, then it will stay consistent at the micro-scale. This allows our understanding of the panels at a large scale to be easily translated to a smaller scale.

Lastly, there is existing technology to program magnetic domains onto colloidal-scale devices. This is important because it allows us to adjust the magnetic binding energy ( $U_{mag}$ ) of the panels while maintaining the desired scale.

\* kayleigh.jones@utexas.edu



## B. Macro-scale Panel Fabrication

Fabrication of the magnetic panels at the macro-scale is relatively simple. The process begins with a sheet of acrylic that is laser-cut into a centimeter-wide, circular pattern (Fig. 1B). This serves as the body of our panel.

Next, this body is given an acrylic base, called a spacer. This spacer can be cut with a variety of desired textures (Fig. 1C). Next, four magnets are embedded in the body of the panel. The dipole moment of each magnet can be manipulated to create four different dipole patterns (Fig. 1A). Finally, the assembly is capped with another spacer (Fig. 1D). The whole ensemble is held together with fast-drying glue.

All designs are mindful of our goal to fabricate panels at the micro-scale. Thus, each panel design is possible to create at a much smaller scale.

## C. Experimental Setup

After assembly, the panels are brought together into a full strand and placed in a dish that sits upon a shielded, electromagnetic shaker. This shaker vibrates at a given frequency and amplitude.

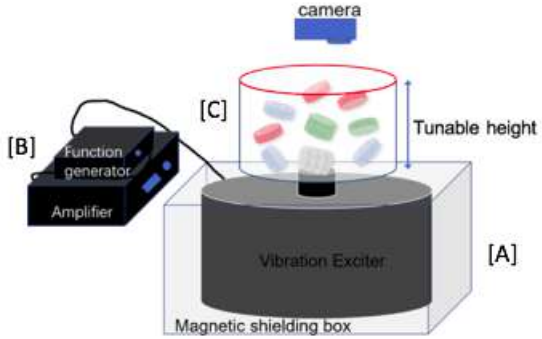


FIG. 2. Experimental setup for exciting panels with an effective temperature,  $\tau_{eff}$ . [A] is the EM shaker, [B] is the function generator and amplifier, and [C] is the dish that holds the magnetic panels

However, what is important is the acceleration that is given to each strand of panels. The acceleration can be understood with the following:

$$\Gamma = (2\pi\nu)^2 A$$

$\Gamma$  is the acceleration of the strand and is manipulated by changing the amplitude of the shaker,  $A$ . The frequency  $\nu$  of the system is held constant.

## D. Dipole Pattern and Spacer Type

There are three important factors that contribute to the flexibility of a magnetic strand. The first is the acceleration of the strand and has already been discussed. The other two are the dipole pattern (Fig. 1A) and spacer type (Fig. 1C).

There are four dipole patterns that can be created with the four embedded magnets in a panel. Each dipole pattern is distinguished with a color and characterized with different binding energies (Fig. 3).

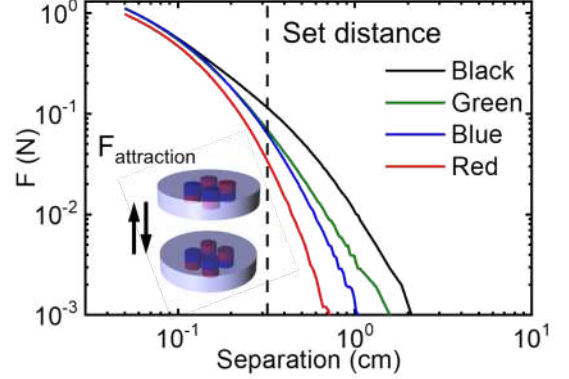


FIG. 3. The attractive force of each dipole pattern at a given separation distance.

## E. Calculating Persistence Length

Persistence length is a mechanical property of a polymer that determines how flexible or stiff the polymer strand is. It is calculated by measuring the correlation of two tangent vectors at a given separation distance along the strand (Fig. 4). The separation distance is plotted versus the average cosine value ( $\langle \cos(\theta) \rangle$ ) of the angle between the two vectors. The decay of this curve is what quantifies the persistence length. If the polymer strand is very stiff, the two tangent vectors would be highly correlated at any distance on the chain. This plot is characterized by a slow decay and thus has a large persistence length. If the polymer strand is very bendy, the tangent vectors would quickly become uncorrelated and produce a plot with a slow decay, indicating a small persistence length. This relationship can be understood by the following equation, where  $l$  is the separation distance and  $p$  is the persistence length.

$$\langle \cos(\theta) \rangle = e^{-l/p}$$

This property is useful to know when trying to understand the polymer's movement and self-assembly. This project's main focus was to measure the persistence length of various strands of magnetic panels.

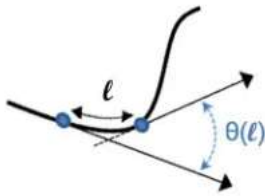


FIG. 4. A schematic explaining the definition of persistence length. *Lamour G, Kirkegaard JB, Li H, Knowles TP, Gsponer J. Easyworm: an open-source software tool to determine the mechanical properties of worm-like chains.*

The first step to calculating persistence length was to take a video of the magnetic panels. The panels were assembled into a strand, placed in the shaker, and given their highest possible effective temperature ( $\tau_{eff}$ ) without accelerating so much that they break.

Next was to write a program using Matlab, a programming language commonly used for image analysis. The written script takes frames from the aforementioned video and reduces each image of our strand to a skeleton (Fig. 5). Then, it creates two tangent vectors, defined at varying panels, for varying separation distances.



FIG. 5. Skeletonized image of a 15-panel, green, magnetic strand with a dome-spaced spacer.

Using trigonometry and the x,y coordinates of each panel, the Matlab script assigns a theta value for each vector, and then it calculates a delta theta between the two vectors ( $\Delta\theta = \theta_2 - \theta_1$ ). This  $\Delta\theta$  is what acts as our angle between the two vectors. Then, the script takes  $\text{Cos}(\Delta\theta)$  and averages these values across frames, for every separation distance. These are the values that get plotted and analyzed.

Writing and modifying this Matlab program consumed the majority of this summer project. Because of this, the following experimental results represent quick tests to see if the code works as it should. Future work would involve a more in-depth analysis of the magnetic strands' physical properties, whereas this project mainly involved creating the script that calculates persistence length.

### III. EXPERIMENTAL RESULTS AND DISCUSSION

The first and only test began by comparing a flexible magnetic strand with a slightly stiffer strand. We pre-

dicted that by changing the spacer type and keeping the dipole pattern constant, we would see a change in the calculated persistence length. We recorded two videos: one of a green, 20-panel strand with the dot small dot spacer (second design from the left in Fig. 1C), and another of a green, 15-panel strand with the hemisphere spacer (fourth design from the left in Fig. 1C). Running the videos through the Matlab script produced a plot that quantified persistence length (Fig. 6). By fitting a negative exponential to each curve, we were able to estimate the persistence length values for each strand. The estimated value for the small dot strand is 12 panels, and the estimated value for the hemisphere strand is 5 panels. The persistence length is the length at which thermal fluctuations can cause a bend in the strand. According to the Matlab script, this happens to the dot strand and hemisphere strand at 12 panels and 5 panels, respectively.

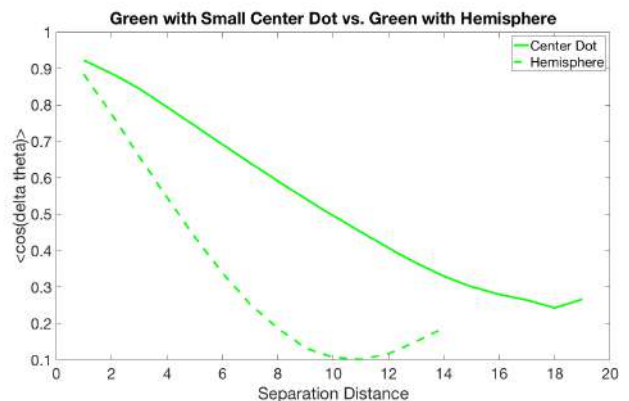


FIG. 6. Plot of  $\langle \text{Cos}(\theta) \rangle$  values versus separation distance for a green, 20-panel strand with the dot small dot spacer and a green, 15-panel strand with the hemisphere spacer. The exponential decay of each plot is what characterizes the strand's persistence length

Despite producing values for persistence length, this analysis and the statistics behind it should be given more attention. We are assuming that the magnetic strands act as an ideal polymer does. This means that as the strand is given an effective temperature, it will be free to move with randomized motion. In doing so, it produces the exponential decay that we expect. We predict, however, that some of our magnetic strands do not behave as an ideal polymer does. The magnetic strands may inherit a bent resting state due to their asymmetric dipole patterns. Take the green, 20-panel strand with the dot small dot spacer, for example. The green panels have one south-facing dipole and three north-facing dipoles (Fig. 1A). This means that when the panels are assembled into a strand with spacers that allow it to bend, the resting strand starts to curve. This is because the three, north-facing dipoles in one panel will more strongly attract to the three, north-facing dipoles in the next panel than the south-facing dipoles in each panel will. Because the strand takes on this natural bent shape, it does not move

randomly when excited in the shaker and does not act as an ideal polymer. This constrained rather than randomized motion may produce error in the graphs that the Matlab code produces. This idea may be responsible for the curled ends of the plots, but this is yet to be explored.

#### IV. FUTURE WORK

First and foremost, this procedure of quantifying persistence length for our magnetic strands must be refined and expanded. Immediate goals would include improving the accuracy of the Matlab script and analyzing longer videos. Yet, the majority of the next project would consist of testing the hypothesis that states our magnetic panels act differently from ideal polymers. Once the analysis stage has reached an adequate standard, the work would begin to include using the persistence length of different strands to create more complicated and mixed structures. One could begin to record videos of a strand with half red panels and half black panels, for example. Studying mixed strands could open possibilities for better replicating more complicated, self-assembling copolymers.

However, the overall project involving magnetic panels is still in its exploratory stages. This paper describes

panels that have out-of-plane dipole patterns, but possibilities like in-plane dipole patterns still have yet to be experimented on. Similarly, this paper mentions 2x2 dipole patterns and thus four different binding energies, but 3x3 dipole patterns must be explored as well. Once the magnetic panels are understood more thoroughly at the macro-scale, projects will focus on translating the found mechanical properties of these macro-scale experiments to the colloidal and micro-scale. This stage will be completed by a collaboration with the McEuen group at the Cornell NanoScale Science and Technology Facility (CNF).

#### V. ACKNOWLEDGEMENTS

This work was overseen primarily by Dr. Ran Niu and Professor Itai Cohen. From them, I received excellent mentorship and a warm welcome. A special thanks should also go to Yunus Kinkhabwala and Samuel Whitehead for helping to teach me about image analysis and programming in Matlab. The Cohen Lab Group as a whole helped guide me through a summer of productivity and growth. The Summer 2019 CCMR REU program is funded by the NSF REU Site program (DMR-1757420) and the NSF MRSEC program (DMR-1719875).

- 
- [1] G. Lamour, “Easyworm: an open-source software tool to determine the mechanical properties of worm-like chains,”.
  - [2] Y. Mai, “Self-assembly of block copolymers,” (2012).

# Decreasing Electrolyte Decomposition to Stabilize High Voltage Organic Battery Systems

Rachel Lawless and Héctor Abruña

## Abstract

High voltage battery systems are extremely promising as increased voltage means higher energy densities for batteries. The polymer poly(Triarylamine-Phenazine) has two stable, accessible redox couples in traditional battery electrolytes, while a third redox couple sits just outside the electrolyte stability window. Access of this third redox couple in an appropriate solvent would increase both the average operating voltage as well as capacity of the material, translating to an increased energy density. Here, solvents with adiponitrile (ADN) and sulfolane (TMS) were used as additives to stabilize the electrolyte solvent in order to improve the battery performance. TMS showed to be the more promising electrolyte with only 30  $\mu\text{A}$  of current decomposition and only a 13% loss in capacity over 100 cycles. ADN showed higher losses in capacity but also showed lower decomposition around 20  $\mu\text{A}$ . In addition to the employed additive, the current collector also had a large effect on decomposition, and the carbon coated aluminum collector lowered the decomposition from 200  $\mu\text{A}$  to only 20  $\mu\text{A}$  for the high performing solvent systems.



## Introduction & Background

Organic cathodes have proven to be advantageous compared to traditional lithium metal oxide cathodes as they are naturally abundant and environmentally friendly. Although there are also several drawbacks to these materials as well. Organic materials have low gravimetric density and small organic materials tend to dissolve in electrolyte which leads to decay in the battery performance over time. This dissolution can be counteracted by using the small molecules as monomers to form a larger polymer. This can significantly increase stability and cycling performance, however size dispersity of the polymer chains can result dissolution of smaller oligomers. To combat this, crosslinking has proven to be an effective method to reduce dissolution.

Previously, the polymer cathode poly(triarylamine phenazine) (poly(TAA-PZ)) has been researched and shown high rate and stability but only moderate capacities (1). This lack of capacity is due to the additional mass added from the cross-coupling molecule that adds to the stability of the system. However this cross-coupling molecule can undergo a redox event as well. This third redox event, if accessed, can improve the specific capacity significantly as more electrons will be transferred without increasing the mass of the system significantly.

The difficulty in accessing the third peak is the limited voltage window of the typical solvent system, EC:DEC (Ethylene carbonate: Diethyl Carbonate) with  $\text{LiBF}_4$  or  $\text{LiPF}_6$ . This solvent system is limited to a maximum voltage of 4.5 V and the third redox event occurs at a voltage of approximately 4.8 V.

Previously there has been work investigating various chemicals to help electrolytes reach higher voltages. There are several options including ionic liquids, sulfones

and aliphatic dinitriles (2). In this paper, aliphatic dinitriles and sulfones are investigated.

Adiponitrile was the aliphatic dinitrile investigated. Adiponitrile was used as it promises a high voltage stability window, over 6 V vs  $\text{Li/Li}^+$  (3). Unfortunately, it does have a high viscosity of 6 cP which is larger than that of the typical solvent system used. Due to this high viscosity, adiponitrile was used as an additive to limit its effect on the viscosity. Sulfolane was the sulfone investigated and similarly to the adiponitrile it was only used as an additive.

## Experimental

Coin cells were prepared with poly(TAA-PZ) as the cathode material in various electrolytes and on various current collectors. Two chemicals were used as additives to stabilize the solvents, adiponitrile (ADN) and sulfolane (TMS). These were added mostly to a mixtures of EC, DEC, and dimethyl carbonate (DMC) at different ratios. The electrolyte salts were either  $\text{LiBF}_4$  or  $\text{LiPF}_6$ . Different current collectors were also used. The standard collector used was carbon paper, but carbon coated aluminum foil was used as well in order to replicate more standard non-organic conditions.

## Results & Discussion

Table 1. Solvents components for  $\text{LiPF}_6$  systems

Base solvent	Additive
EC:DEC:DMC	1 wt% ADN
EC:DEC:DMC	5 wt% ADN
EC:DEC	1 vol% ADN
EC:ADN	N/A

The first set solvents looked at used  $\text{LiPF}_6$  salts on a carbon paper current collector and can be seen in Table 1. These were picked based on references in literature (4,5). Cells were made with these solvents and cycled for 500 cycles at 1 A/g.

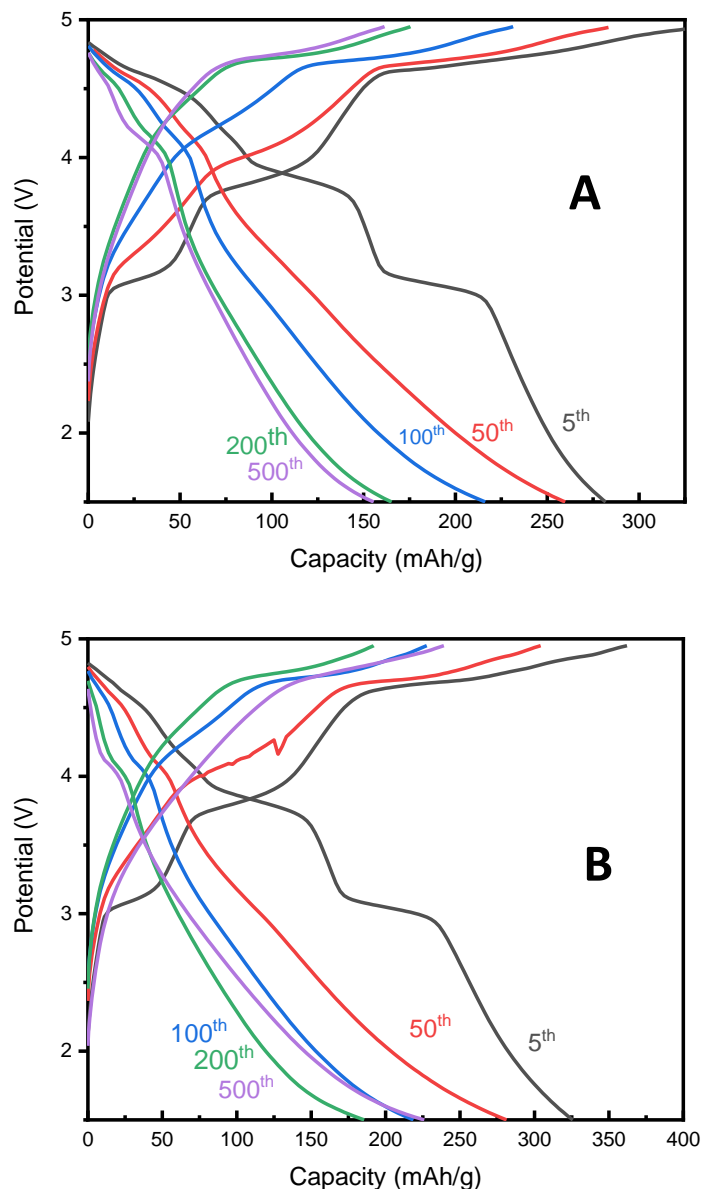


Figure 1. Charge discharge curves for the cells with (a) EC:DEC:DMC 1 wt% ADN  $\text{LiPF}_6$  and (b) EC:DEC:DMC 5 wt% ADN  $\text{LiPF}_6$

The EC:DEC:DMC and low wt% ADN solvent cells showed significant degradation over 500 cycles. Figure 1 shows their charge discharge curves and clear disappearance of the plateaus can be seen. Cycle five for both cells exhibits three defined plateaus. At the end of the 500 cycles the plateaus were barely visible and the batteries showed capacity losses around 125 mAh/g. The amount of ADN added had some effect. The 5 wt% ADN solvent showed less defined plateaus throughout cycling even at earlier cycles.

Another solvent was made using 1 vol% ADN and removed DMC to see if DMC had any effect on the battery performance. Looking at Figure 2 it's clear that DMC does have a large effect. In the solvent without it the highest voltage plateau is less stable, but the other two were still visible even at 50 cycles.

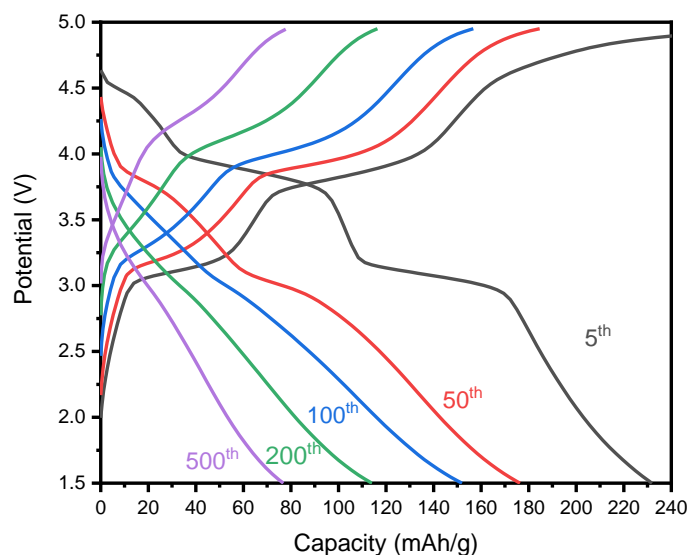


Figure 2. Charge discharge curves of EC:DEC 1 vol% ADN  $\text{LiPF}_6$  over 500 cycles from 1.5V to 4.95V

The effect of ADN was further investigated and 1:1 mix of EC and ADN was made. This cell showed poor stability with the capacity decreasing to only 60 mAh/g by the 500<sup>th</sup> cycle. The process of this degradation is shown in Figure 3. The

highest voltage plateau was never, but there was still a faint plateau present even at 200 cycles.

values significantly higher than that are most likely caused by electrolyte decomposition.

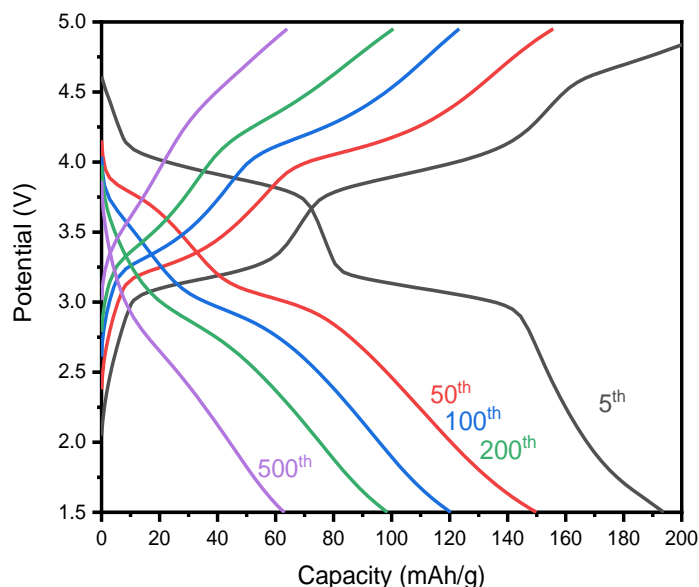


Figure 3. Charge/discharge curves of EC:ADN LiPF<sub>6</sub> over 500 cycles from 1.5V to 4.95V

To further understand the behavior of the batteries in the four different solvents we tested, cells were made that had no active material only the carbon paper current collector. These cells were then cycled from 1.5 V to 5 V at 5 mV/s. Figure 4 shows the cyclic voltammetry results from this cycling. The solvent systems with DMC had the highest decomposition. This explains the faster degradation of plateaus shown in the charge/discharge curves. The EC:ADN LiPF<sub>6</sub> solvent showed the lowest decomposition, but its poor performance could be due to the solution's increased viscosity.

Further comparisons can be drawn looking at the capacity of these battery systems over 500 cycles. Figure 5 shows their discharge capacity from constant cycling at 1 A/g. It can be seen the solvents with the DMC included showed the highest capacities, but as seen by the blank cells this increased capacity is due to the decomposition of electrolyte. The theoretical capacity of Poly(TAA-PZ) is 204 mAh/g so any

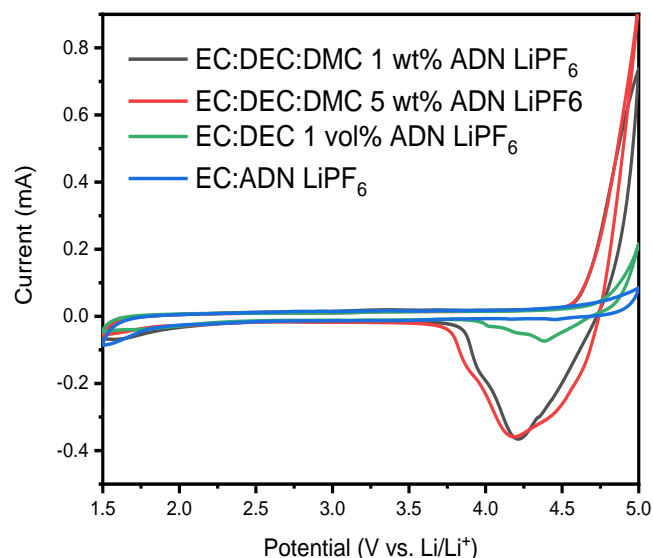


Figure 4. Cyclic Voltammetry of the first 4 solvent systems. Cycled from 1.5 V to 5 V at 5 mV/s

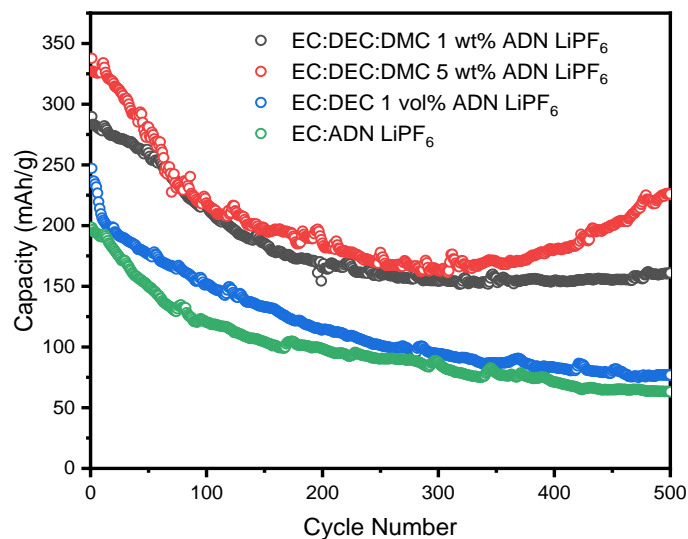


Figure 5. Capacities of the Poly(TAA-PZ) batteries with various solvents over 500 cycles at a constant current of 1 A/g

All the solvent systems investigated so far have used LiPF<sub>6</sub> as their salt. In order to understand the effect the salt plays on accessing the third peak and stability of cycling similar solvent systems were made using LiBF<sub>4</sub>. Table 2

shows which solvents were used to make the  $\text{LiBF}_4$  on Carbon Paper systems.

Table 2. Solvent components in  $\text{LiBF}_4$  systems

Base solvent	Additive
EC:DEC:DMC	1 wt% ADN
EC:DEC	1 vol% ADN
EC:ADN	N/A

First the EC:DEC:DMC 1 wt% ADN solvent's cycling performance is shown in Figure 6. Comparing this to the charge discharge curves with  $\text{LiPF}_6$  salt a stark difference in the size of the highest voltage plateau was seen. Despite this a similar degradation was observed over the 500 cycles.

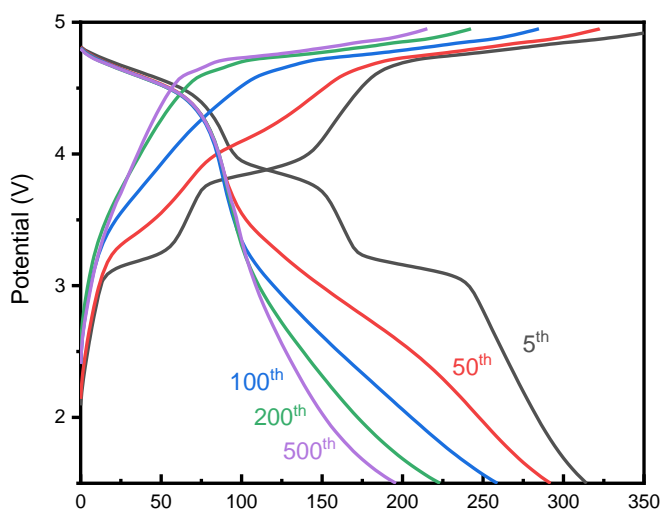


Figure 6. Charge discharge curves of EC:DEC:DMC 1 wt% ADN  $\text{LiBF}_4$  over 500 cycles from 1.5V to 4.95V

The EC:DEC 1 vol% ADN solvent in  $\text{LiPF}_6$  salt once again demonstrated the effect of DMC. Without the DMC the cell maintains clearly defined plateaus longer as seen in Figure 7. The effect of the  $\text{LiBF}_4$  was observed here as well. In comparison to the same solvent in  $\text{LiPF}_6$  the highest voltage plateau is much larger and

more stable as was shown in the other  $\text{LiBF}_4$  solvents as well.

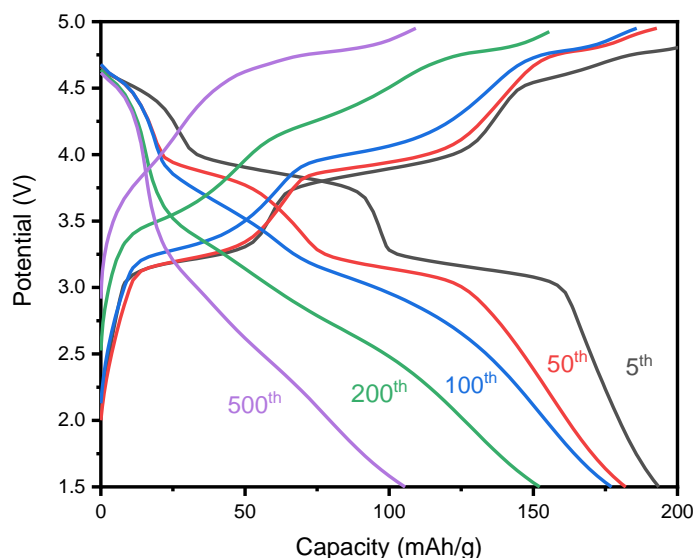


Figure 7. Charge discharge curves of EC:DEC 1 vol% ADN  $\text{LiBF}_4$  over 500 cycles from 1.5V to 4.95V

The pattern seen with the other solvents in  $\text{LiBF}_4$  held up when looking at EC:ADN  $\text{LiBF}_4$  as well. Figure 8 shows the charge discharge curves from this system. Once again the larger presence of the highest voltage plateau was shown

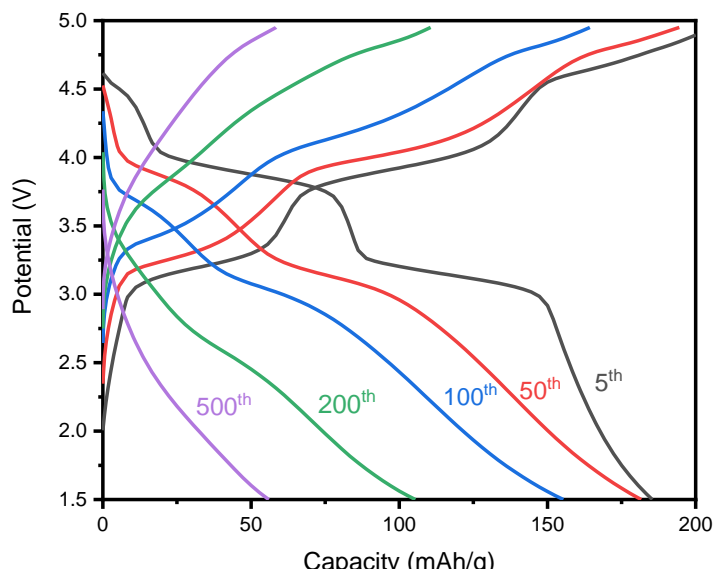


Figure 8. Charge discharge curves of EC:ADN  $\text{LiBF}_4$  over 500 cycles from 1.5V to 4.95V



while there was also a similar behavior between the different salts in the lower voltage plateaus. The EC:ADN mix does maintain some part of them through 100 cycles.

Coin cells without any active material were prepared using the  $\text{LiBF}_4$  solvents in order to see how the solvent decomposes. Figure 9 shows their decomposition after cyclic voltammetry. Once again the solvent with DMC shows the highest decomposition of all solvent systems. In comparison to the  $\text{LiPF}_6$  solvent solutions the decomposition seems to be higher in the  $\text{LiBF}_4$  systems for each respective solution.

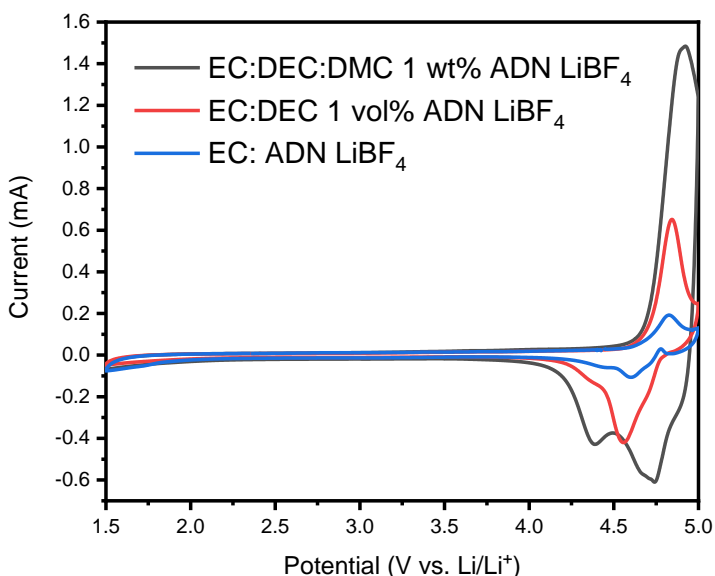


Figure 9. Cyclic Voltammetry of the  $\text{LiBF}_4$  solvent systems. Cycled from 1.5 V to 5 V at 5 mV/s

The capacity over 500 cycles was also analyzed for the  $\text{LiBF}_4$  solvents. The results are shown in Figure 10. The high decomposition of the DMC solvent once again increased the capacity of the cell, similarly to the increase that was observed in the solvents with  $\text{LiPF}_6$ . The solvents without DMC showed less degradation and higher capacity after 500 cycles than the same solvents in  $\text{LiPF}_6$ .

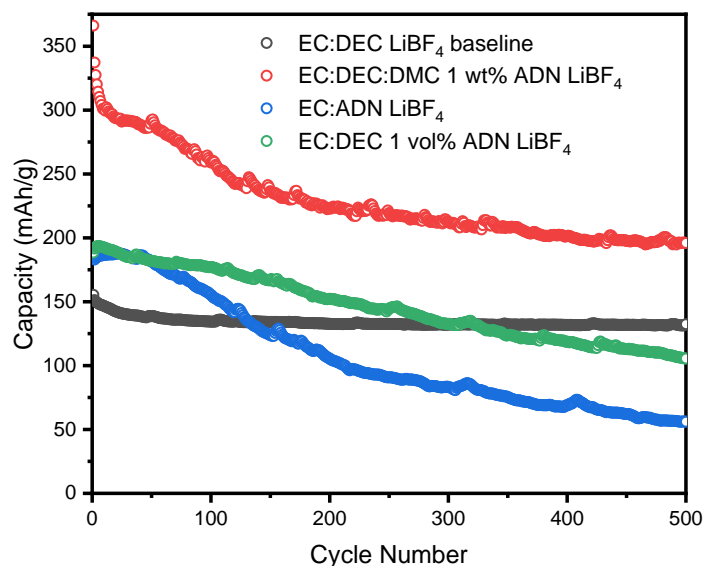


Figure 10. Capacities of the Poly(TAA-PZ) batteries with various  $\text{LiBF}_4$  solvents over 500 cycles at a constant current of 1 A/g

From studying the effects of salt, several solvents were shown to have low decomposition. The 4 solvents with the lowest decomposition were EC:ADN  $\text{LiBF}_4$ , EC:ADN  $\text{LiPF}_6$ , EC:DEC 1 vol% ADN  $\text{LiPF}_6$ , and EC:DEC 1 vol% ADN  $\text{LiBF}_4$ . Of these solvents the low volume percent ADN cells had better performance due to their decreased viscosity.

Despite the decreases in decomposition the performance of the cell still wasn't at the desired level. A possibility was the large difference between the battery systems used here and those in literature. Much of the research with adiponitrile has been done with lithium metal oxides on aluminum current collectors (6), but the systems being investigated here are organic and being placed onto carbon paper current collectors. To match more closely to literature conditions some of the higher performing solvent systems were tested with the Poly(TAA-PZ) placed onto carbon coated aluminum current collectors. The solvents used were EC:DEC 1 vol% ADN with  $\text{LiPF}_6$  and  $\text{LiBF}_4$ .

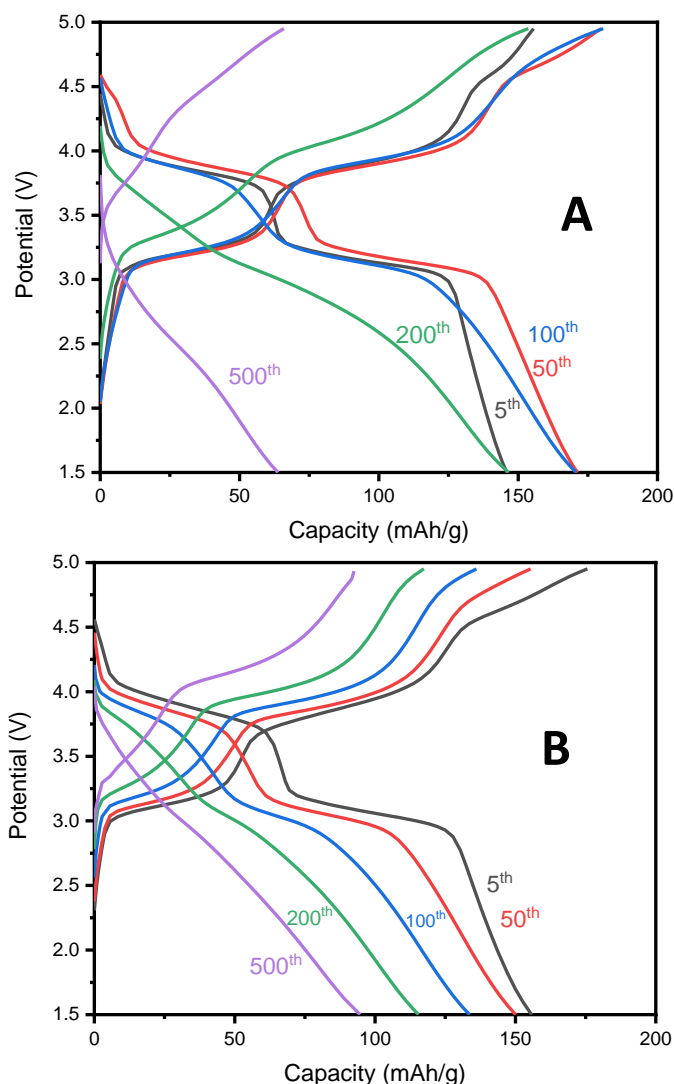


Figure 11. Charge discharge curves for the cells with (a) EC:DEC 1 vol% ADN LiBF<sub>4</sub> and (b) EC:DEC 1 vol% ADN LiPF<sub>6</sub> from 1.5 to 4.95 V

The charge discharge curves for these solvents are shown in Figure 11. The LiBF<sub>4</sub> solution increased in capacity at first. This can be explained by the increasing access of the high voltage plateau. This increase in capacity, however, is counteracted by a degradation of the other plateaus in the system. Due to these competing forces the system hits a maximum capacity at 100 cycles and then starts to decrease as the degradation of the battery increases. This increase in capacity was not seen in the LiPF<sub>6</sub> system. The LiPF<sub>6</sub> system seems to have accessed little to none of the third electron since the third plateau is nonexistent in the charge discharge

curve. Both the LiBF<sub>4</sub> systems and LiPF<sub>6</sub> systems still saw significant degradation of plateaus.

It is unclear what the cause of the degradation is as the solvent decomposition was very low for both the LiBF<sub>4</sub> and LiPF<sub>6</sub> solvents. This is shown in Figure 12 where blank cells were made with EC:DEC 1 vol% ADN in either LiPF<sub>6</sub> or LiBF<sub>4</sub> with the carbon coated aluminum as the current collector. The solvent decomposition was minimal. The LiBF<sub>4</sub> solvent system showed a maximum degradation of .025 mA which is insignificant when compared to the milliamps of current passed in a cell with active material. Since this low decomposition of solvent had little effect on improving the performance of the battery there is something else causing this degradation in performance.

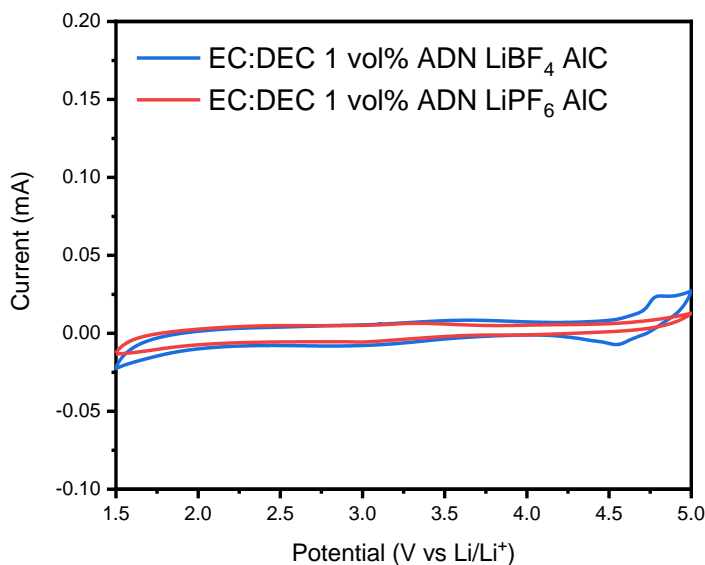


Figure 12. Cyclic Voltammetry of the EC:DEC 1 vol% ADN LiBF<sub>4</sub>/LiPF<sub>6</sub> systems with carbon coated aluminum collectors

The capacity of these cells was also lower than many of the other systems previously investigated as seen in Figure 13. There are several factors for this. First, the carbon coated aluminum has less carbon so there is less capacity contribution from that. There is also less capacity from decomposition as the solvent will contribute

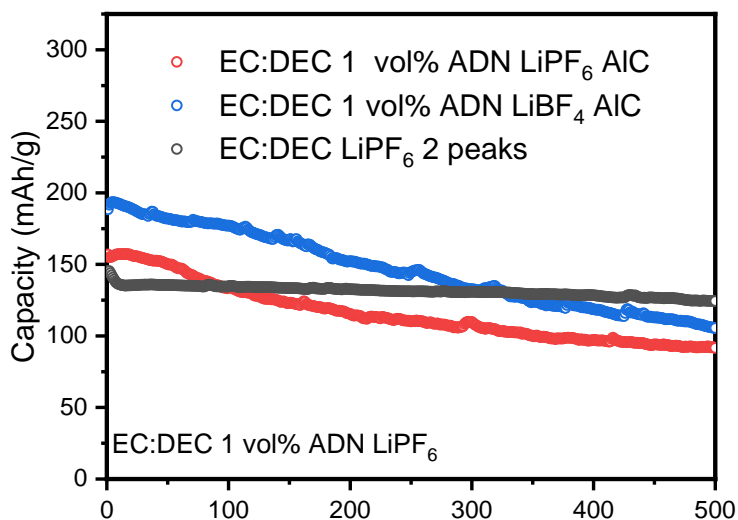


Figure 13. Capacities of the Poly(TAA-PZ) batteries with carbon coated aluminum current collectors over 500 cycles at a constant current of 1 A/g

very little in these systems. This lack of decomposition does help to stabilize the battery some. There is still a large drop in capacity but in comparison to the other solvents this drop is much less than the solvents on the other current collector.

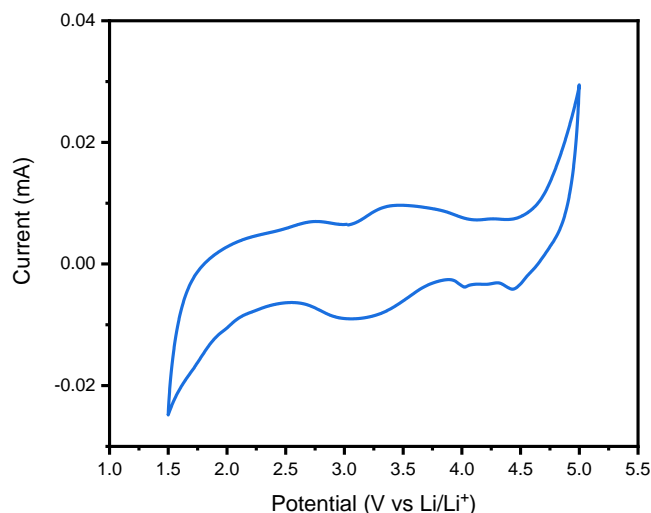


Figure 14. Cyclic Voltammetry of EC:DEC 1 vol% TMS on AIC. Cycled from 1.5 V to 5 V at 5 mV/s

Due to the low performance of the batteries with the ADN, another additive was investigated. Sulfolane (TMS) was the next additive as it has also shown high stability. The largest issue with using TMS is the high viscosity. In order to counteract this the TMS was also used at only 1 vol%, similar to the ADN, to keep the viscosity low. The solvent system tested was EC:DEC 1 vol% TMS in LiPF<sub>6</sub> on a carbon coated aluminum current collector since that had shown the most success with the ADN additive. The blank cell that was made showed very little decomposition, as seen in Figure 14. The maximum decomposition was only 30  $\mu$ A.

This new electrolyte showed much higher stability. Over 100 cycles the battery lost only 13% of its initial capacity. It also showed high capacities compared to the baseline capacity from 2 electrons on the carbon coated aluminum current collector and reached values over 40 mAh/g larger than the 2 electron values as shown in Figure 15. The coulombic efficient of the

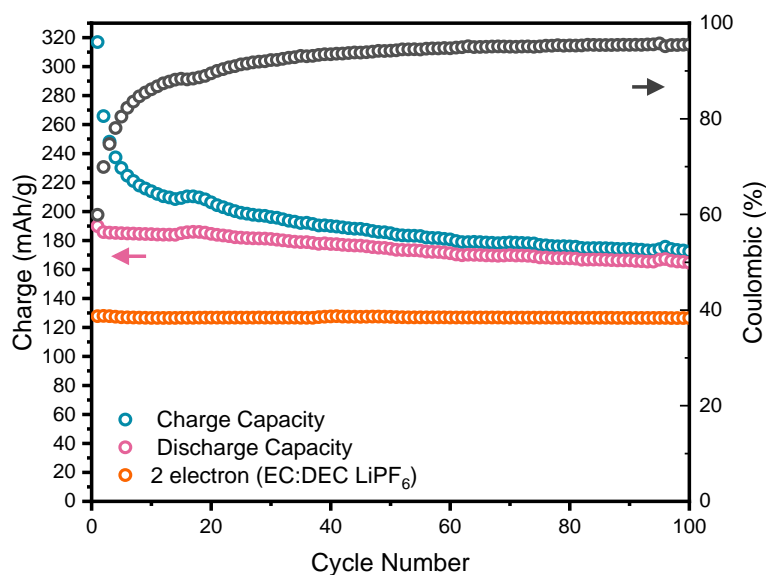


Figure 15. Capacity and Coulombic Efficiency of the EC:DEC 1 vol% TMS LiPF<sub>6</sub> on carbon coated aluminum current collector

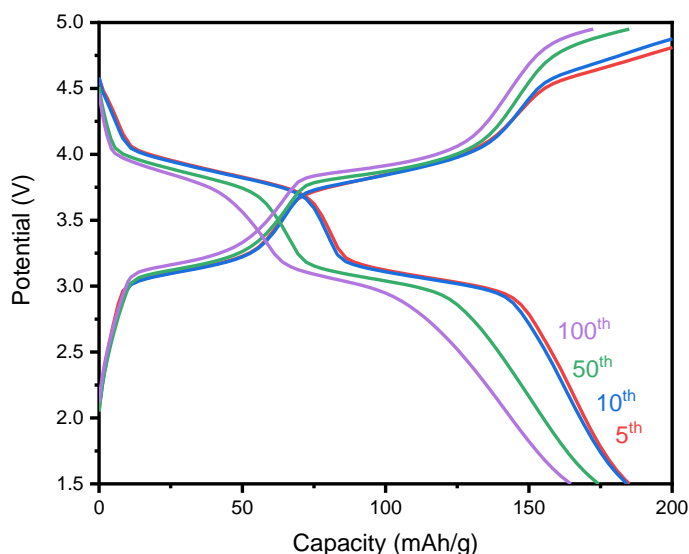


Figure 16. Charge/discharge curves for the EC:DEC 1 vol% TMS solvent on AlC

system is quite low having only reached 96% by the 100<sup>th</sup> cycle. This low coulombic efficiency implies that something irreversible is happening in the cell. The capacity curves in Figure 16 show that some of the higher voltage plateau was accessed. This is more apparent on the charging curves than upon discharging which could explain the low coulombic efficiencies. The charge/discharge curves also show a much slower degradation of plateaus than other solvent systems as the plateaus were still clearly visible at 100 cycles.

While investigating solvent systems a peculiar behavior was found at high voltages, particularly in LiBF<sub>4</sub>. The highest voltage plateau in the solvents that used LiBF<sub>4</sub> as their salt was extremely stable even as the rest of the cell degraded. Initially, believed to have been the third electron being accessed in Poly(TAA-PZ) it seems that this plateau is evidence of something else. In Figure 9 the blank cells of the LiBF<sub>4</sub> solvent systems on carbon paper current collectors are shown. Despite having no active material the blank cells showed a peak that looks reversible. This peak can be compared to the peak seen in an

active cell as shown in Figure 17. This comparison shows that the peak believed to be the third electron was coming from the salt. It is unclear what the cause of this reversible behavior is, but it is most noticeable on carbon paper and in LiBF<sub>4</sub> salt. This behavior can be seen with LiPF<sub>6</sub> salts but is not as prominent.

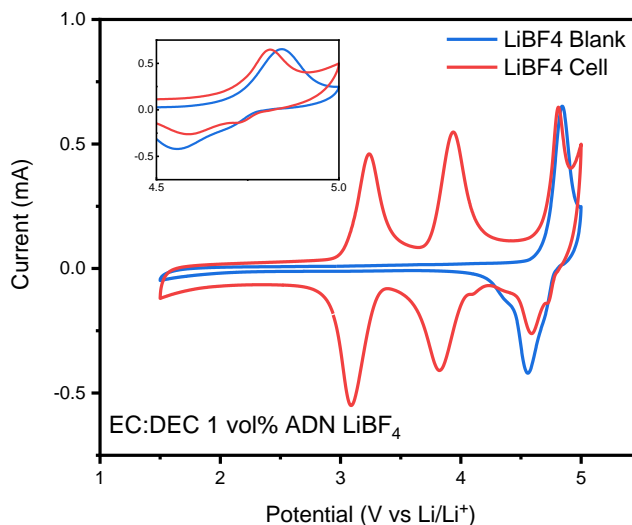


Figure 17. Cyclic voltammetry of both a blank and active cell in EC:DEC 1 vol% ADN LiBF<sub>4</sub> on carbon paper current collectors scanned at 5 mV/s.

## Conclusions

Adiponitrile was initially investigated on a carbon paper current collector. It was found that a lower volume percent of ADN provided better performance due to the lower viscosity of solution. The addition of ADN to these solvents on the carbon paper current collector did successfully lower the decomposition to only .2 mA in the best cases (EC:DEC 1 vol% ADN LiPF<sub>6</sub>, EC:ADN LiBF<sub>4</sub>). This lower solvent decomposition wasn't enough to stabilize the battery system to maintain capacity over 500 cycles with many cells showing significant losses in capacity.

This solvent decomposition and battery performance was improved over the carbon paper

current collectors by switching to a carbon coated aluminum current collector. This lowered the decomposition to 25  $\mu$ A. The cycling performance of the batteries was slightly improved, but still showed high losses over time.

The highest performing battery system that was tested was with TMS as an additive. The EC:DEC 1 vol% TMS LiPF<sub>6</sub> solvent on carbon coated aluminum showed very little decomposition and high stability over 100 cycles. It did have a low coulombic efficiency, implying some decomposition of the system as whole.

Finally, a peculiar behavior with the salts was identified. Future work will need to be done to identify the cause. It has been determined that it is an interaction of the salt with the carbon paper and is reversible.

## References

1. B. Peterson, C. Gannett, L. Shen, J. Seok, B. Fors, and H. Abruna, "High Voltage Cross-linked Phenazine Networks as High Power Density Battery Materials," Manuscript submitted for publicationM. Hu, X. Pang, and Z. Zhou, "Recent progress in high-voltage lithium ion batteries," *Journal of Power Sources*, vol. 237, pp. 229–242, 2013.
2. M. Ue, "Electrochemical Properties of Organic Liquid Electrolytes Based on Quaternary Onium Salts for Electrical Double-Layer Capacitors," *Journal of The Electrochemical Society*, vol. 141, no. 11, p. 2989, 1994.
3. X. Wang, W. Xue, Z. Xu, Y. Li, Y. Li, and R. Huang, "The Study of How the Amount of Adiponitrile Impacts on the Performance of LiNi<sub>0.5</sub>Mn<sub>1.5</sub>O<sub>4</sub> Battery," *Journal of The Electrochemical Society*, vol. 166, no. 4, 2019.
4. Y. Abu-Lebdeh and I. Davidson, "High-Voltage Electrolytes Based on Adiponitrile for Li-Ion Batteries," *Journal of The Electrochemical Society*, vol. 156, no. 1, 2009.
5. 'C-X. Wang, W. Xue, K. Hu, Y. Li, Y. Li, and R. Huang, "Adiponitrile as Lithium-Ion Battery Electrolyte Additive: A Positive and Peculiar Effect on High-Voltage Systems," *ACS Applied Energy Materials*, 2018.



# Potential of the Petite: Electrochromism of CuFeS<sub>2</sub>

Myung Joo Lee<sup>1, 2</sup>, Yuan Yao<sup>2, 3</sup>, Richard Robinson<sup>2, 3</sup>

<sup>1</sup>*Department of Chemistry, Brown University, Providence, RI 02912*

<sup>2</sup>*Cornell Center for Materials Research, Cornell University, Ithaca, NY 14850*

<sup>3</sup>*Nanoscale Materials for Energy Lab, Cornell University, Ithaca, NY 14850*

---

## Abstract

Research regarding plasmonic nanoparticles has focused on noble metal nanoparticles such as gold or silver. There has recently been a push to find dielectric materials such as semiconductors that can emulate the plasmonic behavior exhibited in noble metal nanoparticles. In this paper we explore copper iron sulfide (CuFeS<sub>2</sub>), a dielectric material that shows promise for this role. We show the effect that different sized cations play in electrochromic cells built with dip-coated thin films of CuFeS<sub>2</sub> by showing ultraviolet-visible spectroscopy scans collected in-situ and propose the physical mechanism for electrochromism in thin films.

---

## Introduction

Plasmonic nanoparticles are rising as a potential answer to many of the modern world's challenges. They are extremely versatile due to their local environmental sensitivity and have a great number of applications, such as in biomedical devices involving cancer treatment and in electrical devices such as smart windows. Their use in smart windows would mitigate the energy crisis that the US faces; according to the Department of Energy, about 30% of energy in buildings is lost as heat due to windows (Risser). If smart glass was used instead, the Department of Energy hypothesizes that about \$10 billion could be saved per year.

Not all nanoparticles are plasmonic; what makes certain nanoparticles plasmonic is the ability to induce within them oscillations of free charge carriers, relating to the phenomenon called surface plasmon resonance (SPR). In nanoparticles, this phenomenon is called localized surface plasmon resonance (LSPR), which only occurs in particles significantly smaller than the wavelength of the light hitting it. When this wavelength of light hits these particles, the free carriers in the particles are able to oscillate in phase with the external electric field, which allows for the rise of its unique optical properties (Comin & Manna, 2014).

Although noble metal nanoparticles exhibit LSPR in a range beneficial for our uses, their high optical losses (due to their electronic transitions) make them unideal plasmonic materials. Other materials have therefore emerged as candidates for plasmonic materials. Semiconductors, for example, are rather promising, as varying the free charge carrier concentrations allows for us to tune the SPR frequency to various frequencies in the visible and infrared range (Routzahn, White, Fong, & Jain,

2012). They are also significantly cheaper than noble metals, which makes them much more economically viable for applications on the larger scale such as smart glass. One drawback to using semiconductors is that most of them do not exhibit plasmonic behavior in the visible range of light.

It is important to note that dielectric material nanoparticles, including semiconductors, exhibit plasmonic behavior via a different mechanism than that found in noble metals. Noble metal nanoparticles rely on LSPR, but dielectric nanoparticles simply emulate this behavior when they meet the Fröhlich condition, which describes the free carrier states in which negative real permittivities can occur. Our focus lay on copper iron sulfide (CuFeS<sub>2</sub>), a semiconductor most commonly found in nature as the mineral chalcopyrite. This material offers the best of both the noble metal nanoparticles and the semiconductor nanoparticles: it reacts to light in the visible range, as it meets the Fröhlich condition at these wavelengths, and it is also cheap and tunable (Gaspari et al., 2017).

Here, we are particularly interested in the way thin films of CuFeS<sub>2</sub> nanoparticles coated on indium tin oxide (ITO) glass react to different conditions in electrochromic cells. We synthesize monodisperse nanoparticles of CuFeS<sub>2</sub>, then we dip-coat a thin film onto ITO glass. We then vary the electrolyte used in the cell, using different sized cations to observe the effect of size of the ions on the magnitude of change of plasmon exhibition of the nanoparticles. We particularly focused on three electrolytes of different cation sizes: sodium hexafluorophosphate, potassium hexafluorophosphate, and tetrabutylammonium.

## Experimental Section

### *Materials*

Copper (II) chloride, iron (III) chloride, penicillamine, 1-octadecene, L-ascorbic acid, oleylamine, tetrachloroethylene (TCE), methanol, Nafion solution (5% weight in aliphatic alcohols, decanedithiol, sodium hexafluorophosphate, potassium hexafluorophosphate, tetrabutylammonium hexafluorophosphate, anhydrous acetonitrile, indium tin oxide-coated glass.

### *Synthesis of CuFeS<sub>2</sub> particles*

CuFeS<sub>2</sub> particles were synthesized by first mixing CuCl<sub>2</sub> (33.5 mg), FeCl<sub>3</sub> (40.5 mg), penicillamine (75-100 mg), L-ascorbic acid (500 mg), and 1-octadecene (5 mL) in a 25 mL round-bottomed flask. This mixture was stirred and evacuated first at room temperature, then at 80°C. Once the mixture cooled to room temperature, the flask was filled with nitrogen, and oleylamine (5 mL) was added to the mixture and left to stir for 5 minutes at room temperature. Then the solution was raised to 150°C and left for a period of 2 hours. The resulting dark purple solution was washed with a hexane/acetone mixture and centrifuged at 4400 rpm for 4 minutes to collect the particles at the bottom.

### *Making of thin film*

Indium tin oxide-coated glass slides were first adhered to an insulated wire via a resin that was cured in an oven. Three solutions were prepared for the making of the thin film: 100 µL of decanedithiol was dissolved in 10 mL of TCE; 250 µL of Nafion solution were dissolved in 10 mL of methanol; approximately 30 mg of CuFeS<sub>2</sub> synthesized were dissolved in 2 mL of TCE. About 2 mL of each solution were placed into three separate small sample vials. The glass slide was then dipped into the Nafion solution first for thirty seconds and allowed to dry. This was followed by about eight dipping cycles, where each cycle consisted of dipping into the particle solution, then the decanedithiol solution, then the Nafion solution, each dipped for thirty seconds and letting dry for thirty seconds. After these cycles, the glass was dipped into the particle solution once more, and then directly into the Nafion solution.

### *Building the electrochromic cell*

The electrochromic cell was built inside a nitrogen-filled glove box. 0.1M electrolyte solutions of sodium hexafluorophosphate, potassium hexafluorophosphate, and tetrabutylammonium phosphate in acetonitrile were made inside of this nitrogen environment. The dip-coated glass was inserted into a rubber stopper apparatus which also held a platinum counter electrode and a silver reference electrode. This rubber stopper was screwed into the top of the cuvette, aligning the glass with a clear side of the cuvette. Approximately 2.5 mL of electrolyte solution were injected into the cell to cover the dip-coated layer of CuFeS<sub>2</sub> and the two wires.

### *Constant voltage in-situ experiment*

A VMP3 Bio-Logic Science Instruments potentiostat was used for electric control, and EC Labs used as the software to accompany it. The software OceanView was used to control the DH-2000-BAL Ocean Optics light source, which was used with both the halogen and the deuterium lamps on. The UV-vis and the potentiostat were used in tandem for an in-situ experiment. The respective wires from the VMP3 were connected to each of the electrodes, and the cell placed inside of the cuvette holder. A constant voltage stepwise discharge and recharge procedure was created. the cell was reduced to -1.5V, starting at -0.3V and going down at 0.3V increments, holding at each voltage for 5 minutes. The cell was then oxidized to 0.3V, starting at -1.5 and going up by 0.3V increments. All UV-vis scans were collected during this time.

### *Cyclic voltammetry*

EC Labs was again used with the VMP3 Bio-Logic Science Instruments potentiostat. The cell was again discharged to -1.5V and recharged to 0.3V at a rate of 10 mV/second.

## Results and Discussion

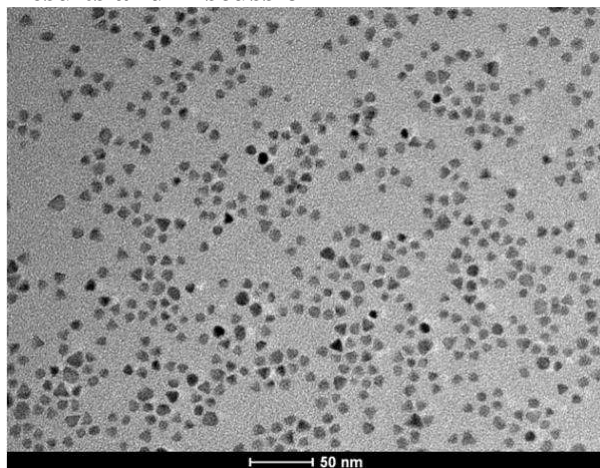


**Figure 1.** TEM image of  $\text{CuFeS}_2$  nanoparticles. Particles were 7.9 nm in diameter with 11% dispersity. Image taken by Frank Yao.

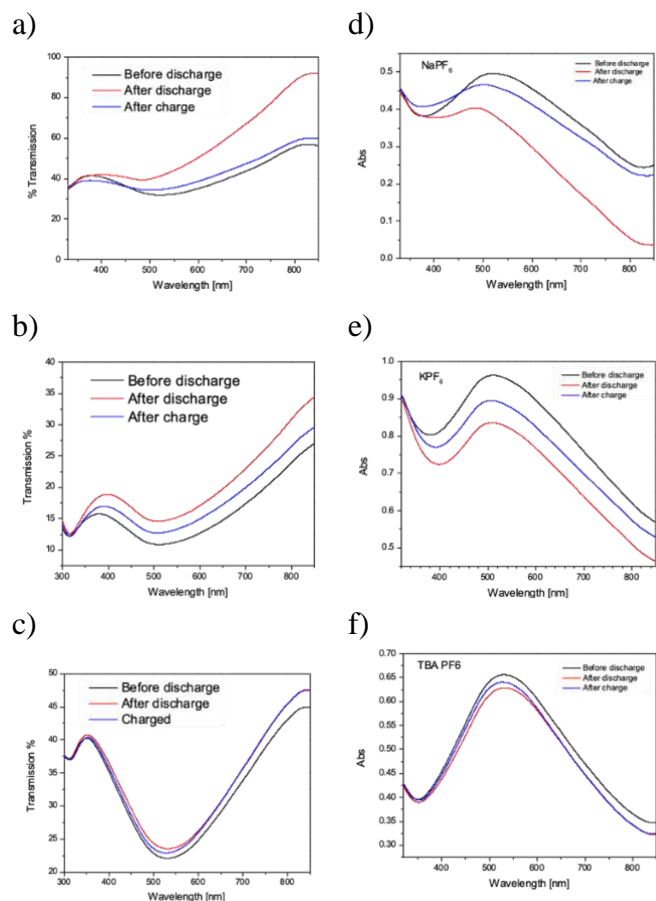


**Figure 2.** UV-Vis scans of spectra at start, after reduction to -1.5V, and after recharge to 0.3V. Figures 2a, b, c represent the transmission spectra for the electrolytes  $\text{NaPF}_6$ ,  $\text{KPF}_6$ , and  $\text{TBAPF}_6$ , respectively. Figures 2d, e, f represent the absorbance spectra for the electrolytes  $\text{NaPF}_6$ ,  $\text{KPF}_6$ , and  $\text{TBAPF}_6$ , respectively.

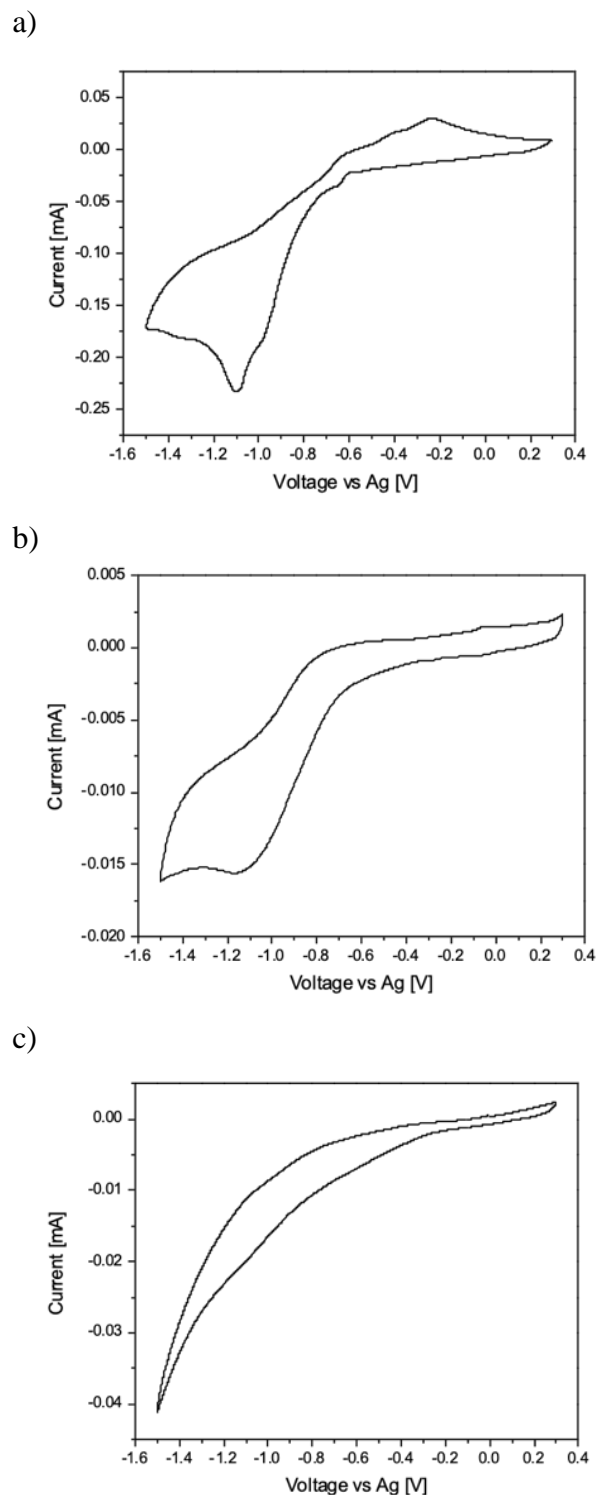


**Figure 3.** Cyclic voltammetry graphs of the electrochromic cells featuring different electrolytes. For Figure 3a, b, c, the electrolytes in the cell were  $\text{NaPF}_6$ ,  $\text{KPF}_6$ , and  $\text{TBAPF}_6$ , respectively.

The UV-Vis absorbance data (Figure 2) reveals that during discharge, the plasmon peak (located at around 525nm) diminishes, and then increases again during recharge. However, this effect is much more significant for the smaller cations. The transmission data (Figure 2a, 2b, 2c) indicates that for the TBA<sup>+</sup>, there was at most a 10% change in transmission at 525 nm during discharge, and an even smaller change during recharge; for K<sup>+</sup>, there was a significantly greater change of about nearly 100% after discharge, and a 50% overall change after recharge; in the case of Na<sup>+</sup>, there was over 100% change after discharge, and a 50% overall change after recharge. For both potassium and sodium, there were great changes in transmission at the location of the plasmon, but there were very small changes for TBA.

The CV data (Figure 3) also indicates this pattern. Figure 3c is a smooth CV and does not show any peaks, indicating a lack of reduction-oxidation occurring in the cell, while Figure 3a shows peaks at about -1.1V and at -0.2V and Figure 3b shows a peak at about -1.1V, indicative of reduction-oxidation activity.

This redox activity appears to be directly related to the amount of change in transmissions as well as the ionic radius of the cation in solution. The transmission plot for sodium indicated the greatest amount of change, the CV plot indicated the greatest amount of redox activity, and sodium, at 116 pm in radius, is the smallest cation used in this experiment. Meanwhile, the transmission plot for TBA showed little change, the CV plot indicated no redox activity, and with an ionic radius of 494 pm, TBA is the largest cation used in this experiment. Potassium, whose ionic radius falls in between sodium and TBA at 152 pm but is closer to that of sodium, shows behavior much more similar to sodium but not nearly as drastic in terms of change in transmission and the CV plot.

This suggests a mechanism for electrochromism and emphasizes the importance of the electrolyte used in electrochromic cells using a thin film coating method. First, these results suggest that the mechanism by which plasmon activity is diminished is by cations intercalating the spaces between nanoparticles. Since the method by which the layers of nanoparticles are built up require layers of other substances in between, the size of the cation determines whether or not it is able to transfer electrons to and from these particles. Sodium, being so small, is able to fit in these

spaces, and is able to effectively transfer electrons to and from these particles, while TBA is too large to be effective.

## Conclusion

In the context of using a thin film, we were able to determine that the ionic radius of the cation in solution determines the magnitude of reduction-oxidation activity that occurs with the CuFeS<sub>2</sub> particles. Future work regarding this project includes gathering more evidence for the mechanism of the electrochromism of CuFeS<sub>2</sub> nanoparticles.

## Acknowledgements

I would like to thank Professor Richard Robinson for the opportunity to work in his lab. I would like to express my deepest gratitude to my wonderful mentor, Frank Yao, who taught me everything about this lab, and Ariadna Lubinus. Thanks also Cornell Center for Materials Research REU program for making this experience possible.

## Funding

This project was funded by the NSF under the award number E74-8519.

## References

- Comin, A., & Manna, L. (2014). *Chem Soc Rev* *New materials for tunable plasmonic colloidal nanocrystals*. 3957–3975.  
<https://doi.org/10.1039/c3cs60265f>
- Gaspari, R., Valle, G. Della, Ghosh, S., Kriegel, I., Scotognella, F., Cavalli, A., & Manna, L. (2017). Quasi-Static Resonances in the Visible Spectrum from All-Dielectric Intermediate Band Semiconductor Nanocrystals [Rapid-communication]. *Nano Letters*, 17, 7691–7695.  
<https://doi.org/10.1021/acs.nanolett.7b03787>
- Risser, R. (2011, April 5). Making Smart Windows Smarter. Retrieved from <https://www.energy.gov/articles/making-smart-windows-smarter>
- Routzahn, A. L., White, S. L., Fong, L., & Jain, P. K. (2012). *Plasmonics with Doped Quantum Dots*. 52(11–12), 983–991.  
<https://doi.org/10.1002/ijch.201200069>
- van der Stam, W., Gudjonsdottir, S., Evers, W. H., & Houtepen, A. J. (2017). *jacs.7b07788.pdf*. *Journal of the American Chemical Society*, 139, 13208–13217.  
<https://doi.org/10.1021/jacs.7b07788>

# Functionalized Polyurethane Coating for Food Industry Applications

Gabriel Martinez-Zayas, Autumn Rudlong, Julie Goddard

**ABSTRACT:** Within food processing facilities there are safety concerns regarding bacterial growth, specifically floor drains. These areas are not routinely cleaned and can be harboring sites for biofilms to develop and become resistant to sanitizing treatments. Therefore, the objective of this research is to create a commercially translatable antimicrobial and non-fouling polyurethane coating to reduce contamination and persistence of bacteria within food processing plants. This work shows that control polyurethane and 1% perfluoropolyether (PFPE) polyurethane were synthesized and preliminarily characterized. Current water contact angle measurements of 1% PFPE polyurethane demonstrates that using fluorinated compounds makes the polymer more hydrophobic, which is essential for a polymer coating that will reduce biofilm development and persistence.

## Introduction

Food manufacturers typically manage facilities by zoning.<sup>9</sup> *Zone 1* is composed of surfaces that are in direct contact with food materials, such as flumes and conveyer belts, and *Zone 2* typically include equipment used for food processing, excluding surfaces that directly contact the unpackaged foods. *Zone 3* refers to surface areas in the processing facility excluding *Zones 1 and 2*, such as floors, drainage, walls, etc. *Zone 3*, while not in direct contact with food materials, are diverse niches and can harbor microbial communities that potentially interact with *Zones 1 and 2*.<sup>10</sup> Furthermore, if *Zone 3* surfaces are not properly cleaned, they can develop biofilms. If this is left unnoticed, food can come in contact with these bacteria, potentially including spoilage organisms that may cause undesirable changes to the quality of food or pathogens which are harmful to consume.<sup>10</sup> Therefore, food processing plants are greatly concerned with preventive and control strategies that can inhibit biofilm formation and also decrease the probability of contaminating food.

Many researchers have investigated the prospect of utilizing functionalized polymers as antimicrobials and biofilm inhibitors.<sup>1,2,7</sup> However, to our knowledge, none have focused their efforts on areas within food processing plants that do not come in contact with food products. This is why this research proposes a commercially translatable antimicrobial and non-fouling polyurethane to coat onto drains and pipes in order to kill bacteria and prevent biofilms to develop.

Polyurethane (PU) is a cheap, easily synthesized polymer with high durability, simple application and a low maintenance lifespan. Most importantly, it is a well-established material that has already been adopted by industry.<sup>12</sup> Quaternary ammonium salts (QAS) are antimicrobial compounds that are commonly used as

active ingredients in industrial disinfectants.<sup>8</sup> Fluorinated compounds, such as Teflon, are materials that are superhydrophobic, which can be utilized in as a non-fouling agent to prevent biofilms from developing. Non-fouling surfaces refer to surfaces which resist the adsorption of proteins and/or adhesion of cells.<sup>11</sup> Therefore, we propose a one batch synthesis in order to produce a PU film that is fully functionalized within the polymer structure, giving it the durability and non-leaching properties that are necessary for food processing plants.

Efforts in our lab have led to the production of control PU films that were preliminarily characterized by FTIR, SEM and Contact Angle, as well as 1% Perfluoropolyether (PFPE) PU films that were preliminarily characterized by FTIR and Contact Angle.

## Experimental Section

### *Synthesis of Control PU and 1% PFPE PU*

Chemical proportions for the reaction of the Control PU were based on the methods by Hepburn<sup>3</sup>. The synthesis was performed using a 5 neck round bottom reaction vessel equipped with silicon oil bath at 80 °C, overhead stirrer, temperature probe (in oil bath), and sparging needle with N<sub>2</sub> hose. For the PU prepolymer reaction 5g of Polypropylene glycol (PPG) was dissolved in 8 mL of Dimethylformamide (DMF) and transferred quantitatively to the reaction vessel. Then 48μl of the catalyst stannous octoate were added followed by the addition of 2.37g of 4,4'-diphenylmethane diisocyanate (MDI). This reaction was left stirring at 500 rpm for 30 min. After this point 0.25 g of ethylene glycol, the chain extender, were dissolved in 6 mL of DMF and added dropwise to the prepolymer mixture using an addition funnel. This was left to stir again at 500 rpm for 2.5 hours. For the synthesis of 1% PFPE PU



the same process was used except that 0.05 g of PFPE was added together with the PPG in the prepolymer reaction.<sup>13</sup>

After the reactions were finished the polymer was coated onto different surfaces including stainless steel sheets, Polypropylene (PPE) sheets and poured in Polytetrafluoroethylene (PTFE) molds. Half were left to cure in ambient conditions and the other half were left to cure inside the Binder VDL 23 Vacuum Drying Oven at 80°C for 24hr.

#### *Characterization by Fourier Transform Infrared Spectroscopy (FTIR)*

Chemical properties of commercial, control and modified PU films were analyzed with an IR Tracer-100 spectrometer (Shimadzu Corp., Tokyo, Japan) equipped with a diamond Attenuated Total Reflectance (ATR) crystal. For each set of prepared films, a random spot was measured for their absorbance in each sample film for at least 3 randomly selected films. FTIR analysis was conducted using Happ-Genzel apodization at a resolution of 4 cm<sup>-1</sup> and with a total of 32 scans applied for each measurement. The obtained spectra then underwent base-line correction and smoothing and were analyzed with OriginLab software.<sup>1</sup>

#### *Characterization by Scanning Electron Microscopy (SEM)*

To understand the surface morphology, control samples were characterized using SEM. Before analyzing the control PU, samples were first gold coated with Ted Pella Cressington Sputter Coater in order to make them suitable for SEM analysis.

#### *Characterization by Contact Angle*

Hydrophobicity of the control PU and 1% PFPE PU films was evaluated using advancing and receding water contact angles measured with Biolin Scientific Attension Theta Optical Tensiometer. To record the advancing contact angle a drop of 2.5 µL HPLC grade water was dispensed onto the sample films at a rate of 0.5 µL/sec and then enlarged using the same rate until the drop became 5 µL. Using the same 5 µL drop, receding contact angles were measured by gathering the drop at a rate of 0.5 µL/sec. Measurements and images were obtained through the instrument's OneAttension software.

## **Results and Discussion**

### *FTIR analysis of Polyurethane Films*

FTIR spectroscopy was used to characterize the surface chemistry of commercial, control and 1% PFPE PU as shown in **Fig. 1**. All types of PU demonstrated absorbance bands (2980-2820 cm<sup>-1</sup> and ~1400 cm<sup>-1</sup>) which are all characteristic of alkane groups from the polyurethane carbon backbone (C-H bond). They also exhibited medium broad bands (330-3310 cm<sup>-1</sup>) attributed to the N-H bond from amines present in the polyurethane. A more prominent band from 1700-1730 cm<sup>-1</sup> was deconvoluted from the spectra of the control and 1% PFPE PU using OriginLab's Peak Deconvolution software and it resulted in two peaks: 1700 cm<sup>-1</sup>, corresponding to the hydrogen bonded urethane carbonyl groups and 1727-1739 cm<sup>-1</sup> corresponding to incompletely hydrogen bonded urethane carbonyl stretching vibration. Commercial PU exhibited similar bands from 1700-1730 cm<sup>-1</sup>.

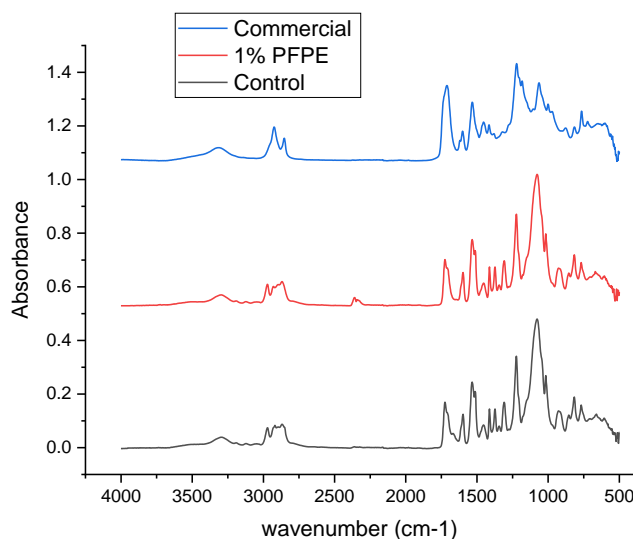


**Figure 1.** FTIR Spectra from top to bottom: Commercial PU, 1% PFPE PU, and Control PU.

Furthermore, all PU's exhibited bands around 1500 cm<sup>-1</sup>, corresponding also to amides. There were also bands in all PU's in the 1600 cm<sup>-1</sup> associated to (C=C bonds) from the aromatic rings in the MDI, in the 1220 cm<sup>-1</sup> corresponding to (C-O bonds) and there was no band for isocyanate band in 2260 cm<sup>-1</sup> indicating that all was consumed during the reactions. Using FTIR there were no distinction between the spectra of Control PU and 1% PFPE PU so for future experiments using a higher percent of PFPE may result in bands more indicative of the presence of fluorinated compounds.

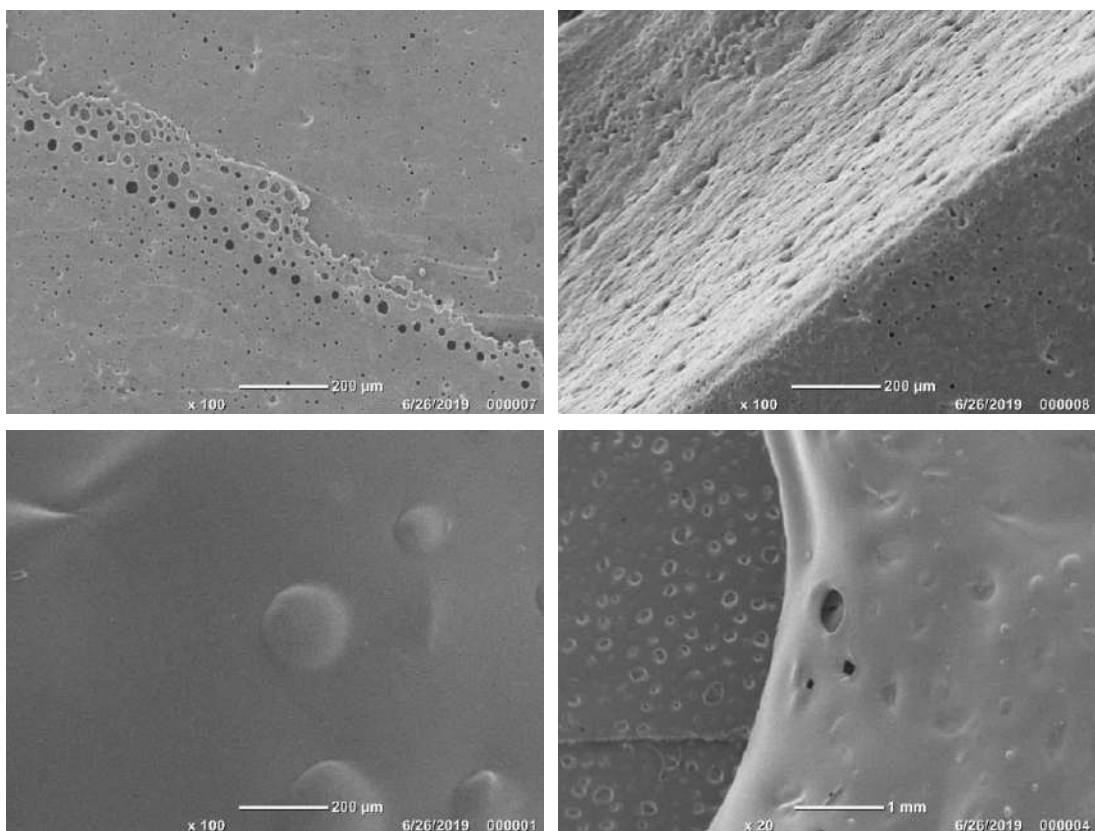


**Figure 2.** SEM Images: Top) Ambient Cured Control PU, Bottom) Oven Cured Control PU

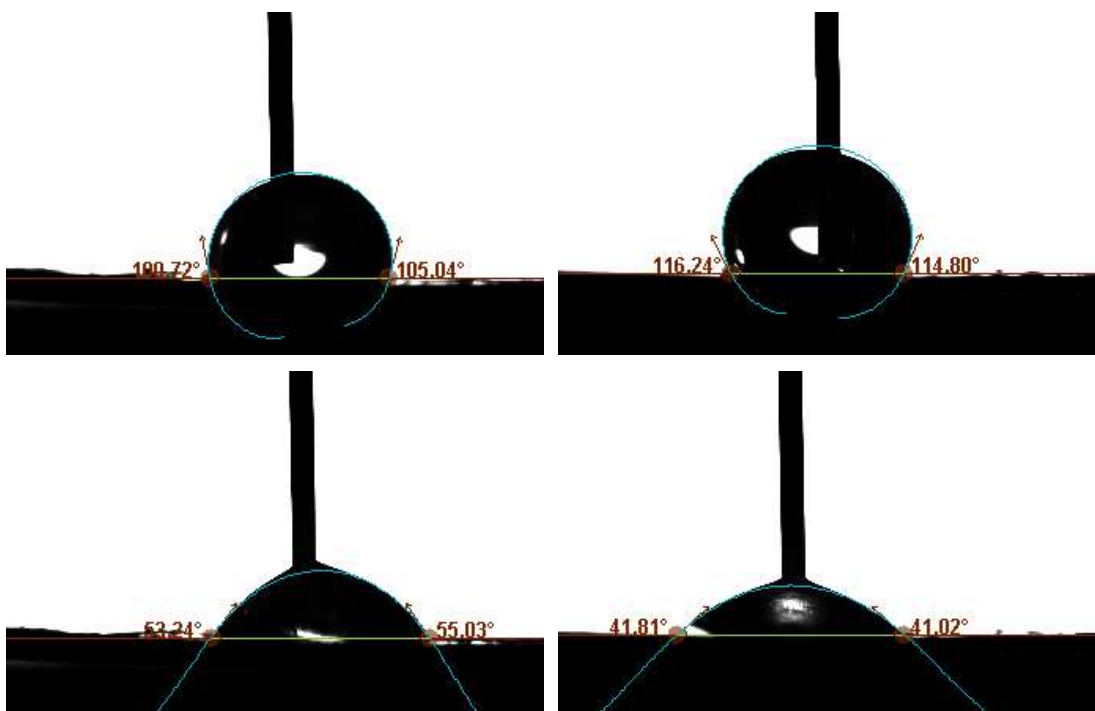


**Figure 3.** Contact Angles: Top Left) Advancing CA of Control PU, Top Right) Advancing CA of 1% PFPE PU  
Bottom Left) Receding CA of Control PU, Bottom Right) Receding CA of 1% PFPE PU

### SEM analysis of Control Polyurethane Films

To understand the surface morphology, control samples were characterized using SEM as shown in **Fig. 2**. The purpose for this analysis was to compare ambient cured and oven cured polyurethane. As shown in the SEM images the surface of ambient cured samples had an abundance of micropores and oven cured samples had bubbles and pores throughout its surfaces. These findings are not ideal because micropores can potentially harbor bacteria and permit biofilms to develop but can be easily removed by flaming or vacuum degassing the polyurethane before curing.<sup>3</sup>

### Water Contact Angles of PU films

Preliminary hydrophobicity of the control PU and 1% PFPE PU films were evaluated using advancing and receding water contact angles (CA) as shown in **Fig. 3**. Advancing CA resulted in 102.88° and 115.52° for Control PU and 1% PFPE PU, respectively, and receding CA resulted in 54.14° and 41.42° for Control PU and 1% PFPE PU, respectively. A larger advancing CA and smaller receding CA signify that a surface is more hydrophobic. This initial CA study indicates that functionalizing PU with fluorinated compounds, such as PFPE, makes the polymer more hydrophobic.

### Conclusions

In this work, we successfully synthesized and preliminarily characterized Control PU and 1% PFPE PU. Current contact angle measurements of 1% PFPE PU demonstrates that using fluorinated compounds in our polymer coating makes it more hydrophobicity, but future experiments are needed to confirm that using fluorinated compounds will make the polyurethane non-fouling.

### Acknowledgements

I would like to thank Professor Julie Goddard for offering me the opportunity to work in her lab for the summer, as well as Autumn Rudlong for her guidance. Additional thanks to all Goddard Group members for welcoming me to the lab and a special thanks to the CCMR REU program for making this summer a great learning experience.

### Funding

This work was supported by the United States Department of Agriculture National Institute of Food and Agriculture under grant #2018-67017-27874; and Hatch project #1016621.

### References

1. Hung, Y.-T.; Mcclandsborough, L. A.; Goddard, J. M.; Bastarrachea, L. J. Antimicrobial Polymer Coatings with Efficacy against Pathogenic and Spoilage Microorganisms. *Lwt* **2018**, 97, 546–554.
2. Wynne, J. H.; Fulmer, P. A.; Mccluskey, D. M.; Mackey, N. M.; Buchanan, J. P. Synthesis and Development of a Multifunctional Self-Decontaminating Polyurethane Coating. *ACS Applied Materials & Interfaces* **2011**, 3(6), 2005–2011.
3. Hepburn, C. *Polyurethane elastomers*, 2nd ed.; Elsevier applied Science: London, 1992. 46-48
4. Zhao, P.; Wang, Y.; Zhu, J.; Hua, X.; Wen, Q. Characterization of Graded Polyurethane Elastomer by FTIR. *Science in China Series B: Chemistry* **2008**, 51(1), 58–61.
5. Bandekar, J.; Okuzumi, Y. FT-IR Spectroscopic Studies of Polyurethanes. *Journal of Molecular Structure: THEOCHEM* **1993**, 281(2-3), 113–122.
6. Wang, S.-K.; Sung, C. S. P. Fluorescence and IR Characterization of Cure in Polyurea, Polyurethane, and Polyurethane–Urea. *Macromolecules* **2002**, 35(3), 883–888.
7. Barish, J. A.; Goddard, J. M. Anti-Fouling Surface Modified Stainless Steel for Food Processing. *Food and Bioproducts Processing* **2013**, 91(4), 352–361.
8. Gerba, C. P. Quaternary Ammonium Biocides: Efficacy in Application. *Applied and Environmental Microbiology* **2014**, 81(2), 464–469.
9. Simmons, C. K.; Wiedmann, M. Identification and Classification of Sampling Sites for Pathogen Environmental Monitoring Programs for *Listeria Monocytogenes* : Results from an Expert Elicitation. *Food Microbiology* **2018**, 75, 2–17.

10. Gu, G.; Ottesen, A.; Bolten, S.; Wang, L.; Luo, Y.; Rideout, S.; Lyu, S.; Nou, X. Impact of Routine Sanitation on the Microbiomes in a Fresh Produce Processing Facility. *International Journal of Food Microbiology* **2019**, *294*, 31–41.
11. Hoffman, A. S. Non-Fouling Surface Technologies. *Journal of Biomaterials Science, Polymer Edition* **1999**, *10*(10), 1011–1014.
12. Akindoyo, J. O.; Beg, M. D. H.; Ghazali, S.; Islam, M. R.; Jeyaratnam, N.; Yuvaraj, A. R. Polyurethane Types, Synthesis and Applications – a Review. *RSC Advances* **2016**, *6*(115), 114453–114482.
13. Jiang, J.; Fu, Y.; Zhang, Q.; Zhan, X.; Chen, F. Novel Amphiphilic Poly(Dimethylsiloxane) Based Polyurethane Networks Tethered with Carboxybetaine and Their Combined Antibacterial and Anti-Adhesive Property. *Applied Surface Science* **2017**, *412*, 1–9.

# Finite Element Method Simulations of Superconducting Microstructures

Maya H. Martinez,<sup>1</sup> G. M. Ferguson,<sup>2</sup> and Katja C. Nowack<sup>2</sup>

<sup>1</sup>*Department of Physics, Harvey Mudd College, Claremont, CA 91711*

<sup>2</sup>*Laboratory of Atomic and Solid State Physics, Cornell University, Ithaca, NY 14853*

We present finite element method (FEM) simulations to better understand the relationship between induced strain fields and resultant superconducting spatial modulations in CeIrIn<sub>5</sub> and Sr<sub>2</sub>RuO<sub>4</sub> microstructures. FEM simulations have proven useful to better understand how unique geometries affect induced strain fields generated from the differential thermal contraction between the sample and substrate, consequently changing the superconducting transition temperature across the structure. A deeper understanding of how induced strain fields influence the superconducting transition temperature may allow for more accurately designed and fabricated modulations in superconductivity, with hopes of designing structures with suitable specifications for the production of devices such as SNS Josephson Junctions.

## I. INTRODUCTION

Few methods exist to spatially modulate the electronic properties of solids; however, it has been shown that control over the superconducting order in certain materials may be achieved by introducing non-uniform strain fields in microstructured devices [1]. In materials such as CeIrIn<sub>5</sub> and Sr<sub>2</sub>RuO<sub>4</sub>, whose superconductivity exhibit high strain sensitivity, spatial modulation of superconductivity in single crystal devices is achieved through strain generated by the differential thermal contraction between the sample and the substrate. The ability to modulate these electronic properties could open doors to new designs of corresponding states in research and applications. An area of interest is the possibility of creating SNS Josephson junctions within a single crystal by suppressing superconductivity in selected areas of the device. Finite element method (FEM) simulations can help predict and create custom spatial modulations and be used to understand the resultant superconductivity patterns on these microstructures. Here we present simulation methods and results to better understand the relationship between our experimental methods and the resultant superconducting patterns in CeIrIn<sub>5</sub> and Sr<sub>2</sub>RuO<sub>4</sub> microstructures.

## II. SIMULATING EXPERIMENTAL DATA

### A. Experimental Methods

We observe spatially modulated superconductivity in CeIrIn<sub>5</sub> and Sr<sub>2</sub>RuO<sub>4</sub> rectangular lamellas and microstructures created from a single crystal by a focused ion beam (FIB). For the case of the tailored microstructures, a FIB is again used to create additional geometries on the device, cutting through the crystal and the epoxy layers. In either case, the rectangular lamella is carved from a macroscopic crystal using a FIB and attached to a sapphire substrate with epoxy [1]. The directions of the crystallographic axes can be chosen for each experiment. When the structures are cooled down to cryogenic tem-

peratures the crystal and the substrate thermally contract. In these limits, Sapphire thermally contracts by  $\sim 0.08\%$ , CeIrIn<sub>5</sub> by  $\sim 0.3\%$ , and Sr<sub>2</sub>RuO<sub>4</sub> by  $\sim 0.2\%$ . This mismatch of thermal contraction between substrate and crystal is responsible for the strain fields creating the spatial modulation of superconductivity.

In order to study the superconducting transitions a local magnetic field is applied to the lamella using a superconducting quantum interference device (SQUID). Superconducting regions will exhibit a strong diamagnetic response producing a series of susceptibility images (FIG 2 (A(i)-A(iii)), (D(i)-D(iii))). These series of images illustrate, as a function of temperature, that different areas of the lamella will begin to superconduct until a low enough temperature is reached such that the whole structure is superconducting. It is with finite element method simulations that we try to understand the patterns in these susceptibility images.

### B. Computational Methods and Simulation Parameters

The FEM simulations are created using the Solid Mechanics Module in COMSOL. A 3D model of the microstructure is created and attached to the sapphire substrate with a layer of epoxy. To model the adhesion between the three materials, we assume that the strain field is continuous along the interfaces between the substrate, epoxy and crystal. A mesh is then placed over the surfaces and interfaces of the structure, creating a finite element grid. At each point on the grid the strain is calculated. Both CeIrIn<sub>5</sub> and Sr<sub>2</sub>RuO<sub>4</sub> are tetragonal crystals, and the strain may be broken into the following irreducible expressions:

$$\epsilon_{A_{1g},1} = (\epsilon_a + \epsilon_b)$$

$$\epsilon_{A_{1g},2} = \epsilon_c$$

$$\epsilon_{B_{1g}} = (\epsilon_a - \epsilon_b)$$

$$\epsilon_{B_{2g}} = 2\epsilon_{ab}$$

$$\epsilon_{E_g} = 2\epsilon_{ac}, 2\epsilon_{bc}$$



where  $\epsilon_i$  is the strain along the  $i$  axis, and  $\epsilon_{ij}$  is the shear strain along the  $i$  and  $j$  axes.

From experimental observations [2], [3] it has been deduced that certain strain components to order parameters and change  $T_c$ . For  $\text{CeIrIn}_5$  it has been shown that the relationship between  $T_c$  and uniaxial pressure is linear [2]. This requires that the strains responsible for the change in  $T_c$  are  $\epsilon_{A1g,1}$  and  $\epsilon_{A1g,2}$ . The strains responsible for the change in  $T_c$  in  $\text{Sr}_2\text{RuO}_4$  can be found using the Ginzburg-Landau free energy and from experimental observations [3], [4]. These strains include  $\epsilon_{A1g,1}$ ,  $\epsilon_{A1g,2}$ , and  $\epsilon_{B1g}$ .

Using the simulated strain field we can then compute the local transition temperature for the crystals. Because the transition temperatures of the two materials of interest respond differently to different strains, two unique equations are used to calculate their respective local superconducting transition temperatures. In order to calculate the local superconducting transition temperature for  $\text{CeIrIn}_5$  we use:

$$T_c = T_{c0} + (\epsilon_A + \epsilon_B) \frac{\delta T_c}{\delta \epsilon_a} + \epsilon_c \frac{\delta T_c}{\delta \epsilon_c}$$

Where  $T_{c0}$  is the bulk transition temperature for the crystal:  $T_{c0} = 0.4K$ . And  $\delta T_c / \delta \epsilon_i$  is the change in the critical temperature of the superconductor in response to uniaxial strain along the  $i$  axis. This coupling parameter is found using the measured elastic moduli of the material and the relationship of  $T_c$  as a function of applied uniaxial pressure [2]. We calculate,

$$\frac{\delta T_c}{\delta \epsilon_a} = -57K/[strain], \quad \frac{\delta T_c}{\delta \epsilon_c} = 66K/[strain]$$

For  $\text{Sr}_2\text{RuO}_4$  a similar methodology is used to calculate the order parameters and local superconducting temperature of the crystal. To compute the local superconducting transition temperature for  $\text{Sr}_2\text{RuO}_4$  we use:

$$T_c = T_{c0} + \epsilon_{A1g,1} \frac{\delta T_c}{\delta \epsilon_{A1g,1}} + \epsilon_{A1g,2} \frac{\delta T_c}{\delta \epsilon_{A1g,2}} + \epsilon_{B1g}^2 \frac{\delta^2 T_c}{\delta \epsilon_{B1g}^2}$$

where  $T_{c0} = 1.5K$ . The coupling parameters for  $\text{Sr}_2\text{RuO}_4$  are computed using the elastic moduli for  $\text{Sr}_2\text{RuO}_4$  and equations relating  $T_c$  as a function of hydrostatic pressure, and uniaxial pressure applied in the  $c$ -direction of the crystal. We calculate,

$$\begin{aligned} \frac{\delta T_c}{\delta \epsilon_{A1g,1}} &= 28K/[strain] \\ \frac{\delta T_c}{\delta \epsilon_{A1g,2}} &= 68K/[strain] \\ \frac{\delta^2 T_c}{\delta \epsilon_{B1g}^2} &= 6.5e4K/[strain] \end{aligned}$$

With these equations, order parameters, and simulated strain fields we may generate maps of local  $T_c$  for devices in either crystalline material.

### C. Simulating Small Structures

Using FEM simulations we can create insight to how certain structures will affect the local superconducting transition temperature across the device. Small devices comprised of thin beams aligned in the  $a$ - and  $c$ - directions (as seen in FIG 1) can not be resolved with the SQUID due to their size; however, a  $T_c$  map can be created to better understand the transport characteristics of these devices.

In order to generate meaningful  $T_c$  maps for these small structures a fine mesh for the device must be used to create the finite grid. Within COMSOL custom meshes may be created and overlayed on the 3D model of the device, however due to the size of the total geometry of the microstructures including the substrate the mesh must be compartmentalized so that COMSOL does not run out of memory. New tetrahedral meshes must be created and assigned to specific domains within the 3D model to prevent this from happening. To minimize the amount of memory used, the finest mesh was only applied to the crystal microstructure, meanwhile predefined coarser meshes were assigned to the glue and substrate domains. A well defined mesh created for the crystal is shown in FIG 1(B). Once a fine mesh has been applied to the crystal, a meaningful  $T_c$  map may be generated.

A strong dependence of transport  $T_c$  on crystallographic axes is illustrated in these smaller devices (as seen in FIG 1(D).) From the transport data, we find that the beam aligned in the  $c$ -direction has a higher transition temperature than the bulk  $T_c$  ( $\sim 0.7K$ ), meanwhile the beam aligned in the  $a$ -direction has a much lower transition temperature than bulk  $T_c$  ( $\sim 0.2K$ .) The  $T_c$  maps generated for this device agree with what is seen experimentally via transport. The computed  $T_c$  for either aligned beam is overlayed in the transport data in FIG 1(D) and shows general agreement. This can also be seen in the suppressed  $T_c$  along the  $a$ -aligned beam in the  $T_c$  map in FIG 1(E), and the elevated  $T_c$  along the  $c$ -aligned beams. This agreement is fruitful due to our inability to produce susceptibility images for these small devices, illustrating what superconducting transition modulation may be occurring in microstructures like these.

### D. Simulating Imaged Structures

For larger structures we can use simulations to directly compare with the imaging data of the susceptibility images to better understand how physical properties of the device affect the local superconducting transition temperature across the structure. For both  $\text{CeIrIn}_5$  and  $\text{Sr}_2\text{RuO}_4$  simulations of a rectangular lamella were generated so that they may be compared to existing susceptibility images of similar samples.

First a rectangular lamella of  $\text{CeIrIn}_5$  was simulated. Through multiple iterations of this simulation the phys-

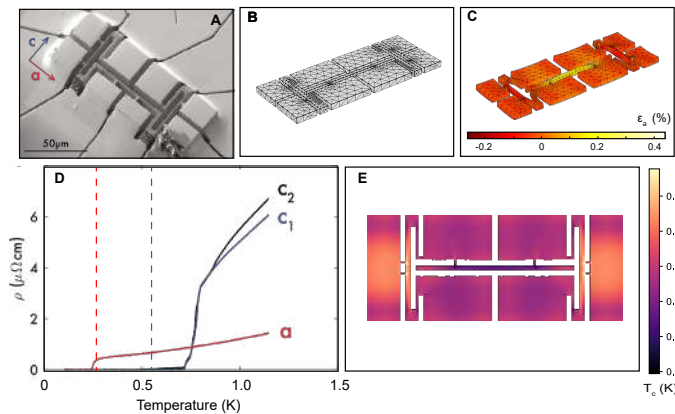


FIG. 1. (A) A SEM image of a small device comprised of bars set in the crystallographic a- and c- axes. The bars had dimensions of  $1.8 \times 8 \times 22 \mu\text{m}^3$ [1]. (B) 3D model of the small structure, created in COMSOL with a custom mesh overlaid. (C) Simulated distortion x 100 of the structure with strain  $\epsilon_a$  overlaid. (D) Transport data of temperature dependence in resistivity of the small structure, plotted in solid lines. The dashed lines represent the computed superconducting temperature of the structure along beams in either crystallographic direction. (E)  $T_c$  map of the surface of the microstructure.

ical parameters were changed in each simulation in an attempt to accurately simulate the susceptibility images for this structure. It became apparent that the thickness of the glue layer is highly influential in accurately modeling the strain field and superconducting spatial modulation of the crystal. We found that the thicker the glue layer, the more the structure began to reflect a sample in free space, essentially inducing a smaller strain field and creating a more elevated  $T_c$ . Once the glue layer more closely resembled the experimental set-up, the  $T_c$  map was in agreement with the susceptibility images, as seen FIG 2(A-C). A 3D model of a  $3.5 \mu\text{m}$  thick lamella and a glue layer of  $2 \mu\text{m}$  successfully generated comparable  $T_c$  maps. For example, there is a suppression of  $T_c$  along the long edges of the lamella, a pattern apparent in both the susceptibility images and the  $T_c$  map.

For the  $\text{Sr}_2\text{RuO}_4$  sample, modulations to the glue layer also proved important and influential in the spatial modulation of the superconducting transition temperature. If the glue layer was too thin (less than  $2 \mu\text{m}$ ) then excess strain was created resulting in elevated  $T_c$  along the short edges of the lamella. Once a more appropriate glue layer thickness was used, the simulations agreed with the susceptibility images. In the susceptibility images for  $\text{Sr}_2\text{RuO}_4$ , an asymmetry appeared at the top and bottom long edges of the sample (as seen in FIG 2(D(i)), the bottom long edge has a greater diamagnetic response than the top). The glue layer was assumed to be uniform and homogeneous throughout, however once an inhomogeneous glue layer was introduced the asymmetry seen in the susceptibility images appeared in the simulations. From even simple structures of rectangular lamellas it is apparent how the glue layer plays an important role in determining how much strain is applied to the structure and consequently determining the spatial modulation of superconductivity.

### III. DESIGNING NEW STRUCTURES

With the ability to control induced strain fields on a micrometer scale using a FIB, FEM simulations are helpful to better understand how unique geometries will generate strain fields. A deeper understanding of how induced strain fields influence the superconducting transition temperature may allow us to more precisely design and fabricate desired modulations in superconductivity for the production of certain devices.

#### A. Patterning Regions of Superconductivity

In many of the simulations performed, for either material and across varying structures, it was found that enough induced strain may dramatically or completely suppress  $T_c$ . In areas where high strain was found, the local  $T_c$  was suppressed well below the expected bulk  $T_c$ . This can be seen in the simple case of a rectangular a-b oriented  $\text{CeIrIn}_5$  lamella (the long edge of the lamella aligns with the a-direction, and the short edge with the b-direction) as seen in FIG 3. The computed superconducting critical temperature in the middle of the crystal, where the greatest strain is applied, is significantly lower ( $\sim 0.2\text{K}$ ) than the expected bulk ( $\sim 0.4\text{K}$ ).

For this structure, thicker glue layers were simulated to see if an elevated  $T_c$ , something more in line with what is to be expected, could be achieved. We found similar results with what was observed before with glue thickness modulations: the larger the glue layer, the higher the average local  $T_c$  was across the sample. The glue layer in FIG 3 was  $2.0 \mu\text{m}$  thick and produced a computed average  $T_c$  of  $0.2\text{K}$ . However once a layer of much greater thickness was applied ( $10.0 \mu\text{m}$ ), the average  $T_c$  across the sample increased noticeably (from  $0.2\text{K}$  to  $0.5\text{K}$ ).

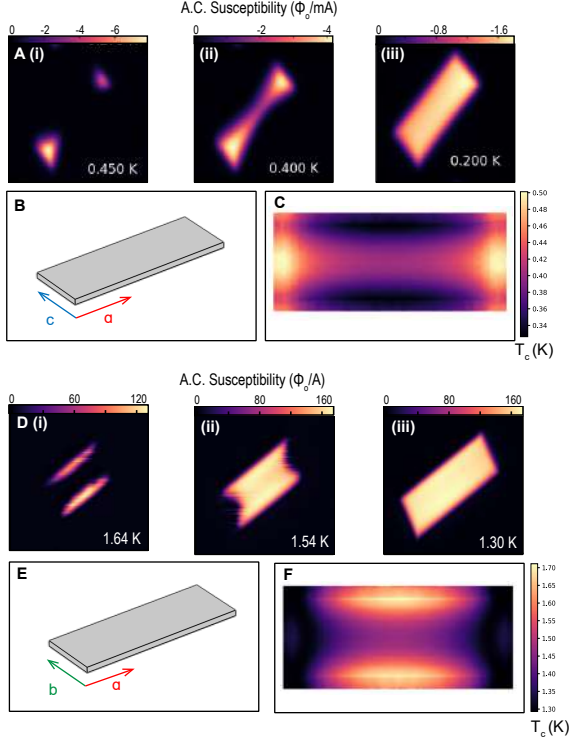


FIG. 2. (A(i)-A(iii)) Susceptibility images of a  $3.5\mu\text{m}$  thick, a-c oriented CeIrIn<sub>5</sub> lamella. These images were taken at three different and representative temperatures during a cool down. Negative diamagnetic susceptibility designates the superconducting regions of the sample. (B) 3D model of the sample of CeIrIn<sub>5</sub>. (C)  $T_c$  map of the surface of the sample. (D-F) Same as in (A-C) but for an a-b oriented Sr<sub>2</sub>RuO<sub>4</sub>.

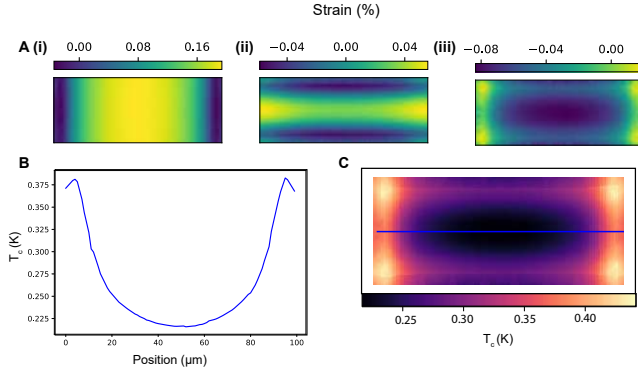


FIG. 3. (A(i)) Top view of the  $\epsilon_a$  component of strain for a a-b oriented CeIrIn<sub>5</sub> lamella. (A(ii)) Top view of the  $\epsilon_b$  component of strain. (A(iii)) Top view of the  $\epsilon_c$  component of strain. (B) Plot of the local superconducting transition temperature across the middle of the lamella (as illustrated by the overlaid blue line on the  $T_c$  map in (C)). (C)  $T_c$  map of the top surface of the lamella.

When thinner glue layers were simulated, a considerably more suppressed  $T_c$  map was generated. A glue layer of

$0.2\mu\text{m}$  thickness generated an average  $T_c$  of  $0.0\text{K}$  across the surface of the lamella. Across both materials and varying structures there is a strong dependence on glue thickness. The thicker the glue layer the more suppressed the induced strain field is, in the limit of thick glue the substrate becomes unimportant. This behavior being a result of the properties of the glue.

We then created structures with varying glue thicknesses by cutting into either the crystal or the substrate to assess which methodologies produced clearer and more prominent changes in  $T_c$ , further investigating our control over the superconducting critical temperature in specified areas of a structure. This was first done by creating 3D models of structures with varying shapes cut into either the crystal or substrate at different heights (an example of such structure is shown in FIG 4).

Variations of these structures included shapes being cut on the top or underside of the crystal, shapes being cut on the substrate, or creating protruding shapes on the surfaces of either the crystal or substrate. In all cases, an assumption that the epoxy would fill in the vacancies created by these shapes was made and simulated. For all variations of these simulations the depth or height of these shapes changed from column to column, cuts being as shallow as  $0.5\mu\text{m}$  or as deep as  $4.5\mu\text{m}$ .

We found that  $T_c$  as a function of either depth or height was dependent on the material being used and the crystallographic orientation. For CeIrIn<sub>5</sub>, the a-b oriented lamella produced more dramatic and profound results when compared to an a-c oriented lamella. Also, cutting into the substrate produced clearer results when compared to any other structure. For this structure, an a-b oriented CeIrIn<sub>5</sub> lamella with shapes carved out of the substrate, a noticeable increase in  $T_c$  as a function of shape depth occurred. These results are in agreement with what was observed in glue thickness modulations. Deeper cuts in the substrate created an increase in glue layer over the shape thus elevating  $T_c$  for the shape.

## B. Constrictions in Structures

With the ability to have micro scaled control of the induced strain field using a FIB, the possible fabrication of superconductor-normal metal-superconductor (SNS) Josephson Junctions within single crystals is an area of interest. We use simulations to investigate the viability of creating structures with suitable specifications in hopes of fabricating such devices. In order to achieve this, we wish to create a narrow normal conducting weak link between two superconducting areas. This was achieved by creating constrictions in the lamella.

We begin by placing a trench cut in the substrate below a rectangular CeIrIn<sub>5</sub> lamella. There is minimal change in the superconducting critical temperature over the trench, as seen in FIG 5(A). Structures with constrictions were then generated to create a more dramatic change in  $T_c$ . The first of these structures re-

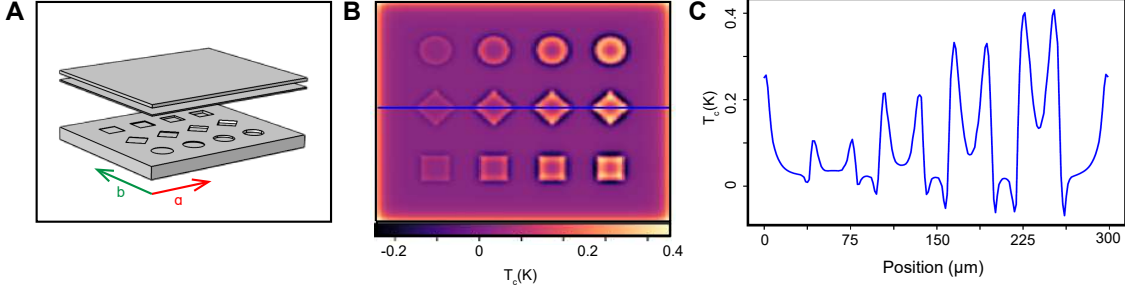


FIG. 4. (A) 3D model of a microstructure comprised of a  $200 \times 300 \times 3.5 \mu\text{m}^3$  CeIrIn<sub>5</sub> a-b oriented lamella, with shapes cut into the sapphire substrate. The shapes had diameters of  $30 \mu\text{m}$ , with depths or heights ranging from  $0.5 \mu\text{m}$  to  $4.5 \mu\text{m}$  (B)  $T_c$  map of the top surface of the lamella. (C) Plot of the local superconducting transition temperature across the middle of the lamella (as illustrated by the overlaid blue line on the  $T_c$  map.)

sembles a dumbbell and is seen in FIG 5(B). A more dramatic change in  $T_c$  is achieved, however the changes are sharp and irregular. The following structure, FIG 5(C), replaced the sharp vertices of the constriction with fillets. A more smooth change in  $T_c$  is achieved with this rounded dumbbell structure. Although the dumbbell structures produce well defined and profound decreases in  $T_c$  over the constriction, we want a larger difference from bulk  $T_c$  and constriction  $T_c$ . A final structure resembling a bow tie was created, as seen in FIG 5(D). In this structure the superconducting areas on either side of the lamella constrict to form a bridge between the two areas successfully creating a well defined weak link. A plot comparing all four different structures is shown in FIG 5(E). The bow tie structure creates the largest and smoothest decrease in  $T_c$ .

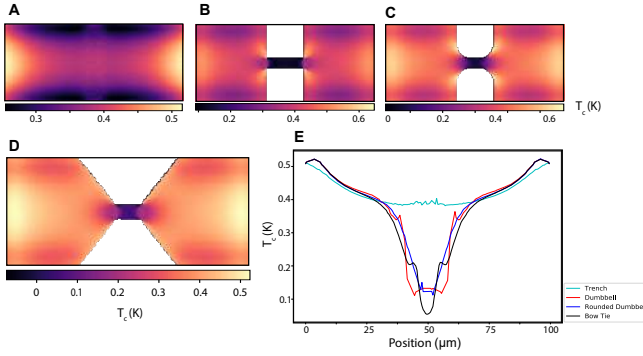


FIG. 5. (A)  $T_c$  map of the top surface of an a-c oriented CeIrIn<sub>5</sub> sample with a  $5 \mu\text{m}$  deep trench cut in the sapphire substrate directly underneath the lamella. (B-C)  $T_c$  maps of three different a-c oriented CeIrIn<sub>5</sub> samples with constrictions cut into the middle of the lamella. The constrictions were only cut into the crystal and glue layers of the structures. (E)  $T_c$  plots comparing the local transition temperature across the middles and constrictions of the lamellas for the four different structures whose  $T_c$  maps appear in the figure.

### C. Achieving Homogeneous Strain

In order to better understand the induced strain fields and coupling parameters it is worth investigating the homogeneity of strain as a function of height throughout the crystal. Initially there were great instances of inhomogeneity in strain as a function of height in the y and z components of strain for both materials and crystallographic axes in constricted structures throughout the constrictions. In order to create a homogenous strain across all components of the strain as a function of height, a trench was placed over the constriction and yielded promising results - these are shown in FIG 6.

## IV. STRAIN ORDER PARAMETER COUPLING

### A. Optimizing $\epsilon_{B_{2g}}$ Strain While Searching for Order Parameter Coupling

Currently the coupling is not well characterized between  $T_c$  and the  $\epsilon_{B_{2g}}$  strain in Sr<sub>2</sub>RuO<sub>4</sub>; simulations were created so that we could gain insight into geometries and structures that would optimize  $\epsilon_{B_{2g}}$  strain to try and identify a clear coupling. Two different structures were simulated to maximize the  $\epsilon_{B_{2g}}$  strain, these structures are shown in FIG 7. Each structure had a cross geometry such that the  $\epsilon_{B_{2g}}$  strain transitions through zero. This is achieved first by creating arms that extend in the [110] direction, ensuring that there is positive  $\epsilon_{B_{2g}}$  strain crossing over to negative strain, and vice versa as seen in FIG 7(A). A second structure with arms extending out in the [100] and [010] directions and then rotated  $45^\circ$  achieves the same results, shown in FIG 7(B).

With the simulated strain fields  $T_c$  maps were generated to see at what value of the order coupling parameter will produce a visible change in  $T_c$ . We begin by generating a  $T_c$  map with a low order coupling parameter, as if there is no coupling present. Then the coupling order parameter to  $\epsilon_{B_{2g}}$  was slowly increased until a noticeable

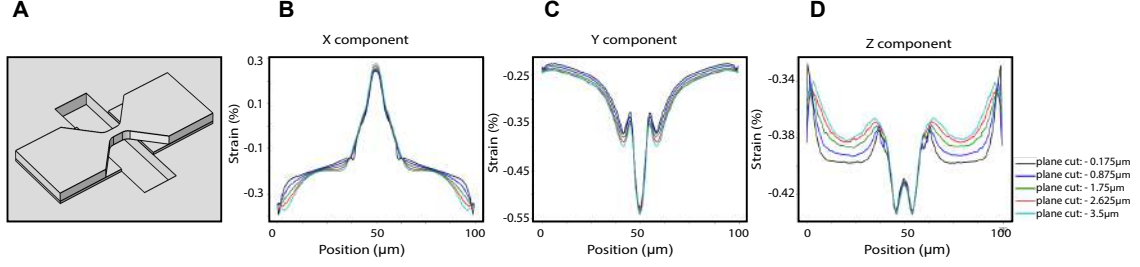


FIG. 6. (A) 3D model of a constricted a-c oriented  $\text{CeIrIn}_5$  structure placed over a  $5\mu\text{m}$  deep trench. (B-D) Strain as a function of height within the lamella.

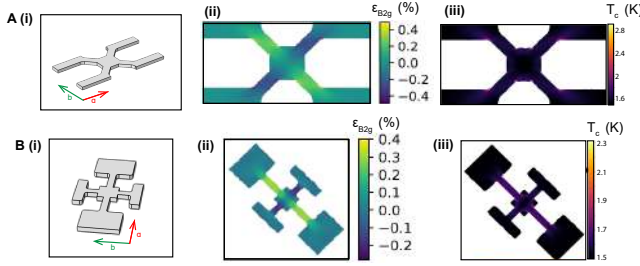


FIG. 7. (A(i)) 3D model of a A-B oriented  $\text{Sr}_2\text{RuO}_4$  structure created to maximize  $\epsilon_{B_{2g}}$  strain. (A(ii))  $\epsilon_{B_{2g}}$  strain at the top of the lamella. (A(iii))  $T_c$  map at the top of the lamella. (B(i)-B(iii)) Same as in (A(i)-A(iii)) but for a different cut geometry created to optimize  $\epsilon_{B_{2g}}$  strain.

change was observed in the  $T_c$  map. This change was observed when the order coupling parameter had a value of approximately  $n = 50\text{K}/\text{strain}$ . The high  $\epsilon_{B_{2g}}$  strain allows us to identify clear correlation between strain and  $T_c$ , and thus coupling between the two. In the  $T_c$  maps of FIG 7,  $T_c$  is elevated in the arms where high strain is observed. These simulations helped determine which structures were worthwhile to experimentally fabricate to further investigate the possible  $\epsilon_{B_{2g}}$  strain coupling with.

## V. DISCUSSION AND OUTLOOK

Finite element method (FEM) simulations have proven helpful in understanding spatial modulations of superconductivity in strain sensitive materials. Here we present simulation methods to better understand the relationship between experiment and superconducting patterns in  $\text{CeIrIn}_5$  and  $\text{Sr}_2\text{RuO}_4$  microstructures; while also investigating modulations in these microstructures and the resulting strain fields and superconductivity spatial modulation. These simulations were used to learn how physical parameters and changes affect the superconducting critical temperature, from which we learned how important of a role the glue layer plays. In addition to this, the FEM simulations gave us a look into what probable strain fields and spatial modulations of superconductivity are created under certain geometries and structures. This is helpful for investigating how to create devices and structures with certain specifications such as suppressing superconductivity in selected areas within a single crystal. Looking forward, these simulations can further provide aid in determining which microstructures are worth fabricating while also attempting to understand experimental data.

## VI. ACKNOWLEDGEMENTS

Thank you to the Nowack Group for hosting and welcoming me into their lab. Special thanks to Matt Ferguson and Professor Katja Nowack for their mentorship and a meaningful research experience. This work was supported by the National Science Foundation.

[1] M. D. Bachmann *et al.*, (2019), arxiv:1807.05079.  
[2] O. M. Dix, A. G. Swartz, R. J. Zieve, J. Cooley, T. R. Sayles, and M. B. Maple, Physical Review Letters **102** (2009), 10.1103/physrevlett.102.197001.  
[3] C. A. Watson, A. S. Gibbs, A. P. Mackenzie, C. W. Hicks, and K. A. Moler, Physical Review B **98** (2018),

10.1103/physrevb.98.094521.  
[4] C. W. Hicks, D. O. Brodsky, E. A. Yelland, A. S. Gibbs, J. A. N. Bruin, M. E. Barber, S. D. Edkins, K. Nishimura, S. Yonezawa, and Y. Maeno, Science **344** (2014), 10.1126/science.1248292.



# Evaluation of Iron-Impregnated Biochar as an Arsenic Adsorbent for Water Filtration

Jessica E. Rappaport, Matthew C. Reid, Lena Abu-Ali

## Abstract

Iron-impregnated biochar has been proven to show promising results as a low-cost sorbent for arsenic. In this study, 26mg of biochar were added to a groundwater matrix of sodium bicarbonate, potassium nitrate, arsenic, and milli-q water. The compounds sulfate, phosphate, bromide, fluoride, and humic acid were added to test how their presence impacted arsenic sorption. It was found that sorption decreased in some of these cases. Phosphate had the largest effect on sorption which is probably due to how similar its structure is to arsenic. Real groundwater was also tested at pH values of 5, 6, 7, 8, and 9. Sorption decreased as pH increased. This trend is likely because of the point of zero charge of the impregnated iron-oxides. Experiments were run in duplicates with two identical set-ups and a control that had no added arsenic. A q-value ( $q = \frac{\text{Initial Arsenic Concentration} - \text{Final Arsenic Concentration}}{\text{Biochar Concentration}}$ ) was used to calculate the density of arsenic adsorbed to the surface of the biochar.

## 1. Introduction

The World Health Organization recognizes that there are at least 140 million people in 50 countries who have been drinking water containing arsenic levels above the provisional guidelines of 10 µg/L.<sup>1</sup> Symptoms of arsenic poisoning include vomiting, abdominal pain, skin lesions, and cancer. Biochar has been proven to be a low-cost sorbent for arsenic.

For these experiments, we used biochar impregnated with 40g/L of iron. Adding iron to the biochar has been proven to increase sorption. As shown in the picture below, iron fills the pores of the biochar, creating sorption sites for the arsenic.

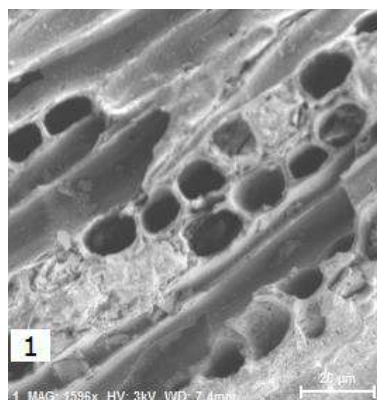


*Figure 1. SEM photo of biochar with iron in the pores*

We tested many different conditions to see how arsenic sorption was impacted by competing ions. Since it is common to find ions like sulfate, phosphate, bromide, and fluoride in groundwater, we tested each of these ions individually with our base matrix, which contained sodium bicarbonate, potassium nitrate, arsenic, and milli-Q water.

We also tested groundwater with added arsenic to see how sorption worked in actual groundwater.

## 2. Procedure

Samples were prepared by starting with an initial mixture containing a concentration of .160 mM arsenic, 15 mM sodium bicarbonate, and 50 mM potassium nitrate in 15 mL of milli-Q water. 2 mL aliquots of the sample were taken before adding any biochar to serve as a time 0 sample to see exactly how much arsenic was in each sample at the start of the experiment. Then 26 mg of biochar were added to each sample and the samples were placed on a rotary mixer for 48 hours. After 48 hours, final samples were collected using syringe filters. Both the initial and final samples were then run on an ICP-MS to determine the difference in arsenic concentration. We performed this procedure under many different conditions to see how certain compounds affected the arsenic sorption. We tested sulfate, phosphate, bromide, fluoride, and humic acid. We also ran samples containing only arsenic and groundwater. This allowed us to see what compounds present in groundwater could possibly outcompete arsenic for sorption sites on the biochar. In order to test the concentrations of these other compounds, we ran the samples on the IC to figure out their concentrations.

## 3. Results and Discussion

### 3.1 Sulfate

The graphs below depict the concentration of arsenic at both 0 hours (blue) and 48 hours (orange) when sulfate was added in different concentrations.

The first 2 sets of bars are duplicates and the third set of bars are the control where no arsenic was added to the sample.

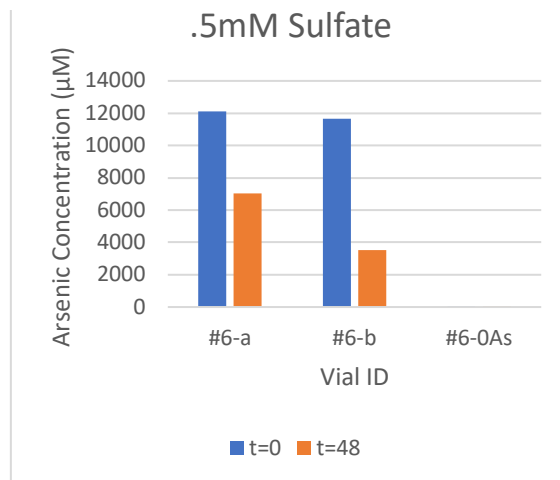


Figure 2. Base matrix plus .5mM sulfate

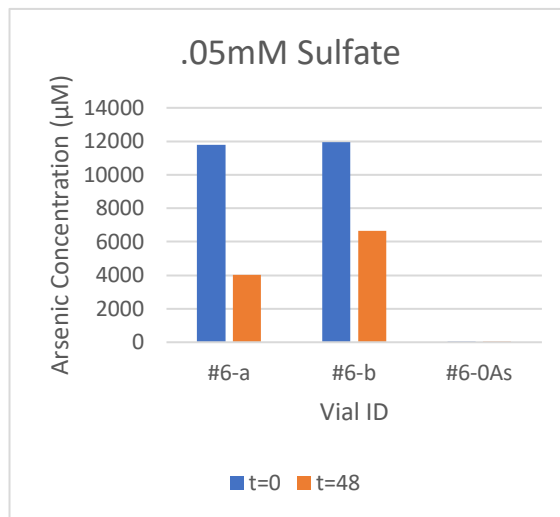


Figure 3. Base matrix plus .05mM sulfate

These results indicate that sulfate is competing with arsenic for binding sites on the biochar.

### 3.2 Phosphate

The graphs below depict the concentration of arsenic at both 0 hours (blue) and 48 hours (orange) when phosphate was added in different concentrations. The first 2 sets of bars are duplicates and the third set of bars are the

control where no arsenic was added to the sample.

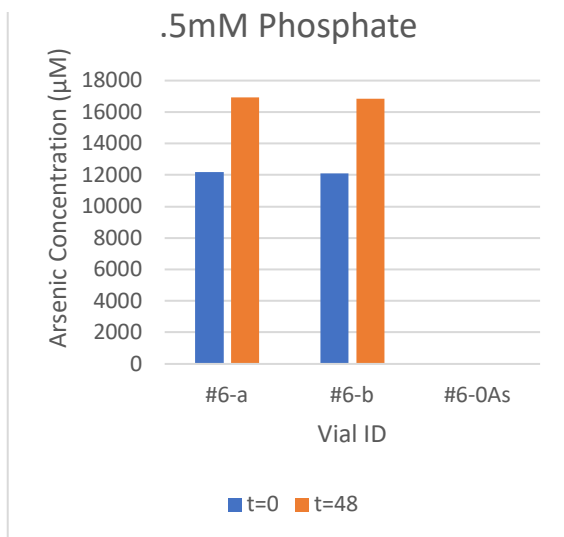


*Figure 4. Base matrix plus .5mM phosphate*

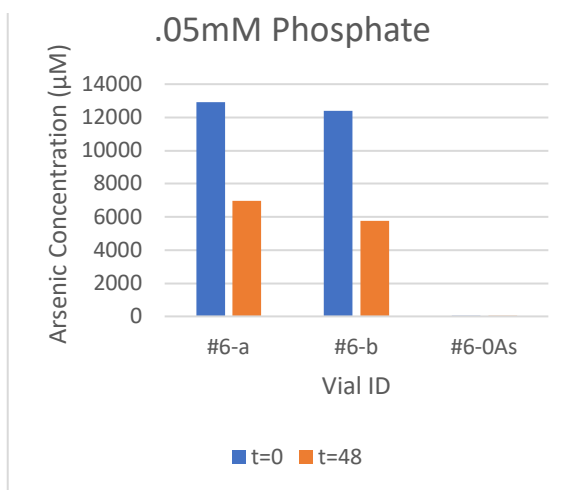


*Figure 5. Base matrix plus .05mM phosphate*

We are uncertain as to why the arsenic concentration appeared to increase when .5mM phosphate was added. We believe it could have had to do with interfering ions on the ICP-MS. These results suggest that phosphate is competing with arsenic for sorption sites.

### 3.3 Bromide

The graph below depicts the concentration of arsenic at both 0 hours (blue) and 48 hours (orange) when bromide was added. The first 2 sets of bars are duplicates and the third set of bars are the control where no arsenic was added to the sample.

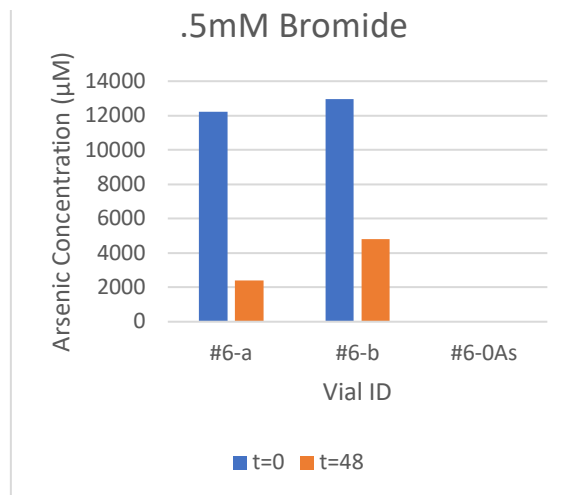


*Figure 6. Base matrix plus .5mM bromide*

These results suggest that bromide is not as large of a competitor for sorption sites compared to both sulfate and phosphate. The concentrations of arsenic went down more than how much they went down with sulfate and phosphate.

### 3.4 Fluoride

The graphs below depict the concentration of arsenic at both 0 hours (blue) and 48 hours (orange) when fluoride was added in different concentrations. The first 2 sets of bars are duplicates and the third set of bars are the control where no arsenic was added to the sample.

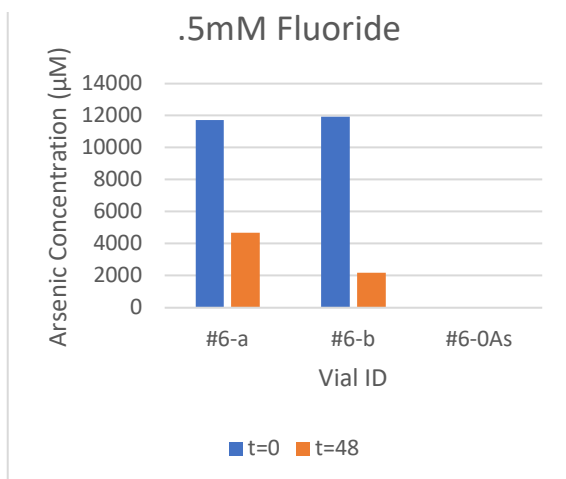


Figure 7. Base matrix plus .5mM fluoride

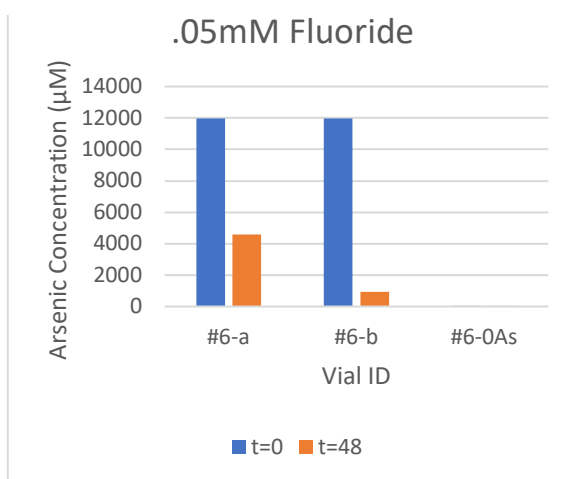


Figure 8. Base matrix plus .05mM fluoride

These results suggest that fluoride is not as large of a competitor for sorption sites compared to both sulfate and phosphate. The concentrations of arsenic went down more than how much they went down with sulfate and phosphate.

### 3.5 Aldrich Humic Acid

The graph below depicts the concentration of arsenic at both 0 hours (blue) and 48 hours (orange) when Aldrich humic acid was added in different concentrations. The first 2 sets

of bars are duplicates and the third set of bars are the control where no arsenic was added to the sample.

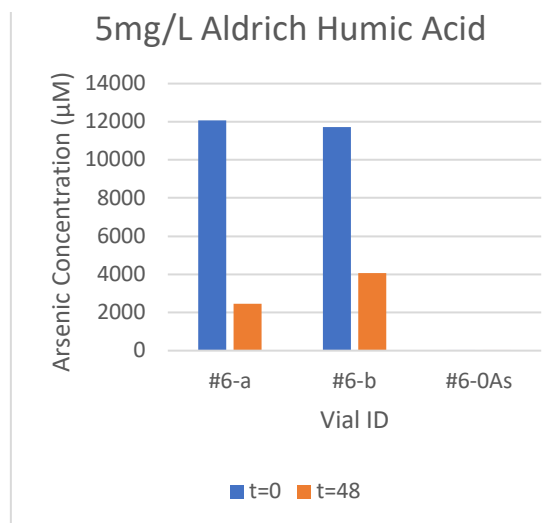


Figure 9. Base matrix plus 5mg/L of Aldrich humic acid

These results suggest that Aldrich humic acid is not as large of a competitor for sorption sites compared to both sulfate and phosphate. The concentrations of arsenic went down more than how much they went down with sulfate and phosphate.

### 3.6 Changing Base Concentration

The graphs below depict the concentration of arsenic at both 0 hours (blue) and 48 hours (orange) when the base concentration was changed. The concentration of sodium bicarbonate was decreased from 15mM to 2.5mM and the concentration of potassium nitrate was increased from 50mM to 500mM. The first 2 sets of bars are duplicates and the third set of bars are

the control where no arsenic was added to the sample.

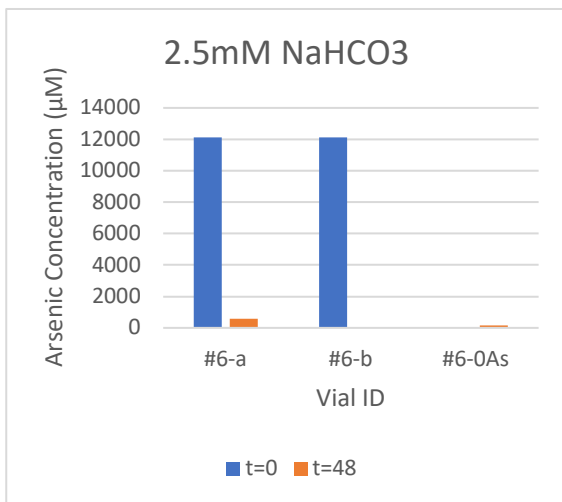


Figure 10. Change in base matrix from 15mM to 2.5mM sodium bicarbonate

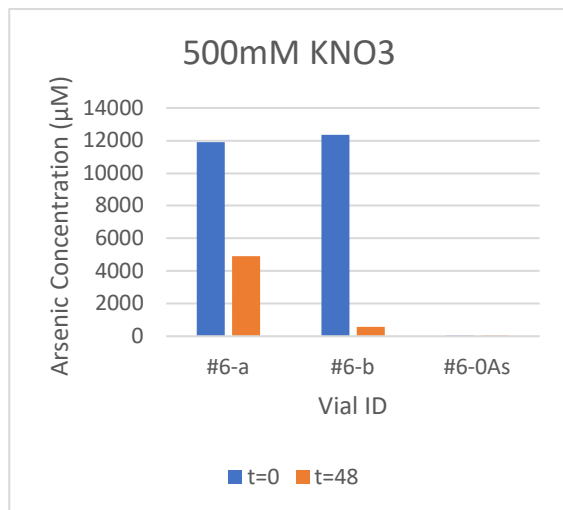


Figure 11, Change in base matrix from 50mM to 500mM potassium nitrate

These results suggest that our base matrix can be adjusted and optimized. It is worth noting that, even though the concentration of arsenic went almost completely down when there was a concentration of 2.5mM sodium bicarbonate, the pH of the solution dropped by 2 (from about 7 to about 5). We tried to keep the solution's pH stable by increasing the

sodium bicarbonate concentration to eliminate variables

### 3.7 Groundwater

The graphs below depict the concentration of arsenic at both 0 hours (blue) and 48 hours (orange) when groundwater with added arsenic was used. The 2 sets of bars are duplicates.

#### 3.7.i pH 5

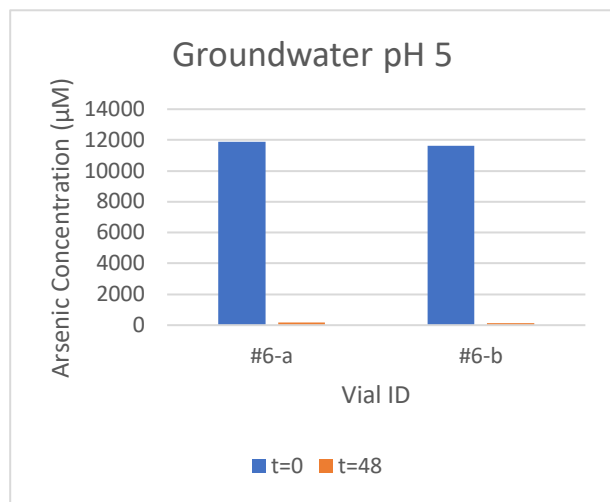


Figure 12. Groundwater adjusted to pH 5



### 3.7.ii pH 6

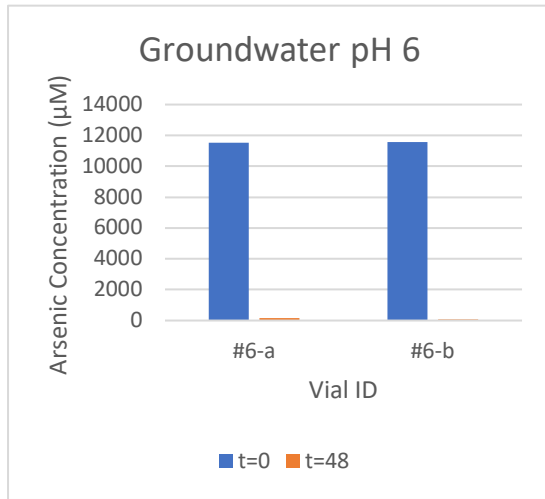


Figure 13. Groundwater adjusted to pH 6

### 3.7.iv pH 8

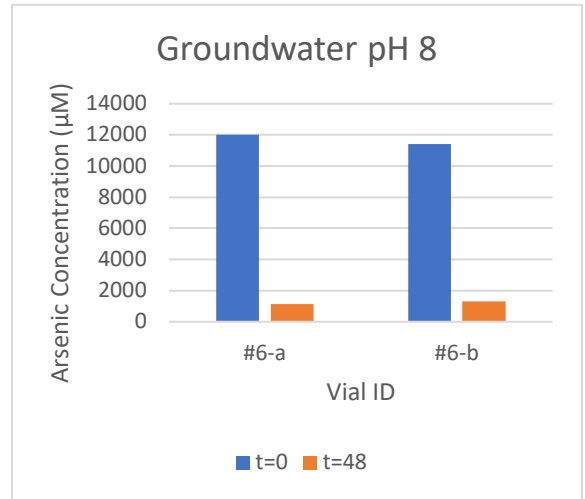


Figure 15. Groundwater adjusted to pH 8

### 3.7.iii pH 7

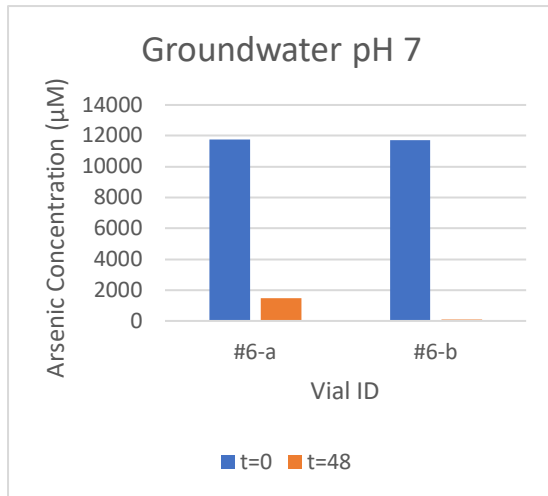


Figure 14. Groundwater adjusted to pH 7

### 3.7.v pH 9

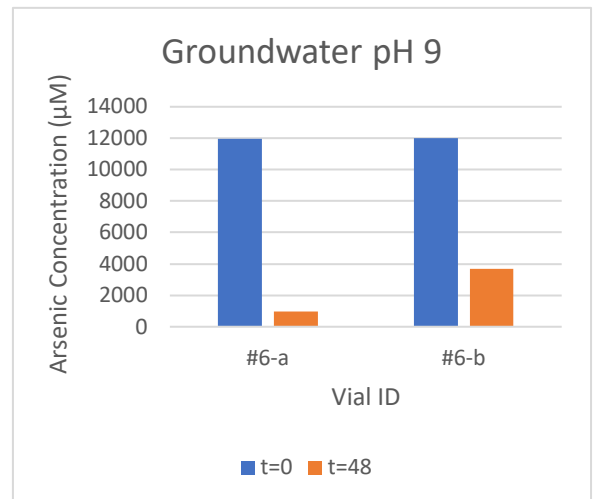


Figure 16. Groundwater adjusted to pH 9

These results suggest that when the pH goes above about 7, the sorption of arsenic decreases. This trend is probably do to the point of zero charge of the iron impregnated on the biochar. When the pH is above the point of zero charge (which is about 7 for iron), there is a net negative charge on the surface. Since arsenic has a negative charge, it makes sense that sorption would decrease as the system got more negative.

### 3.8 q-value Calculation

In order to compare our data, we calculated a q-value. This value represented the density of adsorbed arsenic to the surface of the biochar. The value was calculated by using this formula:

$$q - value = \frac{\text{Initial Arsenic Concentration} - \text{Final Arsenic Concentration}}{\text{Biochar Concentration}}$$

This value showed us truly how effective the biochar was at removing arsenic.

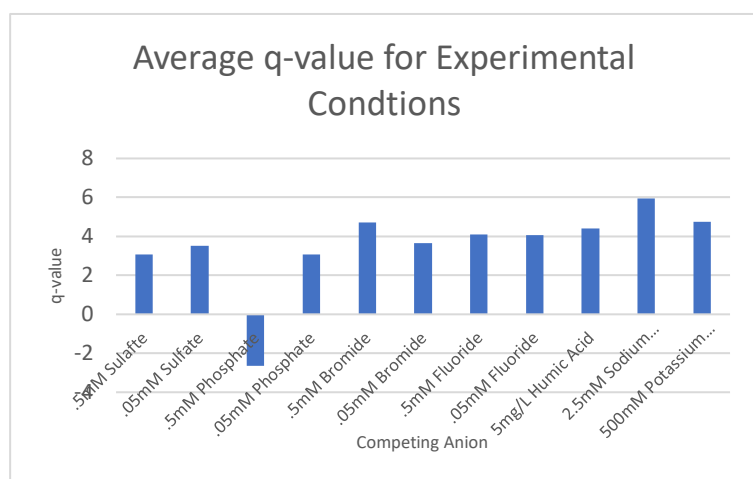


Figure 17. q-value comparison for all the experimental conditions

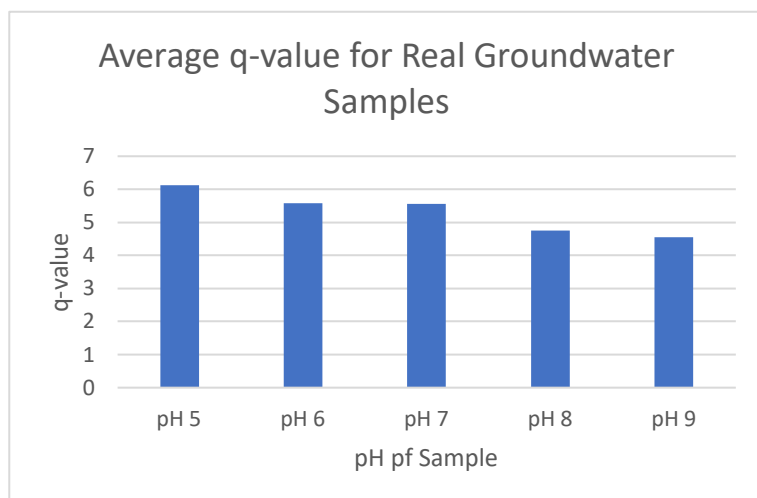


Figure 18. q-value comparison for all the groundwater samples.

### 3.9 Percent Removal

We used percent removal as another way to compare our data. This allowed us to see what percentage of arsenic was removed. It provides a clear image of the efficiency of all the different experimental conditions and groundwater.

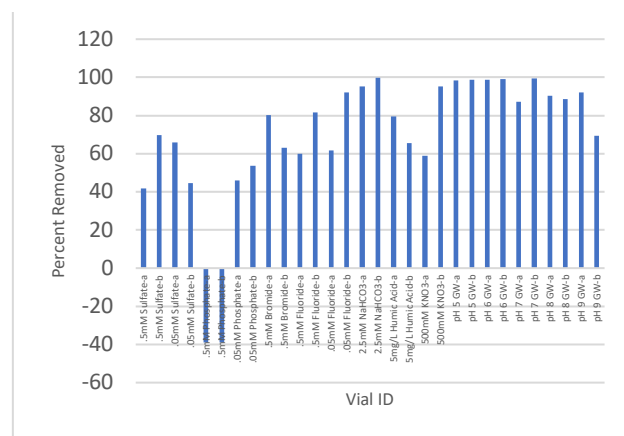


Figure 19. Percent removed from all experimental conditions and groundwater

### 4. Conclusion

From these experiments, we were able to conclude that biochar impregnated with 40g/L of iron caused sufficient removal of arsenic from our samples. In the presence of competing ions, sorption was affected but still efficient. The presence of sulfate and phosphate caused the most reduction in arsenic sorption. This was probably due to their similar structures to arsenic. Increasing the sodium bicarbonate concentration decreased arsenic sorption, however, it increased the buffer capacity so the solution stayed at a pH of 7 for the entirety of the mixing process. This study shows promising

results that biochar can be used to reduce arsenic concentration in water.

### **Acknowledgements**

I would like to thank Dr. Matthew Reid for giving me the opportunity to work in his lab, as well as Lena Abu-Ali for mentoring me through this summer. Additional thanks to the other members of the lab for welcoming me and to the CCMR REU program for making this experience possible.

### **Reference**

1. "Arsenic." *World Health Organization*, World Health Organization, [www.who.int/news-room/fact-sheets/detail/arsenic](http://www.who.int/news-room/fact-sheets/detail/arsenic).

# 3D Printable Heterogeneous Hydrogels to Increase Geometric Fidelity in Calcific Aortic Valve Disease Models

Maximillian J. Rozenblum, Benjamin J. Albert, Jonathan T. Butcher

Aortic valves presenting calcific aortic valve disease (CAVD) often experience diminishing valvular function as the disease progresses. Patients with advanced CAVD are often considered candidates for transcatheter aortic valve replacement (TAVR) to restore valve function. However, bulky calcific nodules may interfere with the expansion of the TAVR stent and may lead to paravalvular leak [1, 2]. 3D printing of patient-specific valve geometry and biomimetic, heterogeneous mechanical properties may allow for pre-procedure prediction of TAVR success. In order to achieve a high-fidelity print, this work explores the optimization of extrudant overlap by changing the center-to-center path distance in 3D printing.

## Introduction

Calcific Aortic Valve Disease (CAVD) has risen to become the most common valvular disease to affect the aging population in the developed world with an anticipated reach from 2.5 million people in 2000 to 4.5 million in 2030.<sup>1</sup> Morphological symptoms of CAVD include valve stiffening, narrowing and scarring. Additionally, CAVD patients find calcific nodules develop on the valve surface. The near-certain development of aortic stenosis may lead to ventricular hypertrophy, angina and syncope. According to a 2014 study by the Journal of American College of Cardiology (JACC), surgical aortic valve replacement with mechanical or bioprosthetic support pending the patient eligibility for surgery is the recommended prognosis.<sup>2</sup>

If open-heart surgery is not an option, another viable intervention may be the transcatheter aortic valve replacement (TAVR). Though formerly seen as an alternative to surgery, TAVR continues to receive growing interest due to its noninvasive nature compared to surgical options. More than a decade of TAVRs have led to the simplification and optimization of the procedure. A randomized study published in 2018 found that TAVRs can increase the rate of major vascular complications (6.0% to 1.1%), the occurrence of moderate to severe paravalvular leaks (5.3% to 0.6%), and the necessity for pacemaker implantation (25.9% to 6.6%) when compared to surgical AVR in patients having little to intermediate surgical liability and severe aortic stenosis.<sup>3</sup>

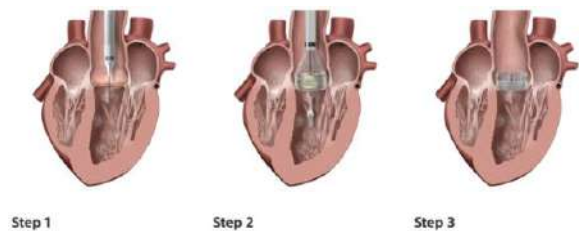


**Figure 1.** Schematic demonstrating three step TAVR.<sup>4</sup> Step 1: the artificial valve is compressed into a catheter and inserted into the femoral artery<sup>5</sup> where it will travel upwards until it reaches the diseased heart. Step 2: the doctor expands the artificial valve pushing the diseased leaflets out of the way. X-ray imaging is required to properly align valve orientation. Step 3: once in place, the new valve will begin to function and restore blood flow. This prompts catheter removal and incision closure.

As the TAVR procedure popularized, manufacturers sought to uncover how to reduce the observed complications. Though there have been monumental breakthroughs in the development of CAVD mechanisms<sup>6</sup>, recent trials have shown that we do not fully understand the cross talk between osteocyte<sup>7</sup>, macrophage, endothelial, interstitial or an unaccounted cell type as it pertains to CAVD enough for industrial considerations of molecular therapies. Thus, the incorporation of a molecular, tissue-targeting therapy into a TVAR stent is not commercially feasible.

For the purpose of analyzing the mechanical failure of the stent, a statistically significant supply of both CAVD and healthy valves are not affordable nor readily available for use. This prompts the need for a model that stent manufacturers could use to calibrate the position and distribution of stresses and strains from the

device applied onto the tissue. Finite element analysis can achieve just that but is often very idealized in the early stages due to the heavy weight on initialization parameters, valve geometry, and mechanical properties.<sup>8</sup> Thus, investigation into a synthetic, tissue-like model with the ability to perform quality assurance experiments on became the more ascertainable intervention.

The industry standard of synthetic biomaterials is polyethylene glycol diacrylate (PEGDA). It is biologically inert<sup>9</sup>, thus reducing inflammatory responses in vitro and in vivo. A photo-initiator can join monomer subunits of PEGDA together under light to form materials with higher mechanical strength. Laponite nanoclay or nanosilicate ( $\text{Na}_{0.7}\text{Si}_8\text{Mg}_{5.5}\text{Li}_{0.3}\text{O}_{20}(\text{OH})_4$ ) is a type of hydrous sodium lithium magnesium silicate that adopts a self-supporting, “house of cards” conformation that eliminates the need for a support bath and can be printed onto a surface in room temperature.<sup>10,11</sup> Laponite is the internal scaffolding to hydrogels it is mixed with. Hydroxyapatite (HA) is one of many calcium salts that deposit in cardiac tissue. HA is highlighted in this study because it has a binding peptide (HABP-19)<sup>12</sup> that under NIR light, can be clearly visualized. HA is useful for this model particularly because it is found in the calcific nodules and contrasts well with microCT imaging.

The fabrication of such a model necessitates that it is physiologically relevant in mechanical strength, and geometrically pliable in 3D extrusion to meet the demands of higher order structures. Additionally, the apparatus design must be able to account for calcific nodules that have different mechanical properties than healthy, non-calcified tissues.

## Methodology

### *Hydrogel Composite Synthesis*

Varying molarities (v/v) of PEGDA 700 (Sigma-Aldrich, St. Louis, MO), due its liquid composition at room temperature, were combined with Irgacure 2959 (Ciba Chemicals, Tarrytown, NJ) for photo-linkage (365nm), 6% Laponite RD (BYK, Wesel, Germany) as an internal scaffold

material, and deionized water were mixed together in a beaker for non-calcific hydrogel. To make a calcific hydrogel, 85% (w/v) hydroxyapatite was added to the aforementioned non-calcified components. All components except laponite were stirred thoroughly before addition of laponite because it increases viscosity and made subsequently added components immiscible. Materials were cast into circular disk molds on the surface of a glass slide. Subsequently, the casted disks were photo-linked by 365 nm UV light for 10 minutes.

### *Compression Testing and Analysis*

Upon citing the compressive moduli (kPa) of both calcific and non-calcific tissue<sup>9</sup> of aortic valve leaflets from patients with CAVD, compression testing was performed by an Instron material testing machine. Tensile testing in theory would offer larger amounts of information about the material properties of a hydrogel, but in practice the hydrogel is not stiff enough to be held in place or formed into an ideal dog bone. Subsequent data files were loaded into MATLAB for analysis.



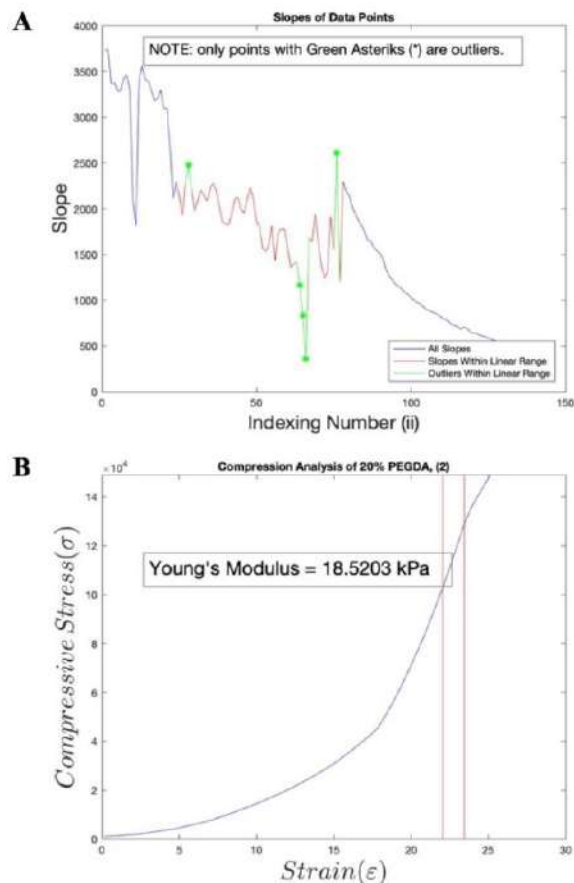


**Figure 2.** Example output screen from automated MATLAB compressive moduli calculations. Plot of the instantaneous slopes across the dataset (2A). The most-linear region denoted in red. Outliers removed from the most-linear region denoted in green. Plot of stress-strain profile with most-linear region enveloped in two red lines (2B).

The compressive moduli<sup>13</sup> used as a reference point for this study were experimentally calculated. Different from the idealized world of textbooks, the linear region of a stress-strain curve is not necessarily easy to observe. A possible explanation of this could be that material casts have small air bubbles and imperfect disk geometry after UV crosslinking. Upon compression from a controlled force with a 1-3 N/min force rate stress-profiles were recorded and stored in a sensitive .txt file. MATLAB analysis began with converting the encrypted .txt file into ASCII numbers and rewriting into malleable stress and strain matrices for mathematical operations. The  $n-1$  algebraic slopes were calculated for a dataset of length  $n$ . The slope values were plotted (Figure 2A) and allow the user to determine the interval of data that is most linear. Then MATLAB averaged the

data within the aforementioned most-linear range and removed outliers from the dataset by the optimization of the standard sum of errors mean algorithm. The complete output is a graph of the slopes and with the linear region and outlier data points color coded, and a second graph of the data with the indexing numbers and experimental compressive modulus printed in kPa (Figure 2B).

### Single Line Deposition

After validating the mechanical strength of a particular hydrogel composition, the second task is to assess the geometric pliability of said gel. The success of this model relies on a material that is easy to print such that the geometry of the extruded material matches the programmed print pattern input into the bioprinter. From now on this will be referred to as print fidelity. A material with high print fidelity extrusion, combined with the ultraviolet crosslinking-induced increase in mechanical strength theoretically yields an approach for patient-specific TAVR stent. To do this, an analysis of single line depositions of extruded materials was performed to evaluate the printability of a material.

40mm single-line paths of hydrogel groups were extruded using a freeform deposition bioprinter (Seraph Scientist, [www.scientist3d.com](http://www.scientist3d.com)) from 1.0mm above the print surface at 5-8psi on the distal end of the top face of a glass histology slide 5 times. The glass slide was then imaged while held perpendicular to the lens of the Zeiss Discovery V.20 stereoscope to measure the extrudant height (Figure 3A). The slide was additionally measured parallel to the microscope lens to measure the extrudant width (Figure 3B). The collection of single line measurements for a particular material and syringe tip diameter becomes a tool in characterizing adjacent multiline prints.

When two lines of extruded material are close enough to touch, fusion of the layers will occur, disrupting their isolated geometry. In theory there is a distance that optimizes the amount of fusion such that the two layers fuse to form a contiguous evenly-distributed mass, while also mitigating the excess extrusion that increases extrudant height (Figure 3C). If the latter occurs,

then the syringe tip will drag through the print and further disrupt the print geometry.

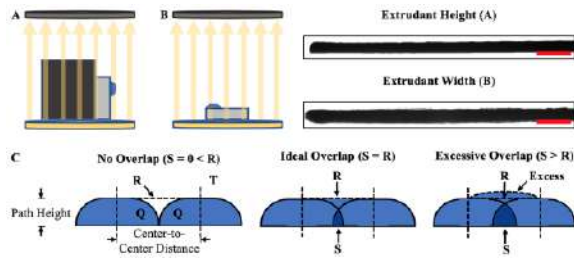


**Figure 3.** Representation of extrudant height (3A) and width (B) measurements. Gray cube is a metal block to stabilize the glass slide perpendicular to stereoscope lens (3A); scale bar 2.5mm (3A-B). Boolean model of printed hydrogel lines for predicting optimal path space that yields uniform layer.<sup>14</sup> Q: half cross-sectional area of each line; R: void region between printed lines; S: overlapping region; T: rectangular region formed between the centers of the two lines. This model assumed that when lines are overlapped, the void region R is reduced by equal volume of the overlapping region S (3C).

### Double Line Deposition

The optimization of the “center-to-center” distance between the midline of extruded lines yields ideal overlap for a more structurally uniform print that increases print fidelity. The double line deposition protocol prints two lines following the single line deposition protocol at variable distances: 1.25, 1.50, 1.75, and 2 (mm). Extrudant height and width from the double line data were compared against that of the single line deposition data. The center-to-center distance that minimized deviation from the single line deposition data was programmed into the print file and printed.

### Deposition Image Analysis

Images were uploaded into MATLAB integrated development environment. Visualization gave insight into the manual thresholding values to manually threshold out unwanted noise. Images were then binarized according to thresholding coefficient and instantaneous height and width measurements were measured. A hemocytometer was used to create a scale bar and convert pixel values to mm.

## Results and Discussion

From the mechanical compression testing, it was found that our hypothesized

concentrations of PEGDA 700 fell near to expectation. 50% PEGDA 700 was eliminated because the non-calcified group was too similar in strength to the calcified group. Findings are summarized below in table 1. The 40% PEGDA 700 group, though meeting necessary mechanical requirements was eliminated on the basis that a lower concentration of PEGDA 700 would result in relative elevation of print pliability.

% PEGDA 700 in Hydrogel	Calcified Moduli	Non-Calcified Moduli
30%	93.387 kPa	57.921 kPa
40%	110.402 kPa	68.751 kPa
50%	94.131 kPa	86.419 kPa

**Table 1.** Summarized findings of the compressive moduli from compression testing of hydrogel disks.

Tables 2 and 3 show the averaged measurements of extrudant height and width respectively. Though only the calcified datasets are displayed, the same calculations were applied to the non-calcified datasets.

Deposition Type	Mean Extrudant Height	Standard Deviation
Single Line	0.790 mm	0.0736 mm
Double 1.25	0.856 mm	0.0481 mm
Double 1.50	0.810 mm	0.0582 mm
Double 1.75	0.808 mm	0.0227 mm
Double 2.00	0.867 mm	0.0567 mm

**Table 2.** Tabulated extrudant heights from various deposition groups of calcified 30% PEGDA 700. For double deposition type, the subsequent number is the center-to-center distance. In single-line depositions  $n=5$  and for double line depositions,  $n=3$ .

Deposition Type	Mean Extrudant Width	Standard Deviation
Single Line	1.274 mm	0.1015 mm
Double 1.25	2.041 mm	0.2018 mm
Double 1.50	1.890 mm	0.0321 mm
Double 1.75	1.815 mm	0.0869 mm
Double 2.00	2.204 mm	0.2413 mm

**Table 3.** Tabulated extrudant widths from various deposition groups of calcified 30% PEGDA 700. For double deposition type, the subsequent number is the center-to-center distance. In single-line deposition  $n=5$  and for double line depositions,  $n=3$ .

As demonstrated in figure 3C, one of the objectives is to mitigate excess extrusion. This would affect multilayer print fidelity that would bear increasing inaccuracy proportional to the number of layers in height. Based on the results reported in table 2, 1.25mm and 2.0mm were eliminated as possible center-to-center distance. 1.25mm was too small of a distance and because of that over-extrusion occurs. 2.00mm was removed because it was observed that at that distance the two extruded lines would, on occasion, be too far to physically touch and exhibit no fusion (not pictured). Combining this information with that in table 3, there are few differences between the 1.50 mm and 1.75 mm groups. Consistent trends were found by repeating the data collection more than once: suggesting that the center-to-center distance yielding ideal extrudant overlap may be a range of values. The same methodology was used to find that the ideal center-to-center distance for the non-calcified hydrogel was 2.25mm (not shown).

This experimentation technique is not without flaw. First, with any automation process, it is imperative to increase efficiency, while simultaneously mitigating events that could disqualify the statistical relevance of the acquired data. The definition of the most-linear range in the mechanical testing phase does pose a question about the consistency of the data between iterations. If the linear region consists of a larger number of data points, by virtue of the SSE mean

algorithm, there is more lenience in outlier filtration. This means that larger linear regions, due to their larger sample size, tend to filter out more outliers than linear regions of smaller size. Though we believe it is an insignificant difference, it is worth noting and reevaluating in future iterations of this project.

Likewise, the design of the bioprinter was not under inspection for the duration of this study however, it is worth noting that the use of a servo motor to open and close syringe nozzles changed the position of the syringe tip in the printer coordinates without recognizing it within the print script. To combat this, we purchased a well-validated 3D extrusion printer and adapted it for bioprinting purposes. The relevant adaptation is the substitution of servo motors to a solenoid valve that using a relay switch controls the flow of pressurized air to each syringe without moving the syringe tip.

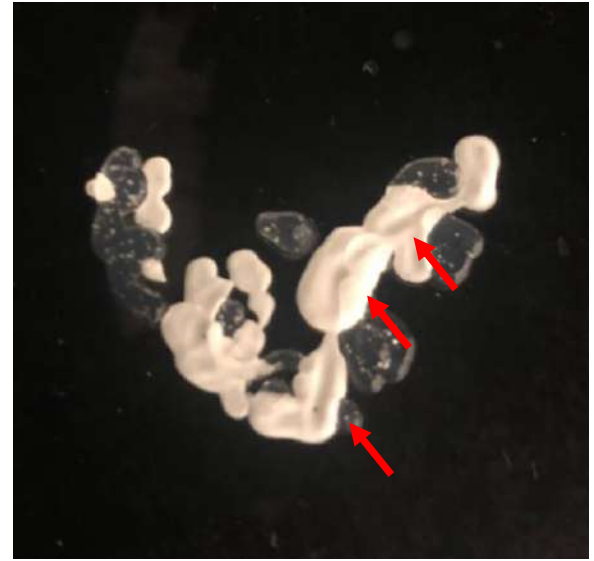


**Figure 4.** Image of a single-layer bi-material cardiac valve leaflet print. Opaque material is calcified nodules and translucent material is noncalcified. Creasing in the calcified region of the print (red arrow) are due to servo motor shifting the position of the syringe tip head. Not physiologically relevant print but possesses print fidelity.

To validate the process completely, we utilized the experimentally calculated center-to-center distance and created a print file in slic3r with path spacing equivalent to the derived value (Figure 4). Upon printing, the calcified and non-

calcified extruded into the expected geometry. This prompted the idea of performing the two-line deposition analysis on two different materials to observe if inter-material fusion requires a different center-to-center distance to optimize ideal overlap.

## Conclusions

Throughout the study, the aim was to develop a technique that, for a particular composite hydrogel, can experimentally derive the center-to-center distance to optimize the amount of ideal overlap caused by layer fusion. We performed the experiments multiple times and found consistent results of 1.75mm center-to-center distance for 30% PEGDA 700. The methodology was tested and validated by creating an .stl file with the path spacing determined to print cardiac valve leaflet. With the incorporation of patient-specific valve CT images, personalized synthetic valves to assess how a patient might respond to a TAVR procedure are on the horizon.

## Acknowledgements

I would like to thank Dr. Jonathan Butcher for offering me the opportunity and resources to work in his lab for the summer of 2019, as well as the mentorship I received from Ben Albert throughout the CCMR REU. Additional thanks to the warm environment offered to me by the remaining members of the Butcher lab. Lastly, I would like to thank the CCMR REU faculty for working tirelessly and applying to grants that make a way for students like myself to be able to afford and benefit from this style of experience.

## Funding

This work was funded by Medtronic, Inc. This work made use of the Cornell Center for Materials Research Shared Facilities which are supported through the NSF MRSEC program (DMR-1719875).

## References

1. Aikawa E, Schoen FJ. Calcific and degenerative heart valve disease., Stone J, Homeister JM, Willis MS, eds. In: Cellular and Molecular Pathobiology of Cardiovascular Disease. Elsevier: London, UK; 2014:161–181.
2. Nishimura, R. A., Otto, C. M., Bonow, R. O., Carabello, B. A., Erwin, J. P., Guyton, R. A., . . . Thomas, J. D. (2014). 2014 AHA/ACC Guideline for the Management of Patients With Valvular Heart

- Disease. *Journal of the American College of Cardiology*, 63(22). doi:10.1016/j.jacc.2014.02.536
3. T J Cahill, M Chen, K Hayashida, A Latib, T Modine, N Piazza, S Redwood, L Søndergaard, B D Prendergast, Transcatheter aortic valve implantation: current status and future perspectives, *European Heart Journal*, Volume 39, Issue 28, 21 July 2018, Pages 2625–2634, <https://doi.org/10.1093/eurheartj/ehy244>
4. The TAVR Procedure with LOTUS Edge™ [3 animated image sequence of a TAVR procedure. Provided by the Boston Scientific.]. (2019). Retrieved from <http://www.bostonscientific.com/en-US/patients/about-your-device/tavr-devices/how-tavr-devices-work.html>
5. What is TAVR? (2019). Retrieved from <https://www.heart.org/en/health-topics/heart-valve-problems-and-disease/understanding-your-heart-valve-treatment-options/what-is-tavr> Published by the American Heart Association.
6. Lee, S. H., & Choi, J. H. (2016). Involvement of Immune Cell Network in Aortic Valve Stenosis: Communication between Valvular Interstitial Cells and Immune Cells. *Immune network*, 16(1), 26–32. doi:10.4110/in.2016.16.1.26
7. Rementer, C. W., Wu, M., Buranaphattana, W., Yang, H. L., Scatena, M., & Giachelli, C. M. (2013). An Inducible, Ligand-Independent Receptor Activator of NF-κB Gene to Control Osteoclast Differentiation from Monocytic Precursors. *PLoS ONE*, 8(12). doi:10.1371/journal.pone.0084465
8. Sun, W., Martin, C., & Pham, T. (2014). Computational modeling of cardiac valve function and intervention. *Annual review of biomedical engineering*, 16, 53–76. doi:10.1146/annurev-bioeng-071813-104517
9. Zhu J. (2010). Bioactive modification of poly(ethylene glycol) hydrogels for tissue engineering. *Biomaterials*, 31(17), 4639–4656. doi:10.1016/j.biomaterials.2010.02.044
10. Hong, S., Sycks, D., Chan, H. F., Lin, S., Lopez, G. P., Guilak, F., . . . Zhao, X. (2015). 3D Printing of Highly Stretchable and Tough Hydrogels into Complex, Cellularized Structures. *Advanced materials (Deerfield Beach, Fla.)*, 27(27), 4035–4040. doi:10.1002/adma.201501099
11. Jin, Y., Liu, C., Chai, W., Compaan, A., & Huang, Y. (2017). Self-Supporting Nanoclay as Internal Scaffold Material for Direct Printing of Soft Hydrogel Composite Structures in Air. *ACS Applied Materials & Interfaces*, 9(20), 17456–17465. doi:10.1021/acsami.7b03613
12. Lee, J. S., Morrisett, J. D., & Tung, C. H. (2012). Detection of hydroxyapatite in calcified cardiovascular tissues. *Atherosclerosis*, 224(2), 340–347. doi:10.1016/j.atherosclerosis.2012.07.023
13. Lim, J., Ehsanipour, A., Hsu, J. J., Lu, J., Pedego, T., Wu, A., . . . Tintut, Y. (2016). Inflammation Drives Retraction, Stiffening, and Nodule Formation via Cytoskeletal Machinery in a Three-Dimensional Culture Model of Aortic Stenosis. *The American Journal of Pathology*, 186(9), 2378–2389. doi:10.1016/j.ajpath.2016.05.003
14. Kang, K. H., Hockaday, L. A., & Butcher, J. T. (2013). Quantitative optimization of solid freeform deposition of aqueous hydrogels. *Biofabrication*, 5(3), 035001. doi:10.1088/1758-5082/5/3/035001